Addis Ababa University
Addis Ababa Institute of Technology
School of Electrical and Computer Engineering

MTPA based Sensorless Control of a Half-Wave Rectified Rotor Excited Synchronous Motor

A thesis submitted to School of Graduate Studies of Addis Ababa University in partial fulfillment of the requirement for the Degree of Master of Science in Electrical Engineering (Control Engineering)

By
Amanuel Mekonnen

Advisor
Assoc.Prof.Mengesha Mamo(PHD)

November 18, 2021
Addis Ababa, Ethiopia

Addis Ababa University
Addis Ababa Institute of Technology
School of Electrical and Computer Engineering

MTPA based sensorless control of a Half-Wave Rectified Rotor Excited Synchronous Motor

By: Amanuel Mekonnen

APPROVED BY BOARD OF EXAMINERS

Name	Signature	Date
Dr.Bisirat Diribssa (School Dean)	....	....
Dr.Mengesha Mamo (Advisor)	....	....
Dr.Dereje Shiferaw (Examiner)	....	....
Mr.Yared Tadesse (Examiner)	....	....

Declaration

I, the undersigned, declare that this MSc thesis is my original work, that it has not been submitted for credit toward a degree at this or any other university, and that I acknowledge all sources and materials utilized in the thesis.

Name	Signature	Date
`Amanuel Mekonnen`	....	....

Dedication

To Mrs. Asdest Getaneh(M.A), I am so pleased to call such a distinguished woman My Mother. Mom, Watching you be so brave through the years makes me proud to be your son. Thank you Akoy for letting me grow my own wings, for letting me fly, for catching me when I fall, for letting me stand when I can't and for assuring me I can fly again. I soared even higher mom, simply because you believed in me.

”Mother: the most beautiful word on the lips of mankind”

`Amanuel Mekonnen`

Acknowledgment

First and Foremost, I sincerely Look-up-to The Almighty God for His Grace, for giving me strength, sustenance and above all, for his Faithfulness and Love from the beginning of my academic life upto this Masters Level. God's benevolence has made me Excel and Successful in all my academic pursuits.

Besides God, I would like to express my sincere gratitude to my advisor, Assoc. Prof. Mengesha Mamo(PHD), for the continuous support on my MSc Study and Research, for his patience, enthusiasm, immense knowledge and more than anything for believing in my potential. His advice was invaluable during the research and writing of my thesis. I could not have imagined having a better advisor and supervisor for my MSc thesis.

Then, I would like to thank my senior, Mr. Getsh Fikadie, for his encouragement, insightful comments and directions, from the beginning to the end of this MSc Thesis.

Last but not the least, I would like to say Ms. Elsabet Ataklti thank you for being on my side and for your confidence in me. Besides when I needed your generosity, you were there for me. This journey wouldn't have been possible without your support. Thank you!

`Amanuel Mekonnen`

Abstract

In this thesis, Maximum Torque Per Ampere (MTPA) based sensorless Field-Oriented Control (FOC) of the Half-wave Rectified Rotor Excited Synchronous Motor (HRreSM) for Electric Vehicle (EV) traction drive application is presented. The traction motors in EVs are responsible to deliver the maximum possible torque for the vehicle's propulsion and the motor should have a flux weakening capability for the high speed range drive of the vehicle. HRreSM has simple, robust and maintenance free mechanical structure with brushless means of field excitation. Variable field flux and torque control capability of HRreSM can be supported by the proper control strategies to increase the efficiency of the motor drive system. Two consecutive control strategies, MTPA and Flux Weakening (FW), with in the FOC are implemented to study and verify the performance of the controlled motor drive system for the proposed EV application. Since the position of the rotor flux is crucial in a FOC system, a sensorless rotor position information extraction method based on the bias frequency component of the stator current is implemented. The proposed drive is demonstrated by simulation on linked MATLAB/ Simulink and Ansys Electronics/ Simplorer environments.

Simulation results show that, the extracted (estimated) rotor position perfectly tracks the actual (sensed) position in the whole speed range of the motor. The extracted rotor position of the motor is compared with the actual rotor position for validation. And The MTPA control performance has been compared to the constant i_d control strategy, and 52.78% more torque generation is registered by the MTPA control model. The performance study of the FW control strategy is made by making a comparison between MTPA based model (for the whole speed range) and MTPA and FW based model (FW applied after the base speed of the motor). And 21.97% speed extension beyond the speed limit of the MTPA based model is obtained by implementing MTPA and FW control strategies consecutively. Therefore, the developed sensorless drive model, with good torque performance and speed range extension beyond the base speed of the motor, is verified to be efficient for EV traction drive applications.

Keywords— Electric Vehicle (EV), Maximum Torque Per Ampere (MTPA) Control, Sensorless

Contents

List of Figures

List of Tables

List of Abbreviations

AC	Alternating Current
BJT	Bipolar Junction Transistor
CFC	Carrier Frequency Component
DC	Direct Current
DFOC	Direct Field Oriented Control
emf	Electromotive Force
EV	Electric Vehicle
FET	Field Effect Transistor
FOC	Field-Oriented Control
FW	Flux Weakening
HEV	Hybrid Electric Vehicle
HRreSM	Half-wave Rectified Rotor Excited Synchronous Motor
IFOC	Indirect Field Oriented Control
IGBT	Insulated Gate Bipolar Transistor
IPM	Interior Permanent Magnet
KVL	Kirchhoff’s Voltage Law
mmf	Magnetomotive Force
MOSFET	Metal-Oxide-Semiconductor Field-Effect Transistor
MTPA	Maximum Torque Per Ampere
ODE	Ordinary Differential Equation

PI	Proportional Integral
PM	Permanent Magnet
PMSM	Permanent Magnet Synchronous Machines
PWM	Pulse Width Modulation
SIM2SIM	Simulink to Simplorer
SM	Synchronous Motor
SPM	Surface Mounted Permanent Magnet
SPWM	Sinusoidal Pulse Width Modulation
SVPWM	Space Vector Pulse Width Modulation
THD	Total Harmonic Distortion
VFD	Variable Frequency Drive
VSI	Voltage Source Inverter

Chapter 1

Introduction

1.1 Background of Study

In a world where environmental sustainability and energy efficiency are becoming increasingly relevant, the advent of electric vehicle (EV) technology has accelerated to meet these demands. Concerning the environment, EVs can provide emission free urban transportation,even taking into account the emissions from the power plants needed to fuel the vehicles, the use of EVs can still significantly reduce global air pollution. From the energy aspect, EVs can offer a secure, comprehensive and balanced energy option that is efficient and environmental friendly [1][2].

In EVs, traction motors are the key component for propulsion, which require high torque and power density, wide speed range, high efficiency, high reliability, low noise, and reasonable cost [3]. Different machines have been used in EVs and HEVs (hybrid electric vehicles) so far. Induction machines, permanent magnet synchronous machines, DC machines and switch reluctance machines are the most applicable machines. Induction machines are the most interesting machines for EVs up to now. Whereas, permanent magnet synchronous machines (PMSMs) are the most capable competing with induction machines for the electric machines of EVs. This is due to their many advantages over the dc and induction machines including high efficiency, compactness, high power density, fast dynamics and high torque to inertia ratio. Interior permanent magnet (IPM) synchronous machine, which is one type of PMSM, with extra features of mechanical robustness, capability of flux weakening for high-speed operation are particularly suitable as electric machines of EVs [4].

PMSMs and other brushless synchronous motors like reluctance type synchronous motors can be used for various applications including EV traction drive. However, their capacity is limited by both demagnetization in overload condition and the poor power factor. Randel type and inductor type synchronous motors have complicated magnetic path structure and they are very large because they are excited by the stator winding not on the rotor winding. The ac excitation scheme and rotary commutation scheme of these motors are not suited for a variable speed motor. The disadvantage of their rotary transformer scheme is that motor construction is complicated. The structural disadvantage caused by the presence of exciter becomes remarkable as the capacity increases [5]. In order to compensate for the drawbacks of these brushless synchronous motors, a brushless self-excited three-phase commutator less motor, Half-wave Rectified Rotor Excited Synchronous Motor(HRreSM), have been invented by Nonaka in 1958. Self excitation in HRreSM is made possible by connecting a diode in series with the field winding on the rotor and by utilizing the backward-rotating field caused by single-phase Magnetomotive Force(mmf).

The half-wave rectified rotor excited synchronous motor is the same as conventional salient pole type synchronous motor, but whose rotor winding is short circuited through a diode. On the rotor, permanent magnet can be attached for additional torque generation [6]. But the torque generation is not fundamentally dependent on the permanent magnets. The principle of operation is, an electromotive force(emf) with bias frequency is induced in the rotor winding of this motor by the mmf which rotates at synchronous speed and pulsates at bias frequency. The field poles are excited by the field current obtained by rectifying this emf with a diode inserted into the field winding. The ”HRreSM” is with the following special features: (1) The motor has simple and robust brushless structure and is maintenance free. (2) The motor parameter variations, due to temperature rise and many other factors, do not affect the performance of the motor. (3) For the whole speed range of operation (including high speed operation), motor speed and torque control is possible by using a FOC of the motor to control the excitation currents and the torque current independently [7] [8]. The performance characteristics of the HRreSM can be supported by the control strategies with in the FOC of the motor depending on the electromagnetic performance requirement of the drive application.

FOC of HRreSM can be implemented by using either Maximum torque per ampere (MTPA) control strategy or constant i_d control strategy. MTPA control has straightforward goal of maximizing the output torque while minimizing the stator current amplitude. It has long been recognized that for a given load torque, it is possible to adjust the d-q axis component of stator current so as to maximize the output torque. It results in the minimization of resistive and core losses thus maximizing the efficiency of the motor drives for a particular operating point [9], [10], [11]. Constant i_d control strategy uses a constant current supply for the reference d-axis current with in the FOC of the motor, while using the torque command from the speed controller as a q-axis current reference [12]. Even if $i_d = 0$ control strategy is the most common control method in electric machines, it is not applicable for the control of HRreSM for some reasons. The first reason is the structure of the HRreSM is salient pole type, while the $i_d = 0$ control is for the non-salient type machines. The other reason is HRreSM requires modulation of the stator current (d-axis component) with a triangular signal for better average field flux production [13]. So letting the d-axis current component reference value to zero can’t be taken as an option for the control of HRreSM.

The HRreSM has naturally flux weakening capability for wide speed range operation. Since independent control of the flux and torque producing current components is possible in HRreSM, by using any flux weakening technique one can make the flux controlled and make the wide speed range operation happen. The motors like induction motors, separately excited dc motors and other with the direct access of field current can employ the direct reduction of field current for weakening the field winding flux for high speed operation. And the PM synchronous motors use a different approach of demagnetizing the rotor flux since the rotor flux is provided by the PM [14].

Due to the cost and reliability effectiveness of the sensorless control, employing sensorless rotor position extraction method in the FOC of the proposed motor is necessary. Sensorless rotor position extraction of the HRreSM is possible and precise using the following methods. The first method is provided by [7], If there is any displacement between the axis of rotating mmf and the axis of the rotor, the impedance of the field circuit varies. Therefore, the rotor position of the HRreSM can be detected only by measuring bias frequency components of armature voltage. And the other candidate for the sensorless rotor position extraction of HRreSM is provided by [15], this approach extracts the rotor position information from the carrier (high) frequency component of the stator current, where the saliency information is indirectly obtained from these currents. In this thesis, Rotor position extraction from the bias (high) frequency component of the stator current is developed, which is a direct adoption of the method by [15].

1.2 Statement of Problem

In EVs, the traction motors are very important for propulsion, i.e., the performance of the traction motors. If the EV is expected to work under different driving cycles for example in urban and highway driving cycles, the selected motor must be designed and controlled to have greater electromagnetic performance under every drive cycle. Higher electromagnetic performance means the vehicle must have a maximum torque output for the vehicle acceleration and flux weakening capability for wide range operation, under the current and voltage limits.

HRreSM has simpler and robust brushless structure and is maintenance free, the motor performance is not affected by the variation of the machine parameter, it has flux weakening capability, it enables us to control the torque over the speed range from the state of standstill to the rated speed, because the torque and excitation currents can be independently controlled and the nature of the motor makes the rotor speed/ position estimation from the standstill to the constant power possible. So, employing a sensorless control, direct field oriented control (DFOC), based on MTPA technique for the given motor creates a very special system with better torque performance and wider speed range. In MTPA control strategy the two axis stator reference currents are calculated so that the maximum torque per ampere will be achieved and results in the minimization resistive and core losses thus maximizing the efficiency of the motor drives for a particular operating point.

The sensorless control is proposed to be used for speed calculation because using a mechanical rotor position sensor for direct speed measurement is very costly, less reliable and increase the system weight. Therefore, the sensorless approach to estimate the rotor position and speed is a very efficient way to control the whole system. The speed will be calculated from the estimated or extracted rotor position.

1.3 Objectives

1.3.1 General Objective

Assuming an electric automobile running on flat surface, to design and simulate an MTPA based sensorless control of a half-wave rectified rotor excited synchronous motor (HRreSM); in order to evaluate the torque performance and wide speed range operation of the motor.

1.3.2 Specific Objectives

- Development of Rotor Position Information Extraction.
- Implementation of MTPA Control Strategy.
- Implementation of Flux Weakening Control Technique.

1.4 Methodology

Simulation of MTPA based sensorless control of HRreSM is based on the block diagram shown in the figure 1.1. In this thesis work, sensorless rotor position estimation, MTPA control strategy for maximum torque per ampere generation below the base speed, and FW control technique for speed extension above the base speed are employed within the field oriented control of the proposed motor, HRreSM. The sensorless control, saliency based, over the whole speed range (from standstill to the high speed, above the base speed), is the source of the rotor flux position and motor speed in the FOC. In the MTPA control, the two-axis stator reference currents are calculated so that the maximum torque per ampere will be achieved.

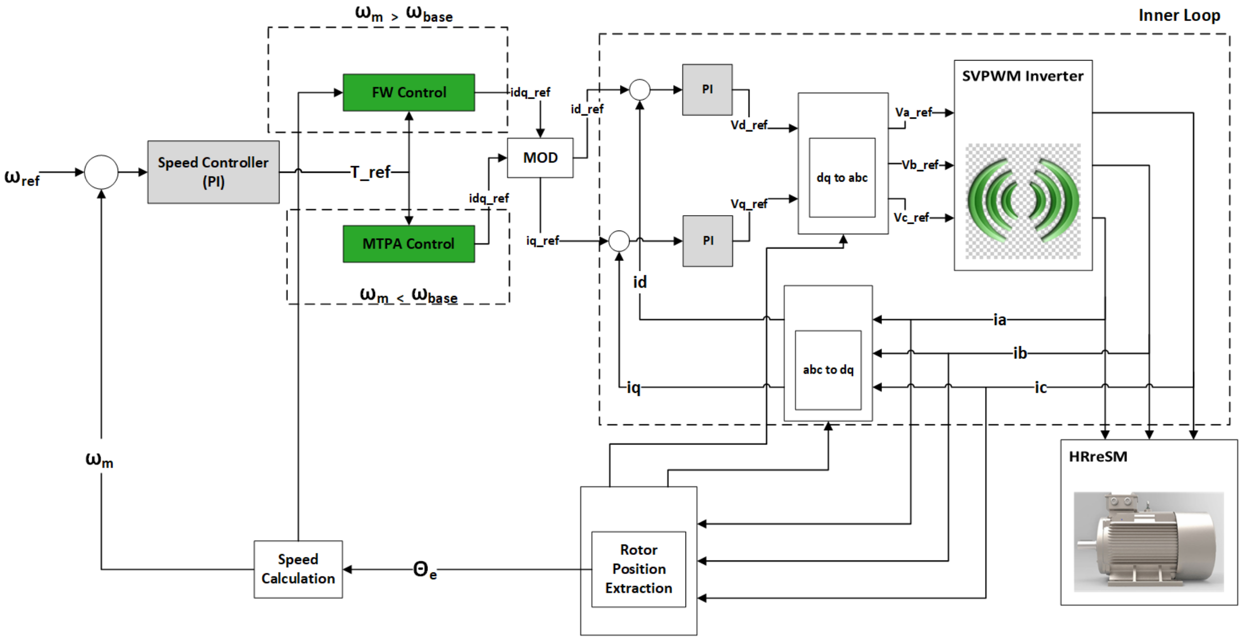

Figure (1.1) General block diagram of MTPA based sensorless control of HRreSM

The simulation model of the whole system shown on the block diagram is developed and simulated on and integrated simulation environment (Link between MATLAB/ Simulink and Ansys Electronics/ Simplorer). MATLAB/ Simulink in this study is the core simulation environment containing control model, rotor position information extraction, SVPWM gate control signal generation, Motor's simscape model and interfacing link (SIM2SIM) for the other modeling software, Simplorer. The SVPWM Inverter block and the HRreSM block on the general block diagram of the above figure are a Simulink-Simplorer link and motor's simscape model respectively. Simulnk generates a gate control signal to the inverter model on Simplorer using SVPWM technique, at the same time receives back the inverter's outputs (3-phase phase voltage) to supply Simscape model of the motor.

1.5 Contribution of The thesis

The main contributions of this thesis are:

1. This paper proposes to use: (i) Half-wave rectified rotor excited synchronous motor which is very effective for a maximum motor torque output with wider operating speed application, (ii) The sensorless speed estimation mechanism since it is very cost effective, precise and reliable and (iii) The field-oriented control based on MTPA and FW techniques for maximum output torque with minimum losses and for wide speed range operation of the motor respectively.
2. This thesis uses the saliency of HRreSM for rotor position information extraction, which requires analyzing the high frequency (bias frequency) component of the stator current.
3. The thesis proposes to employ SVPWM signals, which is intern filtered and used for analysis purpose. Since SVPWM is a digital modulation technique, its result can improve the performance of the drive system. SVPWM results in an optimized algorithm for real time control system.
4. The thesis is demonstrated by simulation, where the simulation enviroment is an integration of MATLAB/ Simulink, Simscape and Ansys Electronics/ Simplorer. Using multi-simulation environment for simulation helps to get a more realistic and practically possible responses from the drive model.

1.6 Thesis Organization

The thesis is organized into six chapters including this introduction. The rest of the thesis is organized as follows.

Chapter 2 describes the theory and operation principles of HRreSM. Dynamical modeling of HRreSM with field oriented control (vector control) based on coordinate transformation is described. Principle of SVPWM technique is also described in detail. A short summery for the reviewed articles is included in the literature review section of this chapter.

Chapter 3. In this chapter the concepts behind the proposed MTPA control, FW control and rotor position information extraction are tried to be covered.

Chapter 4 contains information about the design and modeling of the overall simulation and it's parts. The parts of the whole simulation are the motor, the inverter and the controller.

Chapter 5 shows and discusses the simulation results of the proposed controlled drive system on Matlab/Simulink and Simplorer. The result and discussion focuses on demonstrating the specific objectives of this thesis.

Chapter 6 draws conclusion from the developed simulation in this thesis and recommend further research possible areas for the future work.

Chapter 2

Vector Control of a Half-Wave Rectified Rotor Excited Synchronous Motor

2.1 Introduction

In this chapter the theoretical explanation and mathematical modeling of the developed vector control of HRreSM together with literature review is discussed. The first section is the mathematical modeling of the proposed motor, HRreSM, including the analysis using motor parameters and variables in the d-q axes reference frame. The mathematical modeling covers the motor structure, principles of operation, voltage equations and principle of torque generation for this particular motor.

In the next section, the SVPWM technique for generating a pulse signals to the inverter gates is discussed. It is obvious that the HRreSM must be supplied from a well controlled inverter for a variable speed drive operation of the motor. And among the types of inverter gate control signal generations, SVPWM technique is selected and discussed briefly.

The concept and types of vector control are also discussed in this chapter. Since the vector control, DFOC, employing MTPA and FW control strategies is used in this study, on the fourth section of this chapter the necessary backgrounds behind the candidate vector control method is discussed briefly.

The final section is a literature review, which contains the short summery of the reviewed papers in the process of developing this thesis, is provided. On this section, motors used for EV application, MTPA and FW control techniques for the control of HRreSM, the use of multi-simulation environments for simulation modeling and finally, the research works related to this thesis are reviewed and discussed.

2.2 Half-Wave Rectified Rotor Excited Synchronous Motor

2.2.1 Motor Structure and Operation Principles

HRreSM, induction machines and Conventional 3-phase synchronous machine have the same stator winding structure. Their stator windings have three symmetrically arranged coils, where there is a 120^o phase shift between each coils. Look at Figure 2.1 for the case of HRreSM. A salient pole type rotor with a diode short circuiting the field winding terminals is the employed rotor structure in the proposed motor, HRreSM, [13].

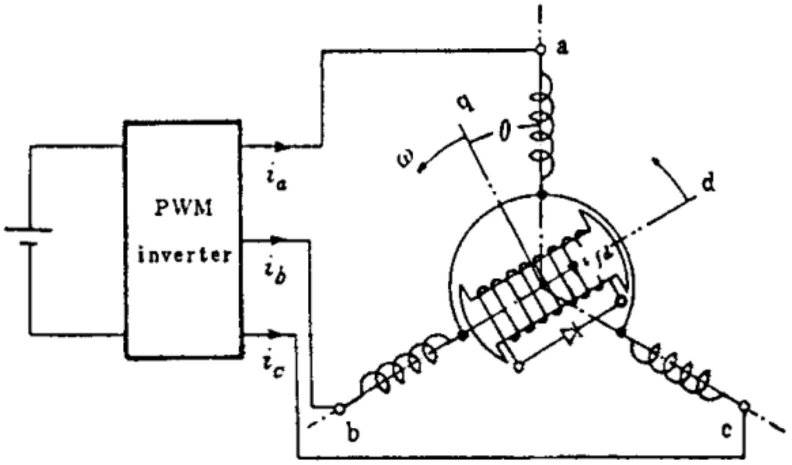

Figure (2.1) Circuit Diagram of The Motor, [13]

In HRreSM, a constant magnitude magnetic field is produced, when a balanced 3-phase current passes through the stator coils. The produced magnetic field rotates at constant angular velocity ω. Besides, a magnetomotive force (mmf), which alternates at an angular frequency of $2\pi f_b$ and rotates at synchronous speed, is produced when the normal 3-phase current together with an amplitude modulated 3-phase current signal is supplied through the stator coils. The frequency of the modulating signal, represented by f_b, is sometimes called bias frequency of the modulated 3-phase current. The stator current d-axis component, oscillating, induces a current in the field winding which will then be rectified resulting a unidirectional current in the field winding. This unidirectional current excites the field winding without the use of any external field winding excitation (brushes employed) or permanent magnets. The required mmf to produce the field winding flux is produced from this rectified unidirectional current [13].

2.2.2 Voltage Equation

Referring to the circuit in the figure 2.1, the following voltage equations are obtained [13].

$$\begin{aligned} E_d &= R_a i_d - \omega\psi_q + \frac{d}{dt}\psi_d \\ E_q &= R_a i_q + \omega\psi_d + \frac{d}{dt}\psi_q \\ E_f d &= R_{fd} i_{fd} + \frac{d}{dt}\psi_{fd} \end{aligned} \tag{2.1}$$

where:

$$\begin{aligned} \psi_d &= M_{fd} i_{fd} + L_d i_d \\ \psi_q &= L_q i_q \\ \psi_{fd} &= L_{fd} i_{fd} + M_{fd} i_d \end{aligned} \tag{2.2}$$

Denoting the angle between a- and d- axes by θ and assuming that $\theta = 0$ at $t = 0$. θ is expressed as,

$$\theta = \omega t \tag{2.3}$$

where ω is the synchronous speed.

The motor variables in the dq-axes (rotor reference frame) are found from the coordinate transformation, i.e.

$$\begin{bmatrix} E_d \\ E_q \end{bmatrix} = \sqrt{\frac{2}{3}} \begin{bmatrix} \sin\theta & \sin(\theta - \frac{2}{3}\pi) & \sin(\theta - \frac{4}{3}\pi) \\ \cos\theta & \cos(\theta - \frac{2}{3}\pi) & \cos(\theta - \frac{4}{3}\pi) \end{bmatrix} \begin{bmatrix} E_a \\ E_b \\ E_c \end{bmatrix} \tag{2.4}$$

$$\begin{bmatrix} i_d \\ i_q \end{bmatrix} = \sqrt{\frac{2}{3}} \begin{bmatrix} \sin\theta & \sin(\theta - \frac{2}{3}\pi) & \sin(\theta - \frac{4}{3}\pi) \\ \cos\theta & \cos(\theta - \frac{2}{3}\pi) & \cos(\theta - \frac{4}{3}\pi) \end{bmatrix} \begin{bmatrix} i_a \\ i_b \\ i_c \end{bmatrix} \tag{2.5}$$

where:

E_a, E_b, E_c – represent stator winding phase voltages.
i_a, i_b, i_c – represent stator winding phase currents.
ψ_d, ψ_q – are the d- and q- axis fluxes.
i_d, i_q – are the d- and q- axis currents.
E_d, E_q – are the d- and q- axis voltages.
E_{fd} – the field voltage.
i_{fd} – the field current.
ψ_{fd} – the field flux interlinkage.
L_{fd} – the self-inductance of the field winding.
M_{fd} – the mutual inductance.
L_d, L_q – are the d- and q- axis self-inductances respectively.
R_a, R_{fd} – are the winding resistance of the stator and the field winding respectively.

2.2.3 Excitation and Principle of Torque Generation

Suppose that the following amplitude modulated three-phase current is supplied to the 3-phase stator winding,

$$\begin{aligned} i_{af} &= A_f(t)\sin\theta \\ i_{bf} &= A_f(t)\sin(\theta - \frac{2}{3}\pi) \\ i_{cf} &= A_f(t)\sin(\theta - \frac{4}{3}\pi) \end{aligned} \tag{2.6}$$

The right side of these equations, equation (2.6), generates a pulsating and synchronously rotating waveform. Trapezoidal, Sinusoidal and Triangular waveforms are the most common signals to substitute $A_f(t)$ of equation (2.6) as a modulating signals. In order to analyze the effects of the modulating waveforms on the performance of HRreSM, [13] made a comparison study on these three modulating waveforms. The authors finally obtained a better motor power factor and average flux linkage of the field winding by employing triangular waveform than the other two modulating signals. $A_f(t)$ has a frequency (bias frequency) of f_b and peak value of I_f

The the d- and q- axis currents are given by,

$$\begin{aligned} i_d &= \sqrt{\frac{3}{2}} A_f(t) \\ i_q &= 0 \end{aligned} \tag{2.7}$$

Equation (2.7) indicates that the airgap flux produced by equation (2.6) is the same as that produced by a 1ϕ current of magnitude $\sqrt{3/2}A_f(t)$ which flows through the d- axis winding rotating at synchronous speed ω.

From Figure 2.2 of [12], it can be seen that the d-axis mutual inductance (M_{fd}) of the stator and the rotor couples the field winding (W_{fd}) and the d-axis stator winding (W_d). In other words, a d-axis pulsating mmf generated by a pulsating d-axis current (i_d), links both windings (W_{fd} and W_d). In the process, a voltage (V_{fd}) in the field winding, induced by the mmf variation, causes a flowing current in the field winding. Then, this current in the field winding will be rectified by a diode to generate a unidirectional (DC) current for the excitation of the field winding.

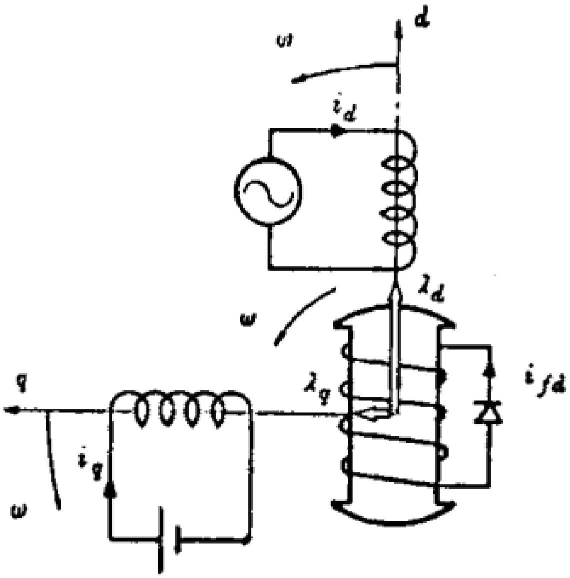

Figure (2.2) Motor principle, [13]

Principle of Torque Generation

The principle of torque generation is illustrated in the figure 2.3, where only the phase 'a' current is represented. The amplitude modulated exciting current produces a d- axis flux inter linkage $M_{fd}i_d$ with the bias frequency ω_b, the diode tends to keep the flux at its maximum value supplying field current i_{fd} [13].

The field flux linkage λ_{fd} is given by the sum of field flux $M_{fd}i_d$ produced by the exciting current and flux

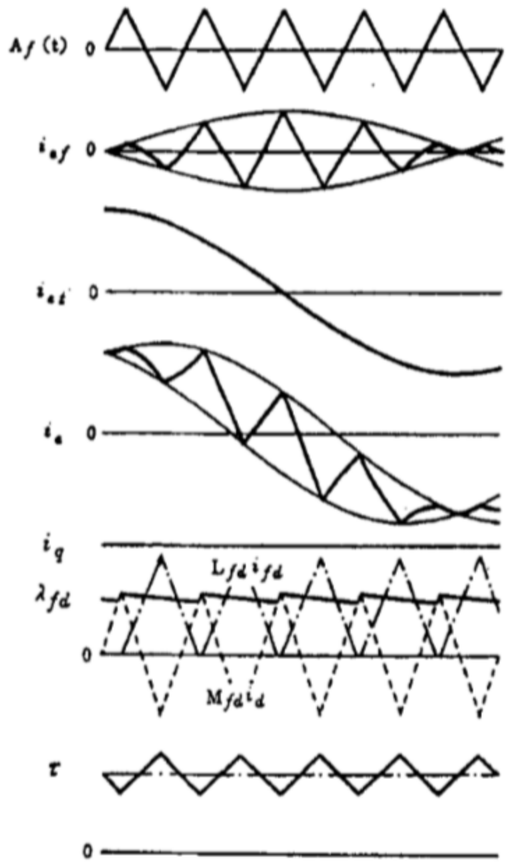

Figure (2.3) Principle of Torque Generation, [13]

$L_{fd}i_{fd}$ produced by the field current. It is almost kept constant as shown in the figure 2.3.

A rotating magnetomotive force (mmf) with constant magnitude can be generated by the torque current component, with peak value of I_t, of the stator excitation. This torque current, given by

$$\begin{aligned} i_{at} &= \sqrt{2} i_t \cos\theta \\ i_{bt} &= \sqrt{2} i_t \cos(\theta - \frac{2}{3}\pi) \\ i_{ct} &= \sqrt{2} i_t \cos(\theta - \frac{4}{3}\pi) \end{aligned} \tag{2.8}$$

is superimposed on the exciting current as given by equation (2.6) or more precisely,

$$\begin{aligned} i_a &= i_{af} + i_{at} \\ i_b &= i_{bf} + i_{bt} \\ i_c &= i_{cf} + i_{ct} \end{aligned} \tag{2.9}$$

Using Park's coordinate transformation, equation (2.9) can be transferred to the dq-axes currents in the rotor reference frame, as shown in equation (2.10).

$$
\begin{aligned}
i_d &= \sqrt{\frac{3}{2} A_f(t)} \\
i_q &= \sqrt{3} I_t
\end{aligned}
\tag{2.10}
$$

The above currents, equation (2.10) produce torque τ of which average value is proportional to the product of λ_{fd} and i_q.

To simplify the discussion, assume that $r_{fd} = 0$ and $A(f)$ is a triangular waveform. Then the stator and rotor flux linkages can be given by,

$$
\begin{aligned}
\lambda_{fd} &= \frac{3}{\sqrt{2}} M_{fd} I_f \\
\lambda_d &= \sqrt{\frac{3}{2}} \sigma L_d A_f(t) + \frac{3}{\sqrt{2}} (1 - \sigma) L_d I_f \\
\lambda_q &= \sqrt{3} LqIt
\end{aligned}
\tag{2.11}
$$

where the value of σ is the leakage coefficient given by

$$
\sigma = 1 - (M_{fd})^2 / L_d L_{fd}
$$

In this case that λ_{fd} is constant, λ_d contains the component which varies with $A_f(t)$ but it is negligible if σ is small. Torque τ is given by

$$
\tau = \lambda_d i_q - \lambda_q i_d \tag{2.12}
$$

or

$$
\tau = 3\sqrt{\frac{3}{2}} (1 - \sigma) L_d I_f + \frac{3}{\sqrt{2}} (\sigma L_d - L_q) A_f(t) I_t \tag{2.13}
$$

The first term of equation (2.13) represents the average torque and the second term is for pulsating component varying with $A_f(t)$. The effect of pulsating torque can be neglecting by setting the bias frequency ω_b at a value much larger than the mechanical resonance frequency [13].

2.3 Space Vector Pulse Width Modulation (SVPWM) Technique

2.3.1 SVPWM Principle of Operation

For most variable speed motor drives, Pulse Width Modulation (PWM) technique is applied to the power electronic converter called inverter (DC/AC converter) in order to generate variable frequency and variable voltage AC waveforms. The input to the inverter is a DC signal, obtained from either a controlled or uncontrolled rectifier or from the battery. When the drive system is supplied from a 3-phase power supply, first there must be a conversion (rectification) of an AC grid to DC and then inversion of the power from the DC to AC. Therefore, an inverter driven motor drive system passes through two stages of power conversion. Initially power electronic converters with analog technology using discrete electronic components, the basic energy processing technique was PWM [16].

The space phasors/ space vectors representation of an inverter output is the basic concept behind SVPWM. I.e. SVPWM implementation realizes the representation of the voltage outputs of an inverter by a space vector. In other words, one rotating space vector (a single quantity) represents the inverter output 3-phase voltage quantities (three quantities)[17]. In contrast to the phasor representation, space vector representation works for both steady state and transient operating conditions. The space phasor representation is valid for steady state operating conditions only.

The space vector can be defined by:

$$f_s = \frac{2}{3}[f_a + e^{j2\frac{\pi}{3}} f_b + e^{j4\frac{\pi}{3}} f_c] \tag{2.14}$$

where f_a, f_b, and f_c can be voltages, currents, and fluxes in three-phase quantity.

In the SVPWM inverter, the voltage space vectors are considered, where the space vector at any given time maintains its magnitude. As the time increases, the angle of the space vector increases, causing the vector to rotate with a frequency equal to the frequency of the sinusoidal waveform. The central idea of SVPWM is to generate an appropriate PWM signals so that a vector, representation of the 3-phase reference voltage, with any desired angle can be generated. When the output voltages of the three-phase six-step inverter are converted to a space vector and plotted on the complex plane, the corresponding space vector takes only on one of six discrete angles of the full switching cycle as time increases.

Since the inverter (three-phase inverter) can attain either $-0.5V_{dc}$ or $+0.5V_{dc}$ (if the DC bus has mid-point), or 0 or V_{dc}, i.e. only two states. In the case of an inverter with only two states, no-mid point DC bus, $8(2^3)$ total possible outputs are obtained (i.e. 111,110,101,100,011,010,001,000). Here 1 and 0 represents the

”ON” and ”OFF” states of the upper switch of an inverter respectively. Therefore, the power flows to the load, connected to the output of the inverter, from the DC link (input to the inverter) in 6-Active switching states. And there is no power flow to the load from the DC link in two zero switching states (111,000). The operations of the lower switches are complimentary to the upper switches. Referring to figure 5.3, voltage quantities V_A, V_B and V_C (called leg or pole voltages of an inverter) attains $-0.5V_{dc}$ when the lower switch is operating and $+0.5V_{dc}$ when the upper switch is operating. V_{an}, V_{bn} and V_{cn} (phase voltages) measured between the leg and the load star point is the one to be supplied to the load.

Figure 5.3 shows the 3-phase VSI circuit diagram, where IGBTs/ Transistors with an anti-parallel power diodes are used as a semiconductor switching devices in the diagram.

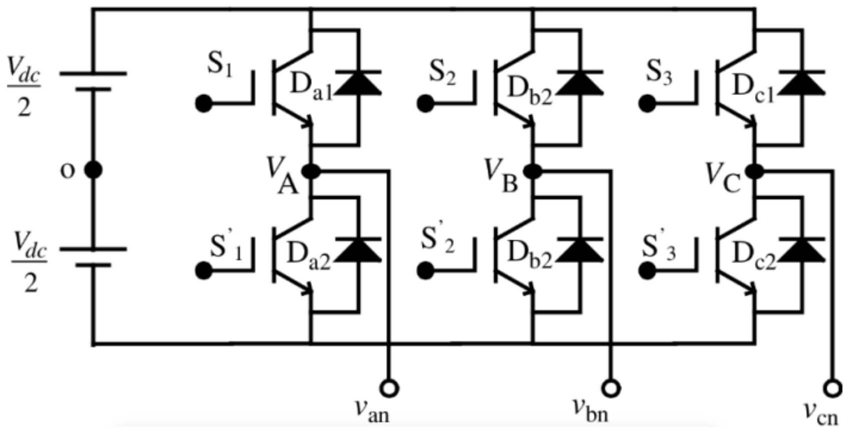

Figure (2.4) 3-Phase VSI, Circuit Diagram, [16]

The relationship between the leg voltage and switching signals can be described as:

$$V_i = V_{dc}S_i;\ i \epsilon A, B, C \tag{2.15}$$

Where S_i stands for a digital value which can have a value of 1 and 0. $S_i = 0$ is for the ’ON’ state of the lower switch and $S_i = 1$ is for the ’ON’ state of the upper switch. Equation (2.16) describes the leg voltage and phase-to-neutral voltage relation, for a star connected 3-phase load.

$$\begin{aligned} V_A(t) &= V_{nN}(t) + V_a(t) \\ V_B(t) &= V_{nN}(t) + V_b(t) \\ V_C(t) &= V_{nN}(t) + V_c(t) \end{aligned} \tag{2.16}$$

In the equation (2.16), V_{nN} is called by the name ”Neutral voltage” or ”Common mode voltage” and it is the difference between the ”the load star point” and ”the DC bus negative rail”. In most cases the source of leakage bearing currents and their subsequent failures is this common mode voltage.

By assuming a balanced 3-phase voltage, add the phase-to-neutral voltages and set their sum to zero (i.e. $V_a(t) + V_b(t) + V_c(t) = 0$, the instantaneous sum is always zero for a balanced 3-phase voltage). By adding each term of equation (2.16), the common mode voltage ($V_{nN}(t)$) becomes $1/3V_A(t) + 1/3V_B(t) + 1/3V_C(t)$. The expressions for phase-to-neutral voltages described in equation (2.17) are obtained by substituting the above common mode voltage expression in equation (2.16).

$$\begin{aligned} V_a(t) &= -\frac{1}{3}[V_B(t) + V_C(t)] + \frac{2}{3}V_A(t) \\ V_b(t) &= -\frac{1}{3}[V_A(t) + V_C(t)] + \frac{2}{3}V_B(t) \\ V_c(t) &= -\frac{1}{3}[V_A(t) + V_B(t)] + \frac{2}{3}V_C(t) \end{aligned} \tag{2.17}$$

Equation (2.17) can also be written in terms of the switching function definition of equation (2.15) and described in equation (2.18).

$$\begin{aligned} V_a(t) &= [2S_A - S_B - S_C]\,\frac{V_{dc}}{3} \\ V_b(t) &= [2S_B - S_A - S_C]\,\frac{V_{dc}}{3} \\ V_c(t) &= [2S_C - S_A - S_B]\,\frac{V_{dc}}{3} \end{aligned} \tag{2.18}$$

The orthogonal coordinates are used to represent a phase diagram of the three-phase two-level inverter. There are eight possible inverter states generating eight space vectors, which are expressed by the following complex vector expressions:

$$\vec{V}_K(t) = \begin{cases} \dfrac{2}{3}\,V_{dc}\;e^{j(K-1)\frac{\pi}{3}} & if \quad K = 1,2,3,4,5,6 \\ 0 & if \quad K = 0,7 \end{cases} \tag{2.19}$$

Using six equal 60^0 sized sectors, the whole space can be divided into six. Two active vectors out of the six Active vectors bound each sector. V_0 and V_7 are two voltage vectors with zero amplitude and they are located at the origin of the hexagon. The eight active and non-active state vectors are geometrically drawn in the figure 2.5(A).

Table 2.1 lists the possible space vectors computed based on equations (2.14) and (2.19). Table 2.1 also con-

Voltage Sectors	Space Vector No.	Switching State	Phase to Neutral Voltages			Line-Line Voltages			Phase to Neutral Voltage Space Vectors
		abc	V_{an}	V_{bn}	V_{cn}	V_{ab}	V_{bc}	V_{ca}	
V_0	7	000	0	0	0	0	0	0	0
V_5	5	001	$-\frac{V_{dc}}{3}$	$-\frac{V_{dc}}{3}$	$\frac{2V_{dc}}{3}$	0	$-V_{dc}$	V_{dc}	$\frac{2}{3}V_{dc}e^{j\frac{4\pi}{3}}$
V_3	3	010	$-\frac{V_{dc}}{3}$	$2\frac{V_{dc}}{3}$	$-\frac{V_{dc}}{3}$	$-V_{dc}$	V_{dc}	0	$\frac{2}{3}V_{dc}e^{j\frac{2\pi}{3}}$
V_4	4	011	$-\frac{2V_{dc}}{3}$	$\frac{V_{dc}}{3}$	$\frac{V_{dc}}{3}$	$-V_{dc}$	0	V_{dc}	$\frac{2}{3}V_{dc}e^{j\pi}$
V_1	1	100	$\frac{2V_{dc}}{3}$	$-\frac{V_{dc}}{3}$	$-\frac{V_{dc}}{3}$	V_{dc}	0	$-V_{dc}$	$\frac{2}{3}V_{dc}e^{j0}$
V_6	6	101	$\frac{V_{dc}}{3}$	$-\frac{2V_{dc}}{3}$	$\frac{V_{dc}}{3}$	V_{dc}	$-V_{dc}$	0	$\frac{2}{3}V_{dc}e^{j\frac{5\pi}{3}}$
V_2	2	110	$\frac{V_{dc}}{3}$	$\frac{V_{dc}}{3}$	$-\frac{2V_{dc}}{3}$	0	V_{dc}	$-V_{dc}$	$\frac{2}{3}V_{dc}e^{j\frac{\pi}{3}}$
V_7	8	111	0	0	0	0	0	0	0

Table (2.1) Line-to-Line Voltages, Phase-to-Neutral Voltages and Phase-to-Neutral Voltage Space Vectors Based on The Switching states, Space Vector Number and Voltage Sectors.

tains the output line-to-line voltages, output line-to-neutral voltages and the eight switching vectors where the output voltages are in terms of V_{dc} computed based on the list of equations from (2.16) to (2.19).

The reference voltage vector V_s^* rotates in space at an angular velocity $\omega = 2\pi f$, where f represents the inverter's output voltage fundamental frequency. When the reference voltage vector passes through each sector, different sets of switches as described in the table 2.1 will be turned 'ON' or 'OFF'. And finally, when the reference voltage vector finishes a rotation of one revolution in space, the outputs of the inverter varies one electrical cycle over time. The rotating speed of the reference voltage vector is going to be inverter's output frequency. The zero vectors and active vectors do not move in space, they are referred to as stationary vectors. Figure 2.5(A) shows the reference vector V_s^* in the sixth sector.

The six active voltage space vectors are shown on the same graph in the figure 2.5 with an equal magnitude of $2V_{dc}/3$ and a phase displacement of 60^o. A hexagon is formed by connecting the tips of the active space vectors. The desired reference voltage vector can be produced by the inverter by decomposing the reference vector into the two adjacent active vectors, for a particular sector, and two zero vectors, located at the center of the hexagon (origin).

The charactristics of SVPWM depends on the value of reference voltage vector $|V_s^*|$ [18]-[19]. When $|V_s^*| = (1/\sqrt{3})V_{dc}$, called linear modulation region where the maximum sinusoidal output of the inverter is achieved and the trajectory is a circle inscribed inside the hexagon. If the value the references vector is greater than $1/\sqrt{3})V_{dc}$, the output is beyond the linear modulation region and the analysis based on linear modulation technique isn't going to be efficient. This operating region of the SVPWM inverter is called the over-modulation region, since the time of application of the zero space vector becomes negative, it does not make any physical sense. The SVPWM inverter enters the over-modulation region for $(1/\sqrt{3})V_{dc} < |V_s^*| < (2/\pi)V_{dc}$. The inverter operates in the square wave mode (six-step mode), when the reference voltage vector is $|V_s^*| < (2/\pi)V_{dc}$, as shown in Figure 2.5 (B).

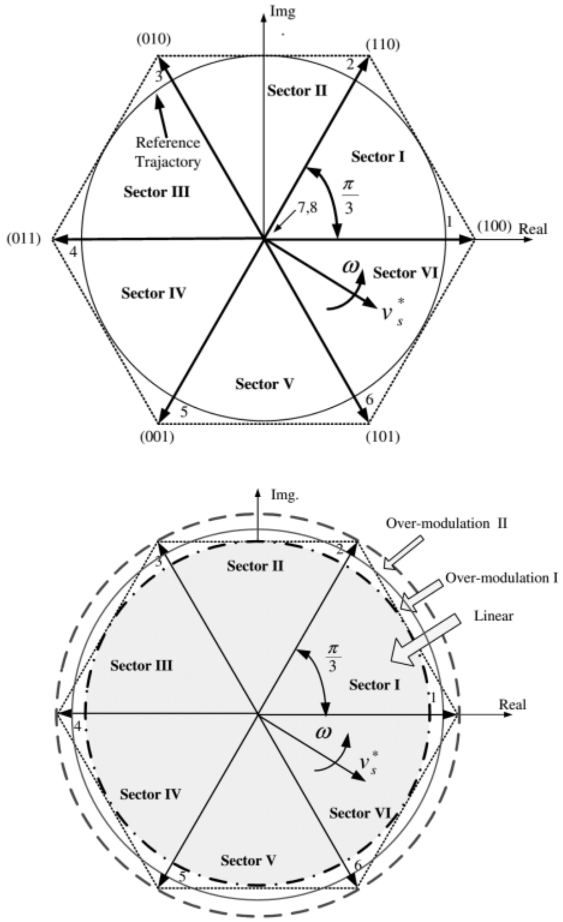

Figure (2.5) (A) Based on the switching states of an inverter allocation of the voltage space vectors on the whole space. (B) Linear and over-modulation range.

The over-modulation region is divided into two sub-regions, the over-modulation region-I (in the range $0.5773 < |V_s^*| < 0.6061$) and the over-modulation region-II (in the range $0.6061 < |V_s^*| < 0.6366$. In over-modulation region-I, the magnitude of the reference voltage vector is altered but the angle is not changed. However, in the over-modulation region-II, both the angle and magnitude of the reference voltage space vector are changed in such a way that it becomes a distorted discontinuous reference voltage space vector [16].

A described above in the linear modulation range the inverter output signals become sinusoidal, where the reference vector follows a circular trajectory. The reference vector trajectory changes when the SVPWM inverter operates in the over-modulation region, i.e. a trajectory identical to the trajectory of the six-step mode inverter, which is at the boundary of the hexagon will be formed.

In SVPWM, for a given sector, from the zero vectors and from the nearest two neighboring active vectors, reference voltage can be computed. The Active vectors are determined from the reference voltage location, which is the reached sector. Therefore, in SVPWM implementation, the vectors to be employed will be known once the location (sector number) is identified.

After identifying the vectors (the active and zero vectors) depending on the reference vector location, the following task is going to be calculating the time of application of each vector, which is called the ”dwell time”. The reference voltage’s magnitude and speed, in SVPWM inverter, is the magnitude and frequency of the output voltage of the inverter respectively.

As shown in the figure 2.5(B), the radius of the largest circle that can be inscribed inside the hexagon is the same as the maximum output voltage of an inverter, which is the maximum modulation index in the SVPWM technique. This maximum attainable SVPWM inverter output voltage is calculated using equation (2.20), from the right-angled triangle of Figure 2.6. The lines joining the ends of the active space vector are tangent to this circle.

$$V_{max} = \frac{1}{\sqrt{3}}V_{dc} = (\frac{2}{3})V_{dc}\cos\frac{\pi}{6} \tag{2.20}$$

In the other case, SPWM inverter generates the maximum possible output voltage of $0.5V_{dc}$. Hence the increase in the output of the SVPWM inverter from the SPWM inverter is $(2V_{dc}/3)/(0.5V_{dc}) = 1.154$.

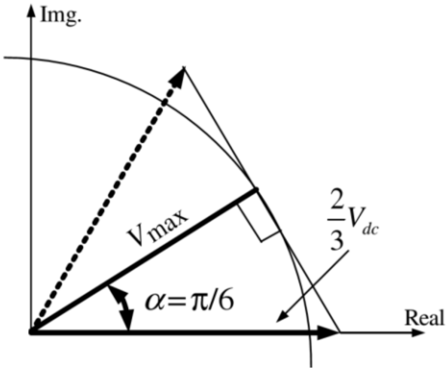

Figure (2.6) Determining the maximum possible output using SVPWM.

The ”equal volt-second principle” is used to calculate the time of application of the different space vectors for each sectors. This principle states, during the switching interval assuming fixed reference voltage, the product of the time of application of the vectors and the applied voltage vectors must be equal to the product of the switching time (T_S) and the reference voltage. For instance, for sector I, from V_0, V_1, and V_2 vectors, the reference voltage can be calculated and t_o, t_a, and t_b are their respective dwell times, see equation (2.21).

$$V_s^* T_s = V_0 t_o + V_1 t_a + V_2 t_b \tag{2.21}$$

where T_s is the switching time, which is the sum of t_o, t_a, and t_b and space vectors are described in the following equation, equation (2.22).

$$V_s^* = |V_s^*| e^{j\alpha} \qquad V_0 = 0 \qquad V_1 = \frac{2}{3} V_{dc} e^{j0} \qquad V_2 = \frac{2}{3} V_{dc} e^{j\frac{\pi}{3}} \tag{2.22}$$

Equation (2.23) can be derived by substitution of equation (2.22) into equation (2.21) and separation of resulting expression's imaginary (β) and real (α) axis components.

$$\begin{aligned} V_s^* \, \cos(\alpha) T_s &= \frac{2}{3} \, V_{dc} \, \cos(\frac{\pi}{3}) \; t_b + \frac{2}{3} \, V_{dc} \, t_a \\ V_s^* \, \sin(\alpha) T_s &= \frac{2}{3} \, V_{dc} \, \sin(\frac{\pi}{3}) \; t_b \end{aligned} \tag{2.23}$$

For sector I, use $\frac{\pi}{3}$ for α.

Solving for the time of application of the space vectors t_a and t_b, dwell time of the vectors, using equation (2.23), the following equations can be obtained.

$$\begin{aligned} t_o &= T_s - t_a - t_b \\ t_a &= \frac{\sqrt{3} \, |V_s^*|}{V_{dc}} \, T_s \, \sin(\frac{\pi}{3} - \alpha) \\ t_b &= \frac{\sqrt{3} \, |V_s^*|}{V_{dc}} \, T_s \, \sin(\alpha) \end{aligned} \tag{2.24}$$

Now let's generalize equations from (2.21) to (2.24) for six sectors. Which gives equation (2.25), where represents the sector numbers, $K = 1, 2, 3, 4, 5, 6$.

$$\begin{aligned} t_o &= T_s - t_a - t_b \\ t_a &= \frac{\sqrt{3} \, |V_s^*|}{V_{dc}} \, T_s \, \sin(\frac{K\pi}{3} - \alpha) \\ t_b &= \frac{\sqrt{3} \, |V_s^*|}{V_{dc}} \, T_s \, \sin(\alpha - (K-1)\frac{\pi}{3}) \end{aligned} \tag{2.25}$$

In SVPWM implementation, determination of the switching sequence is the following step after locating the reference vector position and calculating the dwell time of the zero and active vectors. To reduce switching losses, during the switching sequence synthesis, the minimum number of switching of switching devices of an inverter should be considered. Ideally in one switching period, one power switch should be turned 'ON' and turned 'OFF' .

In each switching periods, for the optimum harmonic performance and to get a fixed switching frequency, each leg should change state only once (either from 'ON' to 'OFF' or 'OFF' to 'ON'). In the first half of the switching period, by applying two adjacent active state vectors after the zero state vectors and in the next half of the switching period by making a mirror image of the first half, a fixed switching frequency can be achieved. Next the switching period T_s should be divided into seven parts, and then first apply the zero vector (000) for $1/4th$ of the total zero vector time, then apply the active vectors for half of their application time and finally apply zero vector (111) for $1/4th$ of the zero vector time. Then the mirror image of the first half will be applied in the next half of the switching period. In this way a symmetrical SVPWM will be obtained. The switching sequences together with the voltage space vectors are shown in figure 2.7 for sectors I to VI.

Based on the switching patterns in figure 2.7, the average leg voltages can be determined. For instance, let's see for sector I,

$$\begin{aligned} V_{A,avg} &= \frac{(V_{dc}/2)}{T_s}\,[t_o + t_a + t_b - t_o] \\ V_{B,avg} &= \frac{(V_{dc}/2)}{T_s}\,[t_o - t_a + t_b - t_o] \\ V_{C,avg} &= \frac{(V_{dc}/2)}{T_s}\,[t_o - t_a - t_b - t_o] \end{aligned} \tag{2.26}$$

Substitute the equation of time of application of the space vectors from equation (2.24) into equation (2.26) and the following equation is obtained for sector I and the same approach is applied to compute for the other sectors.

$$\begin{aligned} V_{A,avg} &= \frac{\sqrt{3}}{2}\,|V_s^*|\,\sin(\alpha + \frac{\pi}{3}) \\ V_{B,avg} &= \frac{3}{2}\,|V_s^*|\,\sin(\alpha - \frac{\pi}{6}) \\ V_{C,avg} &= \frac{-\sqrt{3}}{2}\,|V_s^*|\,\sin(\alpha + \frac{\pi}{3}) \end{aligned} \tag{2.27}$$

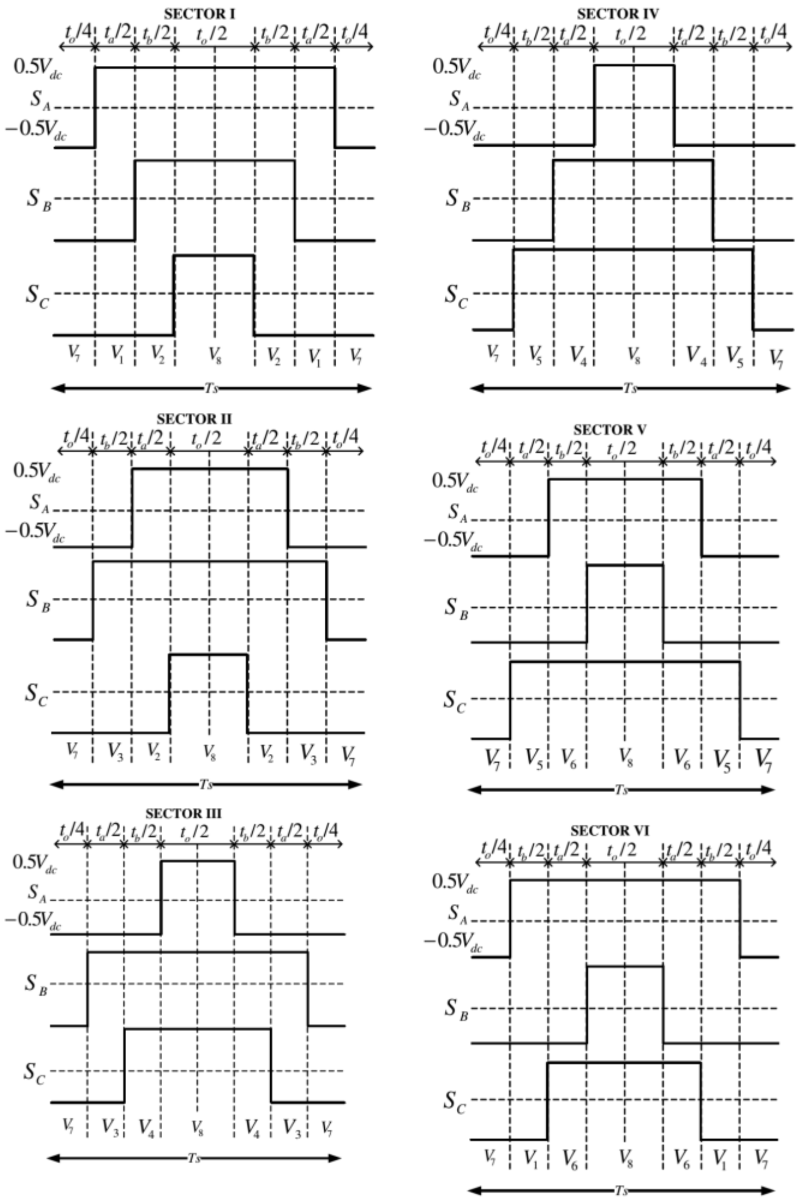

Figure (2.7) Determining the maximum possible output using SVPWM.

2.3.2 Modulation Characteristics and Harmonics of PWM

PWM signals are often evaluated by the percent of DC bus voltage conversion into AC voltage, number of switchings, algorithm efficiency and of course the harmonic distortion present. The maximum DC bus voltage V_{dc} that can be converted to AC in SPWM is $0.5V_{dc}$. According to section 2.3.1, the SVPWM technique converts 57.7% of the DC bus voltage. Since the rated current capabilities of the semiconductor devices remain the same, using SVPWM only increases the power conversion by 57.7%. The ease of implementation of SVPWM in micro-controllers and code efficiency, and changing the state of only one switch unlike SPWM makes the proposed PWM technique even more efficient both power wise and time wise.

The output signals of SVPWM inverter may have a fundamental frequency f (like a sinusoidal signal with frequency f) component and some harmonics components, which are other sinusoidal components at frequencies multiples of the fundamental frequency $(2f, 3f, 4f...)$. Since harmonics can be seen at the output of a system with some non-linearity, the harmonics components should be considered during modeling and control of the system . If the a given system is linear, then the output signal of the system is going to be the linear combination of the input signals having the same frequency as the inputs. These signals are sometimes called linearly dependent signals. The power output of the system with harmonics represents the non-linearity of the system.

Harmonics most of the time are not necessary and cause a distortion to the fundamental frequency component of the signal. The harmonic distortions present in a signal are measured by the Total Harmonic Distortion (THD), which is also called as Distortion Factor. In other words THD of a signal is a measurement of the harmonic distortions present and is calculated as the ratio of the sum of the powers of all harmonic components to the power of the fundamental frequency. Most of the time THD characterizes the linearity of audio systems and the power quality of electric power systems.

THD of a signal can be calculated as a ratio of summation of all harmonic components of the voltage or current signal and the fundamental component of the voltage or current wave as described in the equation (2.28).

$$THD = \frac{\sqrt{(V_2^2 + V_3^2 + V_4^2 + ... + V_n^2)}}{V_1} \tag{2.28}$$

The equation (2.28) shows the calculation for THD value on a voltage signal by comparing the harmonic components to the fundamental component of the voltage signal. The THD value of the signal, in percentage, obtained after applying equation (2.28) for computation, the harmonics distortion level on the signal can be analyzed. The higher the THD value means there is more distortion on the main signal, i.e. fundamental frequency component of the signal.

In power systems lower THD value should be registered from the outputs of the system, which results in reduction in peak currents, heating, emissions, and core loss in motors. Higher temperature in neutral conductors and distribution transformers may occur due to the existence of Unwanted distortions in the power system. In the case of electric motors, higher frequency harmonic components can cause additional core loss in the motor, which results in excessive heating of the motor core. Higher order harmonics in the communication equipments can oscillate at the same frequency as the transmit frequency, which results an interference with communication transmission lines. If left unresolved an increase in temperature and the resulting interference can greatly shorten the life of electronic equipment, cause damage to power systems and electric drive systems [16].

Even if there is no national or international standard dictating THD limits on drive or any other systems, some recommended practices and requirements are given by [20].

2.4 Vector Control

Variable frequency drive (VFD) is necessary in order to run the synchronous motors at different speeds. Based on the quantities to control, there are two man control method categories for an electric motor, vector control and scalar control. The vector control controls both the angle and magnitude of the flux, while the scalar control controls manitude only. To achieve a better dynamic performance of the drive system, controlling both the angle and magnitude of the flux is preferable than the procedures of the scalar control [21]. There are two different types of strategies for vector control, Field Oriented Control and Direct Torque Control. In this section the FOC will be discussed, since it is the main part of this study.

2.4.1 Field Oriented Control (FOC)

Figure 1.1 shows the general block diagram of an FOC of the drive system. In FOC the goal is to independently control the direct- and quadrature-axis currents i_d and i_q to achieve the requested torque. By controlling id and iq independently, it's possible to achieve a Maximum Torque Per Ampere ratio (MTPA) to minimize the current needed for a specific torque, which maximizes the motor's efficiency.

For a non-salient machine, i.e. $L_d = L_q$, the control is easy to implement. From equation (3.1) it can be seen that a motor without saliency cannot produce any reluctance torque. id has therefore no effect on torque production, and it needs to be zero at all times to reach MTPA. The torque curves will be linear in the dq-plane and the MTPA trajectory will be along the quadrature-axis.

For a salient machine, i.e. $Ld \neq Lq$ the control is a bit more difficult to implement since the motor produces both electromagnetic and reluctance torque, see equation (3.1). That's why the torque as a function of current in the dq-plane is no longer linear. To reach MTPA, the minimum distance from the origin to the curve of requested torque has to be calculated.

One critical parameter of FOC is information of the motor's position. The most common way to do this is by using a mechanical sensor coupled to the motor's shaft, this method is called Indirect FOC. Another type is Direct FOC, where the position is estimated from the flux (back EMF vector) [22], or any possible rotor position extraction technique like using high frequency signal injection, carrier frequency component based [15], and so on.

The other critical parameter is the varying values of inductances L_d and L_q as they are constantly changing during different operating conditions due to saturation and etc. The direct axis inductance, which gives the motor a higher salience ratio, is more affected.

Among the various methods to calculate the optimal current trajectory of the MTPA control, some of them are Normalization of variables, saliency ratio and polar coordinates. Normalization of variable as described by [23], is how to normalize the parameters and express the torque equation in a p.u.-system, with the motor parameters eliminated from the equation. The second one is using saliency ratio, by normalizing the variables, introducing the saliency ratio x and short circuit ratio K a modified version of torque equation will be obtained [24]. The other method to find the optimal current trajectory is using a polar coordinates. It works by describing the torque equation using the dq-axes currents [14]. In this paper the last method, polar coordinates, is used for derivation of the optimal dq-axes current components, look at section 3.2 for the details.

Since the FOC allows us to control the d-axis current component of the stator current, the flux producing current component, and the q-axis current independently. The flux weakening (FW) control for high speed operation will be possible by the control of the d-axis current. The FW control can be achieved by direct reduction of the rotor flux linkage or indirectly by adjusting the d- and q- axes currents for the demagnetization of the PM on the rotor. The former FW control technique is applicable for induction motor, separately excited DC motor and HRreSM, look at section 3.3. And the latest FW control technique is for PMSMs.

2.5 Literature Review

2.5.1 Electric Motors for EV Application

The electric motors are key elements in electric vehicles. Selection of traction motors for electric propulsion systems is a very important step that requires special attention and it should be carried out at the system level. In the industrial application point of view, the most common motors used in the hybrid electric vehicles (HEV) and pure electric vehicles (EV) are DC motors, induction motor, permanent magnet synchronous motors, switched reluctance synchronous motors and brushless DC motors. In fact, the automotive industry is still seeking for the most appropriate electric-propulsion system for hybrid electric vehicles (HEVs) and EVs [25]-[26].

The major performance requirements of EV's electric propulsion, as mentioned in past literatures [25] [3], [1], [27] are summarized as a high instant power and a high power density, a high torque for climbing and starting at low speed, as well as a high power at high speed for cruising, including constant-torque region, speed range extension to the constant-power regions, a fast torque response, a high efficiency in the constant torque and constant power regions, a high efficiency for regenerative braking, a high reliability and robustness for various vehicle operating conditions, controllability and a reasonable cost. Based on these requirements let's evaluate the traction motors employed for EV application.

According to [25] DC motors have been important in electric propulsion because of their torque-speed characteristics suits the traction requirement well, and their speed controls are simple. However, DC motor drives have bulky construction, low efficiency, low reliability and high maintenance requirement, mainly due to the presence of mechanical commutator (brushes), even if interesting progress has been made with slippery contacts. [25] also says about the induction motors, due to their reliability, ability to operate in hostile environments, low cost, low maintenance requirement and ruggedness, induction motors (specially squirrel cage IMs) are accepted as the most important candidates for electric propulsion of EVs. Low inverter-usage factor (very important for large motors working in high speed range), low-power factor, low-efficiency and high power loss are the main IM drawbacks. Even if the drawbacks of IM drives are to be considered during design steps, Permanent Magnet (PM) brushless synchronous motors have number of advantages over IM, including (1) overall weight and volume are significantly reduced for a given power output (high power density). (2) they have higher efficiency. (3) heat is efficiently dissipated to the surrounding. Still PM brushless synchronous motors have a short constant power region due to their limited field weakening capability , resulting from the presence of PM field [27]. Power converters' conduction angle must be controlled above the base speed, in order to improve the efficiency of PM brushless SMs and to increase the speed range of operation. But at every high speed range, the efficiency may drop because of the risk of PMs demagnetization. Switched reluctance motors (SRM) are also gaining much interest for an EV applications. The advantages of these motors are their outstanding speed-torque characteristics, simple control, fault-tolerant operation and their simple and rugged construction [28]. There are, however several disadvantages of SRM. Some of them are acoustic noise generation, torque ripples, special converter topology, excessive bus current ripple, and electromagnetic interference noise generation [25].

Several kinds of brushless synchronous motors have been used including the permanent magnet type and reluctance type synchronous motors. However, their capacity is limited by both demagnetization in overload condition and the poor power factor [5]. Interior PM synchronous machines (IPMSMs) have emerged as the brightest candidates, which have been widely used for EV (or hybrid EV) traction. These electric motors may be designed with different rotor topologies, where rare-earth magnet is often employed to achieve high performance [29]. However, the material cost of rare-earth magnet is high and supply is controlled by few countries owning the mineral resources. Some EVs adopt propulsion solutions without rare earth permanent magnet, which uses copper rotor IMs . However, in addition to the drawbacks of IMs mentioned above the starting current of IMs can be high which is disadvantageous for battery duration and the Vector controlled induction motors allow independent control on torque and flux, but the performances are sensitive to the motor parameter variation since the motor flux is estimated using the motor parameters [3],[7]. Randel type and inductor type synchronous motors have complicated magnetic path structure and they are very large because they are excited by the stator winding not on the rotor winding. The ac excitation scheme and rotary commutation scheme are not suited for a variable speed motor. The disadvantage of their rotary transformer scheme is that motor construction is complicated. The structural disadvantage caused by the presence of exciter becomes remarkable as the capacity increases. It is possible to construct a brushless self-excited three-phase commutator less motor by connecting diodes to the field winding [5].

The half-wave rectified brushless synchronous motor or half-wave rectified rotor excited synchronous motor (HRreSM) is the same as conventional salient pole type synchronous motor, but whose rotor winding is short circuited through a diode. HRreSM is a motor of which field winding is excited by a current obtained by rectifying the aforementioned alternating voltage induced in the field winding. In this type of motor the structure is simple and robust because of absence of brushes; once the position of the rotor is identified, the torque current and the excitation currents can be controlled independently; and it is more insensitive to parameter variation [13]. Permanent magnets may be attached on the rotor for additional torque generation. But the torque generation is not fundamentally dependent on the permanent magnets. An emf with bias frequency is induced in the rotor winding of this motor by the mmf which rotates at synchronous speed and pulsates at bias frequency. The field poles are excited by the field current obtained by rectifying this emf with a diode inserted into the field winding. This motor has simple and robust brushless structure and is maintenance free. This motor also provides us with the torque control operation over the speed range from zero to the rated speed [6].

This HRreSM has following special advantages; (1) Non-PM brushless rotor, with field winding short circuited through a diode, is the only different structure in HRreSM as compared to the conventional SM. Thus, the motor is maintenance free, low cost, robust and simple. (2) Since decoupling of the torque curent and excitation current is possible with prior knowledge of the rotor position information, the high speed operation and torque control are much easier in HRreSMs than IMs. (3) Using the supply to the 3-phase stator winding (the peak value of the excitation current), the amplitude of the field winding flux linkage can be determined. Consequently, machine parameter variations due to temperature rise and other factors, don't affect the characteristics of the motor.

By adopting the permanent magnets excitation combined with the half-wave rectified excitation, following additional merits are expected; (1) The excitation current is reduced for a same output and consequently the power factor and the efficiency are improved compared with the motor without permanent magnets. (2) Higher power machine, with combined results of permanent magnet and half-wave rectified excitation than a conventional synchronous motor can easily be designed. (3) Since the field flux can be controlled directly, field weakening control is possible and simple for the high speed range operation of the motor. (4) The demagnetizing force to the permanent magnet doesn't exist and thus rotor structure design is very easy and simple, as the rotor is always excited in one direction because of a diode. (5) Cogging torque can be decreased,because the sinusoidal field flux distribution can be designed by positioning the permanent magnets and the field winding properly [7]-[8]. Therefore, since HRreSM includes all the necessary performance requirements of EV describes above, it is proposed and studied for modeling and sensorless control under this research paper.

2.5.2 FOC of HRreSM

The 3-phase AC machines including the proposed HRreSM represent a mathematically complicated construct with its multi-phase winding and voltage system, which made it difficult to maintain the important decoupling and independent control of the flux and torque forming current components. Thus, the aim of the field orientation can be defined to re-establish the decoupling of the flux and torque forming components of the stator current vector. The field-orientated control (FOC) scheme is then based on impression the decoupled current components using closed-loop control [30]. Control strategy of maximum torque per ampere (MTPA) with in the FOC is simple in structure and has the straightforward goal of minimizing the stator current amplitude for a given load torque. It has long been recognized that for a given load torque, it is possible to adjust the d-q axis component of input current so as to maximize the output torque. It results in the minimization resistive and core losses thus maximizing the efficiency of the motor drives for a particular operating point [9]. In the MTPA strategy, the two-axis stator reference currents are calculated so that the maximum torque per ampere will be achieved [10]-[11].

Conventional AC motors, used in many industrial applications are normally equipped with a rotor position sensor and a speed sensor. But sensors have many disadvantages such as cost, less reliability and sensitivity of external temperature etc. Many remarkable works have been done to realize sensorless drive system. Most sensorless systems utilize amplitude and phase of emf as the rotor position information source and have some difficulties in low-speed region where emf becomes very low [7]. Interior permanent magnet motors position information is attached to stator inductance (due to magnetic saliency) and back electromotive force (EMF). Consequently, control of such motors without a mechanical rotor position detector is generally based on rotor position estimation from measured or estimated values of either or both of these two electrical quantities [15]. [15] referring [31], [32] claims, For rotor speeds of about 10% base speed and above the back EMF can be estimated from measured fundamental stator terminal quantities using motor models and has been effectively used to estimate rotor speed and position. For lower speeds, the back EMF is very small resulting in unstable control. By referring [33], [34], [35], [32], [36] and [37], [15] described that Rotor position estimation from stator inductance variation with rotor position is effective in the lower speed range including zero speed. Various methods of inductance estimation and rotor position extraction from it have been reported recently. High-frequency signal injection or utilization of inverter switching-frequency component signals are the most common methods to estimate or calculate the inductance and, hence, the rotor position. In high-frequency signal injection, injected signal frequency has to be chosen between the inverter switching (carrier) frequency and motor fundamental frequency. If the injected signal frequency is decreased it can cause torque ripple and acoustic noise. If it approaches the inverter switching frequency it becomes difficult to filter it out. Furthermore, controller bandwidth is limited by the injected signal frequency. And finally [15] present a novel rotor position formulation method , Carrier Frequency

Component (CFC) Method, using the pulse width-modulated (PWM) inverter switching-frequency component signal itself is as the rotor position information source with no additional signal injection is required.

2.5.3 MATLAB/ Simulink to Simplorer interfacing

As demonstrated by [38], modeling with an interface for linking the simulation systems, Simplorer and MATLAB/Simulink, makes the use of the specific advantages of either simulation package to examine the interactions between different subsystems of complex drive systems possible.

After introducing simulation of induction motor drive by using three softwares, Simulink, Simplorer and Maxwell, [39] concluded that, it is very difficult for any user to predict the real behavior of the AC drive with the MATLAB/Simulink simulator. Based on their results, the Ansys Maxell and simplorer simulators are suitable for simulation platform for induction motor drive which will reveals to better performance and advanced simulations for the electric machines and drives. The simulation of induction motor drives in MATLAB/Simulink has been used commonly for a long time. MATLAB/ Simulink software provides a suitable environment for design of controller because of various mathematical tools. But the model on this software for power electronics and motor is ideal which does not provide the practical behavior. On the other hand, Maxwell is design software for electrical motor, but its facilities are very limited for design of drives and controller. In this way, users of these two softwares, MATLAB/Simulink and Maxwell, can't simulate the practical behavior of controller, drive and motor all together and therefore, their simulation will not be close to reality. Modeling power electronic circuit using Simplorer software is very accurate and it provides an interface connection between Simulink and Maxwell that these three softwares can run all together. A direct torque control of induction motor drive has been implemented to demonstrate the efficiency of a model developed using three integrated simulation softwares [39].

The paper [40] deals with modulation of voltage control technique using MATLAB and Simplorer simulation environments, thus regulating the converter output current and voltage. And the simulation results indicate that this control technique on an integrated simulation softwares environment, provides robust output current and voltage of step up converters and is more feasible for their chopper up conversion technique.

2.5.4 Related Works

This study is an extension of a research paper made by [12]. The authors in [12] perform the modelling and control of a half-wave rectified rotor brushless synchronous motor (HRreSM). They used a finite element method to verify the principle of operation of the motor on COMSOL Multiphysics. And in their study, for Matlab/ Simulink simulations of control system a simplified analaytical model and Simscape based models are developed. Their results from these three models was, for a fixed bias frequency fb (the frequency of the modulating triangular waveform), the amplitude of the field current I_f and the field flux linkage are linearly related. The other result is the decoupling nature of the field flux and torque currents of the HRreSM allowed implementation simple PI based speed and current controller. and mainly the authors verify the motor's capability of wide speed range operation.

The rotor position extraction method of this thesis is directly related to a novel study made by [15]. [15] demonstrated the extraction of rotor position from carrier frequency component of the stator current. The carrier signal is injected to the stator through triangular waveforms of the sinusoidal pulse width modulation SPWM. The frequency of the carrier signal is chosen in such a way that, it is in the range of the inverter's switching frequency and well above the fundamental operating frequency of the motor under study. The rotor's position is, then, extracted from the stator currents. These currents indirectly contain the inductance values L_q and L_d, from which the rotor position can be determined. For the position to be determined, two stationary reference frames were defined. According to this paper, one of the stationary reference is $\alpha - \beta$ frame, where the α axis is aligned with the d-axis stator current, and the other frame, $k - l$, which is 45^0 behind the $\alpha - \beta$ frame. Before the three phase currents are transformed into the two stationary frame values, they must have been filtered in the carrier frequency range.

[7] realize a complete sensorless system which can operate in speed range from standstill to rated speed, using HRreSM, which the author proposed for the servo motor. The concept used by the authors for rotor position formulation is, if there is any displacement between the axis of rotating mmf and the axis of the rotor, the impedance of the field circuit varies, therefore the rotor position can be detected only by measuring bias frequency components of armature voltage. And the authors verify that this method of rotor position estimation can provide a whole sensorless control (position and speed sensorless) over the speed range from zero to the rated speed.

[21] Designed and Simulated a control system for a Permanent Magnet Synchronous Motor with Positive Saliency by implementing a direct torque control and field oriented control methods. The FOC and direct torque control methods were chosen by the author and were implemented and simulated together with the newly developed motor in MATLAB Simulink to evaluate their performance. Their simulation results show that there is no difference in performance of the two methods, except there is a difference in efficiency. This paper is related to our thesis, in a way that the author in [21] uses a PM synchronous motor with positive saliency, i.e., $L_d > L_q$, and our candidate motor is also with positive saliency. And in the FOC of the [21], the author employs the MTPA control method for maximum torque generation. This thesis also adopts the same MTPA control strategy of [21].

Chapter 3

MTPA based High Speed Operation and Principle of Rotor Position Extraction for HRreSM

3.1 Introduction

This chapter is the main source of knowledge for the understanding of the developed control model in this paper. This chapter provides answers for What MTPA control strategy is?, How to drive the HRreSM above the rated speed for wide speed range operation?, and How to find the rotor flux position in the development of FOC.

Since EVs, require higher torque performance during the start-up and during acceleration, MTPA control strategy is used for generating maximum torque while minimizing the required stator current value. The concept of MTPA and the way of generating optimal dq-axes current components are discussed in the second section of this chapter. Once the motor passes the rated speed, it is necessary to weaken the rotor flux for the extension of the motor operation in the wider range. So FW control is used for wide speed range operation of the HRreSM. The concept behind FW control and the way to reduce the rotor flux linkage value is discussed in the third section of this chapter. The fourth section is the discussion of the transmission of control, to smoothly transform the control operation from MTPA to FW at the base speed.

In FOC of HRreSM, the independent control of d- and q- axes currents for the independent control of torque and rotor flux is possible. But there is a very important component, the rotor flux position, which is necessary for the decoupling of the stator currents to the dq-axes current components. So, In this paper, the bias frequency component based rotor position extraction method is used. The last section of this chapter clearly shows the process of rotor position formulation using bias frequency component based method.

3.2 Maximum Torque per Ampere (MTPA) Control Strategy

The MTPA control strategy provides maximum torque for a given current. So the copper-loss for a given torque is minimized [22]. The three requirements for the instantaneous torque control of SM can be written as follows: (1) The space angle between the field flux- and the torque-producing current is always 90 degrees. (2) Both the rotor (field) flux and the torque-producing currents can be controlled independently. (3) The torque-producing current has to be controlled instantaneously [14].

Now let's look at how we can meet these three requirements for a HRreSM. For the vector control of a HRreSM, it is important to fulfill the requirement 1, i.e., to maintain the space angle between the field flux- and torque- producing current at 90 degrees. For that to happen, it is necessary to first transform the three-phase abc stator currents into two d-q axes currents. When transforming, the d-axis current is the rotor flux-producing current while the q-axis current becomes the true torque-producing current, which is orthogonal to the rotor flux-producing current. In HRreSM the field winding flux is rotating at the same speed as the rotor speed ω_r, synchronous speed. This implies that the transformation of the stator current must be into the rotor reference frame ($d^r - q^r$ axis). Such transformation requires the rotor position θ_r, i.e. the position of the field winding flux. This can be obtained from the position sensors such as a resolver or an absolute encoder, or the rotor position can be estimated by applying one of rotor position estimation techniques.

For HRreSM, requirement 2 for the instantaneous torque control can be inherently fulfilled . As described above, in HRreSM the field flux of the rotor is produced by the d-axis stator current component. thus, the field flux and the torque producing currents can be controlled independently. In addition, the torque-producing current (q-axis) can be controlled simultaneously by synchronous reference frame current regulator (PI Controller) and the PWM inverter and thus can satisfy the requirement 3.

Now let examine the vector control strategy for a HRreSM with $L_{ds} \neq L_{qs}$. The torque of HRreSMs consists of two terms as,

$$T_e = \frac{3}{2}\frac{P}{2} i^r_{qs}[(L^r_{ds} - L^r_{qs}) i^r_{ds} + M_{fd} i_{fd}] \tag{3.1}$$

Equation 3.1 consists of two terms, the first term represents the magnetic torque (by the field winding current) and the second term is a reluctance torque which is produced by the difference between the inductance values of the two axes. To produce the reluctance torque, both the d- and q- axes components of the stator current are required. Most commonly the q-axis inductance L^r_{qs} is typically larger than the d-axis inductance L^r_{ds}. Thus the d-axis current must have a negative polarity, for the reluctance torque to be added to the torque created by the field current, i.e., $i^r_{ds} < 0$. The stator current of an HRreSM needs to be divided into d-and q-axes components as shown in Fig. 3.1 [14].

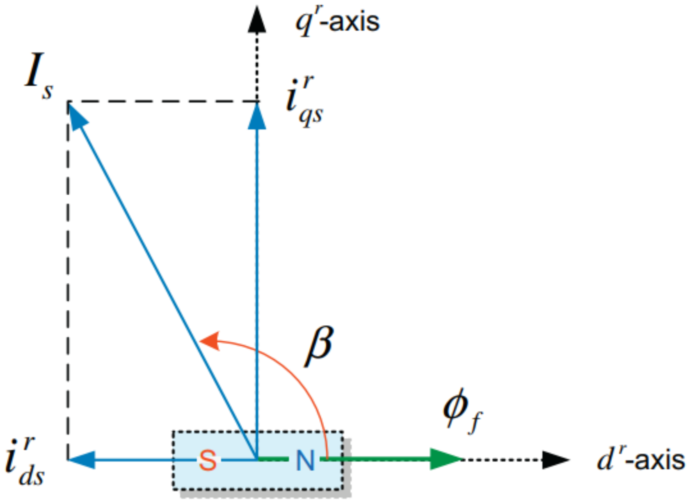

Figure (3.1) d-q currents in the vector control of an HRreSM.

In this case, we need to know how the stator current is divided into the d-and q-axes stator currents properly to produce the MTPA. These optimal currents can be obtained as follows.

As seen in Eq. 3.1, there are many different combinations of d- and q-axes currents that produces the same torque. Fig. 3.2 shows the curve consisting of these currents [14]. Among these combinations, there is an optimal one that gives the smallest stator current. This optimal combination is the point M,$I_{sc}(i^r_{ds0}, i^r_{qs0})$, at which the circle with a radius of I_{so} is tangent to the curve. If an HRreSM operates with the d-and q-axes currents at this optimal point, then it can produce the MTPA. Such operation method with the optimal combination of d-and q-axes currents that leads to the smallest stator current for producing the given torque command is called the MTPA control. The optimal combination of the d-and q-axes currents varies with the required torque.

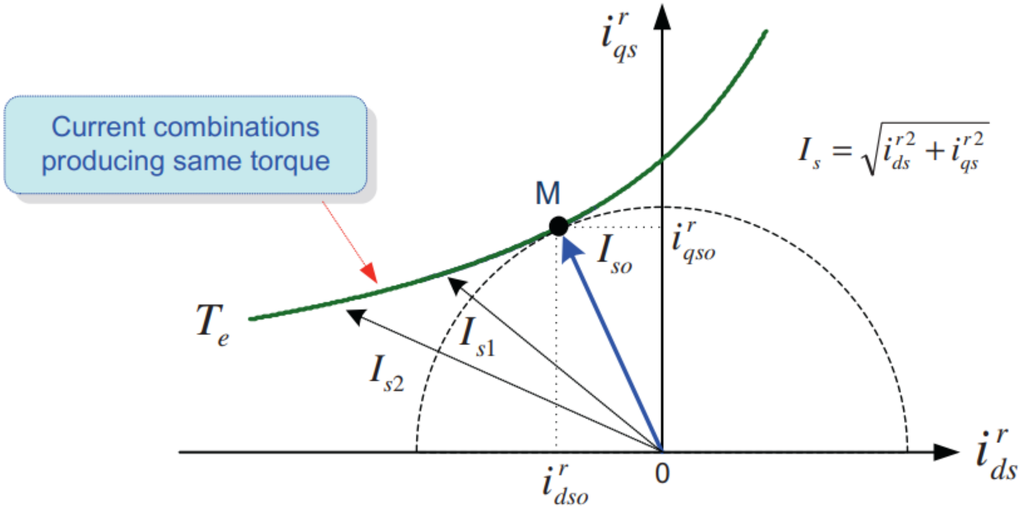

Figure (3.2) Curve consisting of current combinations producing the same torque.

Now we will find out the optimal combination of d-and q-axes currents for a given torque command [23]. In a speed controller the command to produce the output torque is often given as a stator current. For this stator current command I_s, we can obtain the d-q axes stator current commands for the MTPA operation as follows [41]. The torque expression of Eq. 3.1 can be rewritten as a function of the stator current I_s^* as

$$T_e = \frac{3}{2}\frac{P}{2}[(M_{fd}i_{fd})I_s^* sin\beta + \frac{(L_{ds} - L_{qs})}{2} I_s^{*2} sin2\beta] \tag{3.2}$$

where β denotes the angle between the d-axis and I_s^* the stator current vector is as shown in Fig. 3.1.

The $\beta_{optimal}$ for producing the maximum torque can be obtained by solving $dT_e/d\beta = 0$ as show in the equation 3.3 [21].

$$\begin{gathered}\frac{dT_e}{d\beta} = \frac{3}{2}\frac{P}{2}[(M_{fd}i_{fd})I_s^* cos\beta + (L_{ds} - L_{qs})I_s^{*2} cos2\beta = 0] \\ \beta_{optimal} = cos^{-1}\left(\frac{(M_{fd}i_{fd}) - \sqrt{(M_{fd}i_{fd})^2 + 8(L_{ds} - L_{qs})^2 I_s^{*2}}}{4(L_{ds} - L_{qs})^2 I_s^*}\right)\end{gathered} \tag{3.3}$$

From $\beta_{optimal}$, the optimal d- and q-axes current commands are given as

$$\begin{aligned} i^r_{ds0} &= I^*_s cos\beta_{optimal} \\ &= \frac{(M_{fd}i_{fd}) - \sqrt{(M_{fd}i_{fd})^2 + 8(L_{ds} - L_{qs})^2 I^{*2}_s}}{4(L_{ds} - L_{qs})} \\ i^r_{qs0} &= I^*_s sin\beta_{optimal} \\ &= \sqrt{I^2_{smax} - i^r_{qs0}} \end{aligned} \tag{3.4}$$

where i_{smax} is the rated current from the inverter rating.

To obtain the optimal currents for the MTPA operation by using the methods just mentioned, the exact knowledge of stator inductances and magnetic flux is necessary. The magnetic flux varies considerably with the operating temperature. In addition, each inductance value of d-q axes depends on the magnitude of the current of each axis.

Furthermore, it is also known that each inductance of d-q axes may change with the current of the other axis due to cross-saturation effect between the d-q axes [14]. Therefore the exact knowledge of the inductances and magnetic flux at various operating conditions is very important for a successful fulfillment of the MTPA control.

3.3 High Speed Operation of Half-Wave Rectified Rotor Excited Synchronous Motor

As discussed in the subsection A.2 of this paper, the nature of HRreSM favors the high speed operation, it can widely be used for applications requiring a wide speed range operation like an electric vehicle application. Now let's discuss the techniques and strategies of high-speed operation for HRreSM.

According to [14] for motors such as an induction motor, separately excited DC motor, and Half-wave rectified rotor exited SM without PM on the rotor, the field flux can be reduced directly by controlling the field current for high-speed operation. This technique is referred to as classic field-weakening control. By contrast, for PMSMs such as IPM synchronous motors or SPM synchronous motors, the field flux cannot be fully controlled by directly reducing the field winding current because it is generated by a permanent magnet as well as the current in the field winding. On this paper, the first method of flux weakening is discussed and demonstrated.

3.3.1 Classic FW Control

Flux weakening control of HRreSM is possible by direct reduction of the field current since the field winding flux linkage is linearly related to the d-axis component of the stator current [12].

The operation region of HRreSMs can be normally divided into the following two speed regions.

- Constant torque region: Speed range below base speed
- Constant power region: Speed range above base speed (flux-weakening region)

Fig. 3.3 shows the characteristics in two speed regions [14].

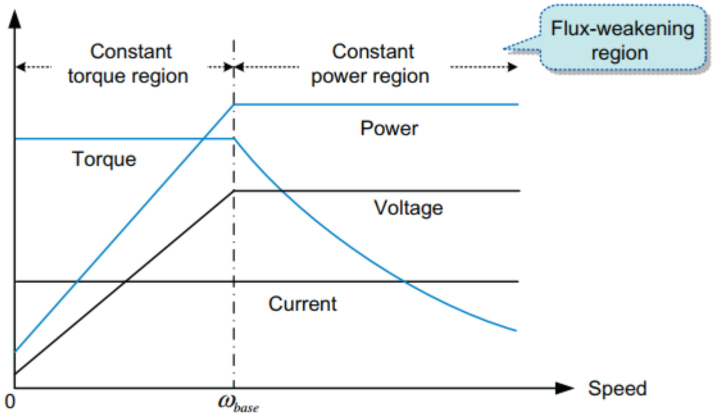

Figure (3.3) Operation regions of HRreSM.

Before examining the high-speed operation of an HRreSM, we will first review the operation of an HRreSM in the constant torque region.

Constant Torque Region($\omega_e < \omega_{base}$)

For the operation of an HRreSM in the constant torque region, which indicates an operating range below the base speed, the MTPA control is used, as shown in Fig. 3.4 [14].

In Section 3.2, we discussed how to obtain the optimal currents for the MTPA operation. In the MTPA operation, the output torque of a HRreSM is mainly limited by only the maximum available stator current $I_{s\ max}$. However, for the high speed range, where the back-EMF voltage becomes large, the voltage margin is insufficient to control the current commands for the MTPA operation. Thus the output torque of an HRreSM is limited by the available voltage rather than the available current.

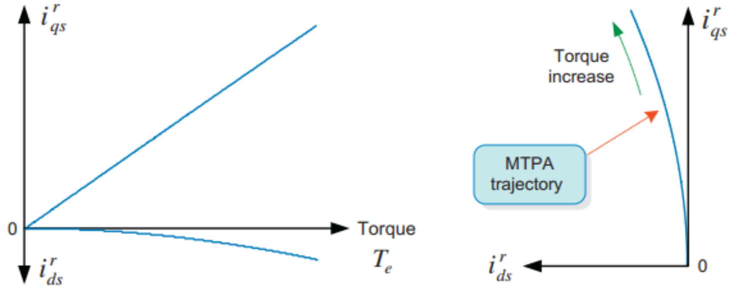

Figure (3.4) d-q axes current commands for MTPA operation.

Now we will examine the speed attainable under the maximum available stator voltage E_{s_max}.

Base Speed Determination

According to [12], for a given rated dq-axes current values and rated voltage value of E_{s_max}, ω can be solved from the voltage limit curve ellipse equations, after that ω_b (the base speed) will be determined. First let's start from the voltage limit equations.

$$E_d \approx -\omega\psi_q + \frac{d}{dt}\psi_d \tag{3.5a}$$

$$E_q \approx \omega\psi_d + \frac{d}{dt}\psi_q \tag{3.5b}$$

Then use

$$i_{fd} \approx \frac{3}{2}\frac{M_{fd}}{L_{fd}}\left(I_f - i_d\right) \tag{3.6a}$$

$$\psi_d = M_{fd}i_{fd} + L_d i_d \tag{3.6b}$$

$$\psi_q = L_q i_q \tag{3.6c}$$

Now substitute the later equation list into the former.

$$\begin{aligned} E_d &= -\omega L_q i_q + \left(L_d - \frac{3}{2}\frac{M_{fd}^2}{L_{fd}}\right)\frac{d}{dt}i_d \\ &= R\frac{d}{dt}i_d + \omega S i_q \end{aligned} \tag{3.7a}$$

$$\begin{aligned} E_q &= \left[\frac{3}{2}\frac{M_{fd}^2}{L_{fd}}I_f + \left(L_d - \frac{3}{2}\frac{M_{fd}^2}{L_{fd}}\right)i_d\right]\omega \\ &= \omega\left(Ri_d + TI_f\right) \end{aligned} \tag{3.7b}$$

where

$$R = -\frac{3}{2}\frac{M_{fd}^2}{L_{fd}} + L_d \tag{3.8a}$$

$$S = -L_q \tag{3.8b}$$

$$T = \frac{3}{2}\frac{M_{fd}^2}{L_{fd}} \tag{3.8c}$$

Now write $E_{s\_max}^2 = E_d^2 + E_q^2$ can be written as

$$E_{s\_max}^2 = \left(R\frac{d}{dt}i_d + \omega S i_q\right)^2 + \left(Ri_d + TI_f\right)^2 \omega^2 \tag{3.9a}$$

or

$$0 = -E_{s\_max}^2 + \left[S^2 i_q^2 + \left(Ri_d + TI_f\right)^2\right]\omega^2 + \left(2RSi_q\frac{d}{dt}i_d\right)\omega + \left(R\frac{d}{dt}i_d\right)^2 \tag{3.9b}$$

Solve for ω using equation (3.9b) using the quadratic root formula.

$$\omega = \frac{-2RSi_q\frac{d}{dt}i_d \pm \sqrt{\left(2RSi_q\frac{d}{dt}i_d\right)^2 - 4\left[\left(Ri_d + TI_f\right)^2 + S^2 i_q^2\right]\left[-E_{s\_max}^2 + \left(R\frac{d}{dt}i_d\right)^2\right]}}{2\left[\left(Ri_d + TI_f\right)^2 + S^2 i_q^2\right]} \tag{3.10}$$

The base speed ω_b is the rotor electrical speed at which the stator voltage reaches the maximum value of V_{s_max} when supplied with rated stator current. Then the based speed calculation can be performed by using equation (3.11) [12].

$$|\omega_b| = \frac{-8RSI_tI_ff_b + \sqrt{\left(8RSI_tI_ff_b\right)^2 - 4\left[\left((R+T)I_f\right)^2 + S^2 I_t^2\right]\left[-E_{s\_max}^2 + \left(4RI_ff_b\right)^2\right]}}{2\left[\left((R+T)I_f\right)^2 + S^2 I_t^2\right]} \tag{3.11}$$

Constant Power Region ($\omega_e > \omega_{base}$)

The proposed FW control method is an old method used for the wide speed range operation of induction motors. It is to simply vary the flux-producing current, i.e., d-axis stator current i_{ds} in proportion to the inverse of the motor speed ω [14].

$$i_{ds}^* = I_{d\_rated}\frac{\omega_{base}}{\omega} \tag{3.12}$$

Where, ω_{base} is the base speed and I_{d_rated} is the rated d-axis current.

For HRreSM the d-axis stator current should always be modulated by a triangular signal in order to provide the a better field winding flux linkage. The amplitude and period of the modulated signal are I_f and $T_b = 1/T_b$ as discussed in section 2.2, the modulated d-axis current is described as shown in equation A.1. Using this modulated d-axis current, the rotor flux command according to the speed in the field-weakening region is given by equation 3.14 and 3.15.

$$i_d(t) = \begin{cases} I_f + \dfrac{-4I_f}{T_b}t & ; 0 \leq t \leq \dfrac{T_b}{2} \\ \\ -3I_f + \dfrac{4I_f}{T_b}t & ; \dfrac{T_b}{2} < t \leq T_b \end{cases} \tag{3.13}$$

$$\psi_{fd} = \frac{3}{2}M_{fd}i_d + L_{fd}i_{fd} \tag{3.14}$$

To simplify the discussion, assume $R_{fd} = 0$ [13]. Then

$$\psi_{fd} = \frac{3}{\sqrt{2}}M_{fd}i_{fd} \tag{3.15}$$

Refer the appendix A for detail derivation of the field current.

Flux weakening i_q calculation

For motor in the flux weakening control region first based on I_{f_max} and the speed ω, I_f can be determined. Then solve for i_q using equation 3.9a and the obtained I_f value [12]. Thus the q-axis current in the flux weakening region is given by,

$$i_q = \frac{-R\frac{d}{dt}i_d \pm \sqrt{E^2_{s\_max} - \omega^2 I_f^2 (R+T)^2}}{\omega S} \tag{3.16}$$

The ellipse is used as the limiting curve determines the sign of $\dfrac{d}{dt}i_d$. The voltage limit is determined by the lower ellipse corresponding to $\dfrac{d}{dt}i_d = -4I_f f_b$, If the value of i_q is positive. Since the sign of B is negative, the sign of the square root must be negative To give positive i_q value [12].

Therefore,

$$i_q = \frac{4Rf_bI_f - \sqrt{E^2_{s\_max} - \omega^2 I_f^2 (R+T)^2}}{\omega S} \tag{3.17}$$

3.4 Transition of Control Mode

In this section, control mode transition from constant torque region, MTPA control mode, to constant power region, FW control mode, will be discussed shortly.

From fig: 3.5 the torque command, T_{ref} is decided from the speed error ($\omega_{ref} - \omega_r$) through the proportional-integral (PI) compensator. The d- and q- axes currents are decided in the MTPA region or in the flux-weakening region according to the torque command. The transition of both control modes is determined according to the following flowchart shown in fig: . Below the base speed ω_{base}, since the voltage limit ellipse is large enough to encompass the current-limit cycle, the MTPA control mode constrained with current limit cylce only will be employed. And above the base speed the flux-weakening control mode is selected since MTPA trajectory is outside the voltage-limit cycle(i.e., the voltage limit ellipse shrinks as the speed increases above the base speed($\omega_r > \omega_{base}$)).

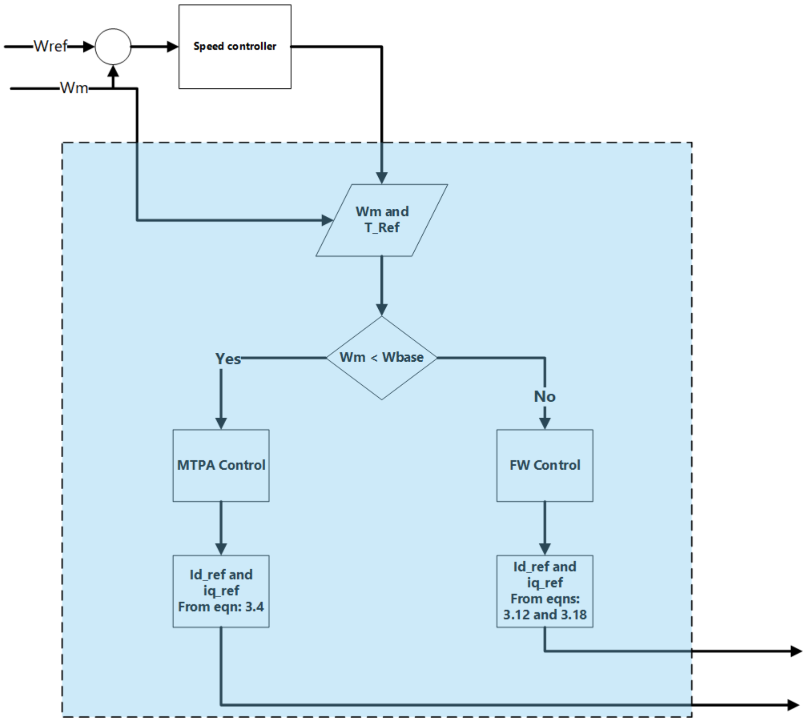

Figure (3.5) Transition of Control Mode.

3.5 Rotor Position Extraction Principles

The rotor position of HRreSM is to be extracted from the bias frequency component of stator currents. This bias frequency is a frequency of a triangular modulating waveform which superimposes itself to the stator current of HRreSM in order to increase the average field winding flux linkage [13]. The rotor position will then be extracted from this component, which indirectly contains the value of the inductance values.

In this paper, the bias frequency component of the stator current itself is used as the rotor position information source. No additional signal injection is necessary. A very effective rotor position extraction method using a pair of reference frames is employed, enabling rotor position extraction even when the saliency (L_q/L_d) level is small and the bias frequency is high. This method of rotor position formulation is a direct adoption of Carrier Frequency Component (CFC) based rotor position extraction of [15].

3.5.1 Inductance Variation

Fig. 3.6(a), shows a HRreSM motor modeled as a salient-pole synchronous motor. Its air gap is stretched and shown in Fig. 3.6(b). For a sinusoidal distributed stator winding and the rotor d-axis aligned with phase-u winding axis (commonly phase-a winding axis), stator inductance $(L_s(\theta))$ distribution is shown in Fig. 3.6(b) and can be given by equation (3.18) [15].

The stator inductance varies between the maximum value (L_q) and minimum value (L_d) depending on the rotor angle of the stator from the rotor axis. A very attractive rotor position equation can be obtained if we consider equation (3.18) at four spatial positions as it is going to be described in Section 3.5.2.

$$L_s(\theta) = L_{sum} - L_{diff} cos(2\theta) \tag{3.18}$$

Where $L_{sum} = 0.5(L_q + L_d)$ and $L_{diff} = 0.5(L_q - L_d)$

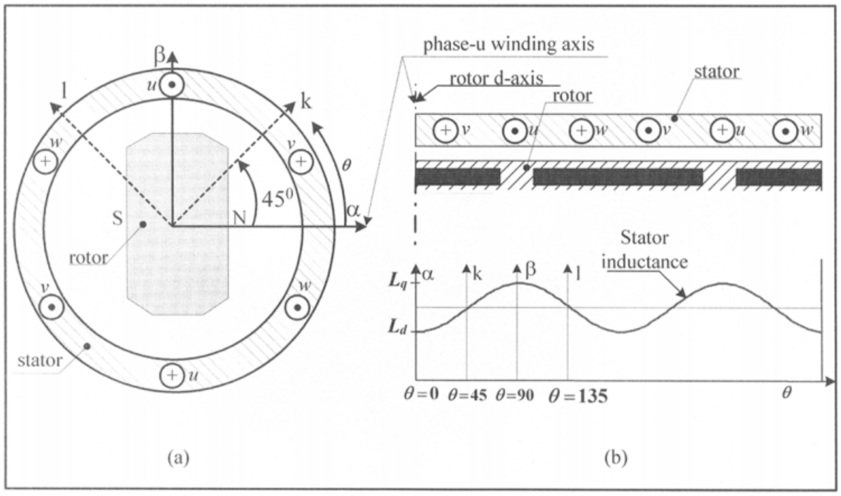

Figure (3.6) (a) HRreSM motor as a salient synchronous motor. (b) Stator winding inductance distribution, [15].

3.5.2 Definition of Two Reference Frames

By using two reference frames the rotor-position-dependent part of the stator inductance can be doubled, while the constant part can be canceled out. In Fig. 3.6, two stationary reference frames ($\alpha - \beta$ and $k - l$) are shown. The real axis of the first reference frame (α axis) is aligned with the rotor d-axis. The other reference frame is 45^o in the forward rotation direction from the first reference frame.

Now let's assume, the rotor has moved counterclockwise by angle δ from the initial position, as shown in Fig. 3.7(a) and (b). The inductance values at the four axes, L_α, L_β, L_k and L_l at the α-axis, β-axis, k-axis and l-axis, respectively, can be expressed as shown in equation (3.19) by inspecting Fig. 3.7(b).

Subtracting L_α from L_β and L_k from L_l of equation (3.19) the constant parts of the inductance values cancel out while the rotor-dependent part doubles as given in equation (3.20). From equation (3.20), δ can be expressed as equation (3.21) in terms of the inductance relative values at the four axes. Note that δ is the angle between the rotor d-axis and α-axis on the stator, and is zero on the α-axis. The α-axis can be chosen arbitrarily on the stator.

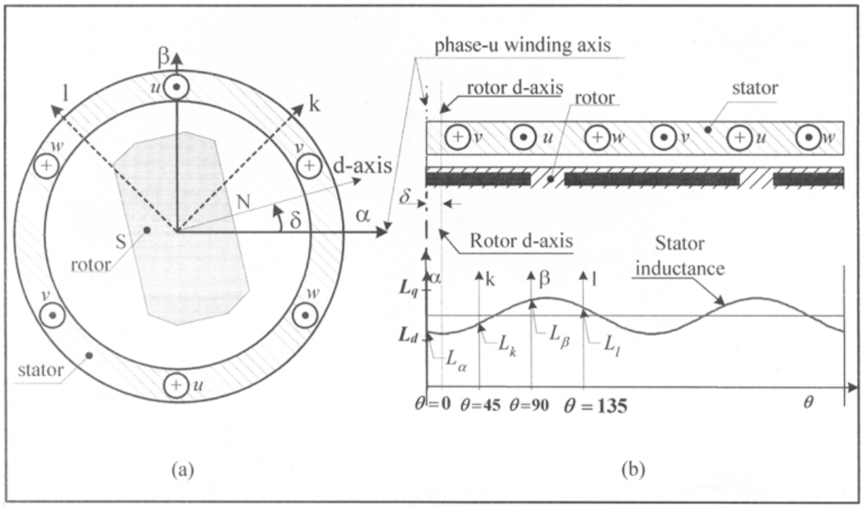

Figure (3.7) (a) Two reference frames $\alpha - \beta$ and $k - l$, where α axis is arbitrarily aligned with phase-u winding axis. (b) Inductance values as the rotor rotates by electrical angle δ from α axis, [15].

$$\begin{aligned} L_\alpha &= L_{sum} - L_{diff}\ cos(2\delta) \\ L_\beta &= L_{sum} + L_{diff}\ cos(2\delta) \\ L_k &= L_{sum} - L_{diff}\ sin(2\delta) \\ L_l &= L_{sum} + L_{diff}\ cos(2\delta) \end{aligned} \tag{3.19}$$

$$\begin{aligned} L_\beta - L_\alpha &= 2L_{diff}\ cos(2\delta) \\ L_l - L_k &= 2L_{diff}\ sin(2\delta) \end{aligned} \tag{3.20}$$

$$\delta = \frac{1}{2}\, tan^{-1}\left(\frac{L_l - L_k}{L_\beta - L_\alpha}\right) \tag{3.21}$$

where L_α, L_k, L_β and L_l are the stator inductance at the α-, β-, k- and l-axes, respectively, as shown in Fig. 3.7(b).

3.5.3 Rotor Position Extraction From Bias-Frequency Signal

The nature of HRreSM requires modulation of the stator current by a triangular waveform of frequency f_b and amplitude of I_f, in order to generate better average rotor flux linkage and power factor. When this modulated stator current passes through the current controller, a reference voltage for the SVPWM will be produced. The phase voltages from the SVPWM inverter contains a bias frequency component. The amplitude of these voltages are functions of the instantaneous reference voltages and can be expressed as shown in equation (3.22).

$$\begin{aligned} u_{bias} &= -\frac{2E}{\pi}\ cos(\frac{\pi u}{2E})\ sin(\omega_b t) \\ v_{bias} &= -\frac{2E}{\pi}\ cos(\frac{\pi v}{2E})\ sin(\omega_b t - \frac{2\pi}{3}) \\ w_{bias} &= -\frac{2E}{\pi}\ cos(\frac{\pi w}{2E})\ sin(\omega_b t - \frac{4\pi}{3}) \end{aligned} \tag{3.22}$$

where E is inverter dc-link voltage; u, v and w are fundamental phase voltages; u_{bias}, v_{bias} and w_{bias} are bias-frequency component voltages in phases u, v and w respectively, ω_b is the bias frequency in rad/sec.

If the motor speed is low, the back emf is also low and the terminal voltage (reference voltage) can be approximated to be zero. Under such approximation, the bias-frequency component voltage amplitudes in the equation (3.22) can be approximated to be constant and given by equation (3.23).

$$\begin{aligned} u_{bias} &= -\frac{2E}{\pi}\ sin(\omega_b t) \\ v_{bias} &= -\frac{2E}{\pi}\ sin(\omega_b t - \frac{2\pi}{3}) \\ w_{bias} &= -\frac{2E}{\pi}\ sin(\omega_b t - \frac{4\pi}{3}) \end{aligned} \tag{3.23}$$

If the 3-phase quantities are transformed to orthogonal two-phase quantities, along the stationary-axis, the HRreSM motor voltage model at the bias frequency can be described by using the equivalent model of HRreSM of equation (3.24) [15], where δ is the angle between the α-axis and the rotor d-axis. In this model, the resistive voltage drop has been ignored since it is very small compared to the inductive reactance at the bias frequency. Since the rotor speed is very small compared to the bias frequency the voltage due to rotor speed has to be neglected. After mathematical manipulation equation (3.25) can be written from equation (3.24) assuming to be constant in one bias-frequency cycle.

$$\begin{bmatrix} u_{bias\_\alpha} \\ u_{bias\_\beta} \end{bmatrix} \begin{bmatrix} L_{sum} + L_{diff}\ cos(2\delta) & L_{diff}\ sin(2\delta) \\ L_{diff}\ sin(2\delta) & L_{sum} - L_{diff}\ cos(2\delta) \end{bmatrix} \frac{d}{dt} \begin{bmatrix} i_{bias\_\alpha} \\ i_{bias\_\beta} \end{bmatrix} \tag{3.24}$$

$$\begin{bmatrix} i_{bias\_\alpha} \\ i_{bias\_\beta} \end{bmatrix} \begin{bmatrix} L_{sum} - L_{diff}\, cos(2\delta) & -L_{diff}\, sin(2\delta) \\ -L_{diff}\, sin(2\delta) & L_{sum} + L_{diff}\, cos(2\delta) \end{bmatrix} \begin{bmatrix} \int u_{bias\_\alpha}\, dt \\ \int u_{bias\_\beta}\, dt \end{bmatrix} \tag{3.25}$$

If the saliency, $L_q/L_d < 3$, and $\int (u_{bias\_i})dt$ and $\int (u_{bias\_j})dt$ are sinusoidal and orthogonal. This is an approximation with the reference voltage being very small compared to the dc-link voltage. Equation (3.26) can be written from equation (3.25).

$$\left[\int_0^{T_b} |i_{bias\_\alpha}|\, dt\right] - \int_0^{T_b} |i_{bias\_\beta}|\, dt = k\, L_{diff}\, cos(2\delta) \tag{3.26}$$

$$\int_0^{T_b} |i_{bias\_k}|\, dt - \int_0^{T_b} |i_{bias\_l}|\, dt = k\, L_{diff}\, sin(2\delta) \tag{3.27}$$

where $k \propto \left(\int_0^{T_{bf}} \left[\int u_{bias\_x} dt\right]\, dt / L_{sum}^2 - L_{diff}^2\right), x = \alpha, \beta, k, l.$

Similarly, equation (3.27) can be obtained from the voltage equation on the reference frame.

Equations (3.26) and (3.27) are similar to equations at (3.20). Their relation can be described by the following equation, equation (3.28).

$$\begin{aligned} (L_\beta - L_\alpha) &\propto \left(\int_0^{T_b} |i_{bias\_\beta}|\, dt - \int_0^{T_b} |i_{bias\_\alpha}|\, dt\right) \\ (L_l - L_k) &\propto \left(\int_0^{T_b} |i_{bias\_l}|\, dt - \int_0^{T_b} |i_{bias\_k}|\, dt\right) \end{aligned} \tag{3.28}$$

Hence, a rotor position equation similar to equation (3.21) can be written from the bias-frequency currents at the four axes as equation (3.29)

$$\delta = \frac{1}{2} arctan \left(\frac{\int_0^{T_b} |i_{bias\_k}|\, dt - \int_0^{T_b} |i_{bias\_l}|\, dt}{\int_0^{T_b} |i_{bias\_\alpha}|\, dt - \int_0^{T_b} |i_{bias\_\beta}|\, dt} \right) \tag{3.29}$$

Note that no motor parameter is used in equation (3.29). Hence, knowledge of motor parameters is not required. Furthermore, the integration of the bias-frequency component current can be replaced by a moving average of the absolute value of the bias-frequency component current with a little more than two samples in one bias frequency cycle. This avoids the need for the integration constant [15].

Chapter 4

Drive System and Controller Design

4.1 Introduction

In this chapter, the overall simulation environment, motor parameter selection, the simplorer model of the inverter and the design of used controllers are discussed.

This research study uses simulation modeling for the demonstration of the effectiveness of the candidate control model for this particular motor. Since the application area of the drive system is necessary, EV is selected and proposed. For EV application before selecting the electric motor for propolsion, it is crusial to know the required ratings of the motor for the particular EV. So motor rating calculation based on the vehicle dynamics has performed before simulation model developed. Then based on the calculated motor ratings and using the selected motor's parameters, the motor dynamics is modeled on the MATLAB/ Simscape, refer [12] for the MATLAB code.

The main components of EVs are the electric motor, the inverter, and the controller. So in this paper, a realistic modeling of each of these components is performed. i.e. The motor modeling on MATLAB/ Simscape, Controller modeling on MATLAB/ Simulink and inverter (VSI) modeling on ANSYS Electronics/ Simplorer. The interfacing of two different simulation softwares, MATLAB/ Simulink to Simplorer, is discussed on the second section of this chapter under the overall simulation environment development section. The components of the power electronic circuit of an inverter, a realistic VSI model, used in our model are described under the fourth section of this chapter.

The design of speed PI controller and current PI controllers of the FOC of the HReSM are discussed on the final section of this chapter.

4.2 Overall Simulation Environment Development

MTPA based sensorless speed controller design for the halfwave rectified rotor excited synchronous motor is proposed to be modelled and simulated based on the general block diagram shown below on figure 4.1.

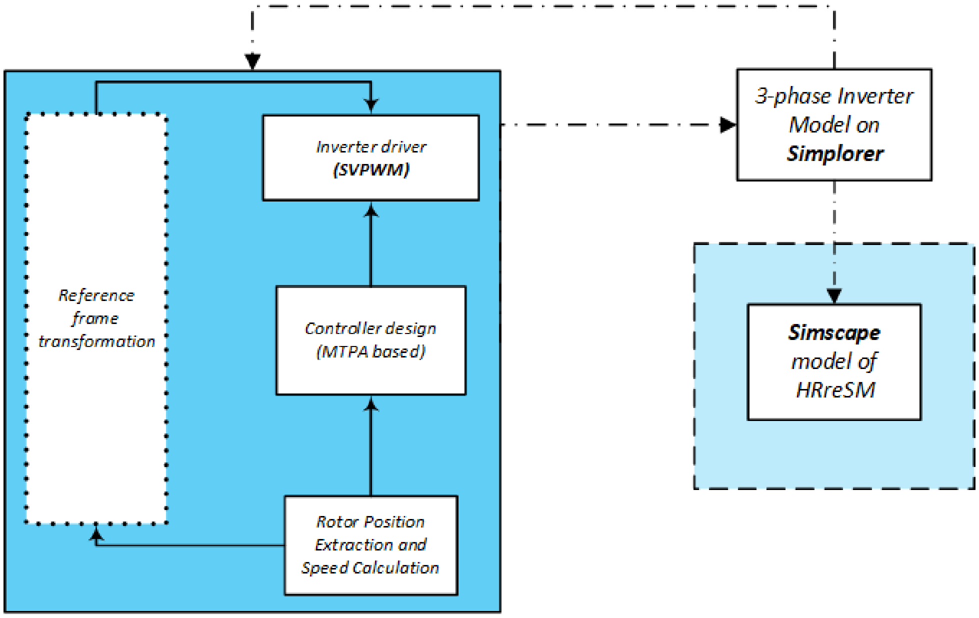

Figure (4.1) Overall Simulation Environment for the MTPA based sensorless control of HRreSM.

The block labeled by "Simscape model of HRreSM" represents a halfwave rectified rotor excited synchronous motor which modeled on Simscape, in which the MTPA and FW based speed control is be applied. The motor is to be adapted for an automobile traction application, assuming the EV (automobile) moving on a given flat surface.

The " 3-phase inverter model on Simplorer" block is responsible for generation of a controlled three phase voltage, which is a supply to the stator winding of HRreSM. It is modeled on SIMPLORER and simulated together with MATLAB, Simulink . The control signal to control switching of the semiconductor switches of the 3-phase inverter is generated by using an appropriate PWM technique, SVPWM, which has been represented by the "inverter driver (SVPWM)" block on figure 4.1.

To simplify the analysis during the modeling, the phase variables and motor parameters has to be referred to some reference frame and this paper considers referring the phase variables as well as the motor parameters to the rotor reference frame. Conversely to retain the original variable an inverse reference frame transform is applied. This transformation is represented on the given general block diagram as "reference frame transformation".

The MTPA, the maximum torque per ampere control strategy and Flux Weakening control, with in the field-oriented controller (FOC) is modeled with in the "controller design (MTPA based)" block of the block diagram. It is known that in the MTPA strategy, the two-axis stator reference currents are calculated so that the maximum torque per ampere will be achieved. And the flux weakening control is for the operation of the motor in high speed.

To simulate this system based on the above general block diagram, it is proposed to use three simulation softwares.

1. Mainly MATLAB simulation software (Simulink and Simscape): To design the field-oriented controller and to write different scripts, which are necessary for the accomplishment of the objective of this research is used. The block containing "inverter driver (SVPWM)", "controller design (MTPA based)", "Simscape model of HReSM" and "reference frame transformation" blocks are modelled and simulated on MATLAB Simulink.
2. And Simplorer of ANSYS electronics is proposed to design the inverter (3-phase VSI inverter). i.e. "3-phase inverter model on Simplorer" block on figure 4.1.

These models on each softwares are going to be integrated (interfaced) to get the results of the whole proposed system. The interfacing and the indirect connections are tried to be indicated by using center lines on the block diagram, figure 4.1.

4.2.1 Interfacing Simulink to Simplorer (Sim2Sim) Link

The following steps are found accurate to develop the interfacing between Simulink and simplorer.

1. You need have an administrator rights!
2. You need a compiler running in MATLAB. Check it by typeing mex –setup on the command. If you don't have one already, install it from MATLAB Add-Ons tab on the toolbar.
3. Set the MATLAB path in Simplorer, using the following directory: Tools− >Options− > General Options− >Miscellaneous Options− >MATLAB Optimization set the MATLAB path.
4. Set the Ansys Path in MATLAB, using the following directory: In Environment− >Set Path− >Add C:\Program Files\AnsysEM\AnsysEM16.2\Win64\cpl\matlab\r2014. .
5. In MATLAB create your model with an s-function call it "AnsoftSFunction", now you get the dialog from the manual. The dialog box Look like figure B.3 with all field empty.
6. In the link assignment area add as many Inputs and Outputs you need (using the little button with the yellow flash). Select One SIMULINK-IN and one SIMPLORER-OUT then press link.

7. Press OK and s-function with as many inputs and outputs that you selected will be created. Run your Simulink model and save as *.mdl

8. Now go to Simplorer and create Simulink Subcircuit, use the following step: Simplorer Circuit $->$ Subcircuit $->$ Add Simulink Component. By checking on the ”Read link information from the file” option, Connect to the Simulink model you just created using the little button with three dots and Wait until all inputs and outputs are loaded. Select the Pin option for each inputs and outputs then press ”OK”.

9. Design your Simplorer circuit including the ”Simulink Component” and save it. Then switch back to Simulink and double click on the s-function block. Select link information from file and Select the Simplorer file you just created, Then press ”OK”.

4.3 Inverter Modeling on Simplorer

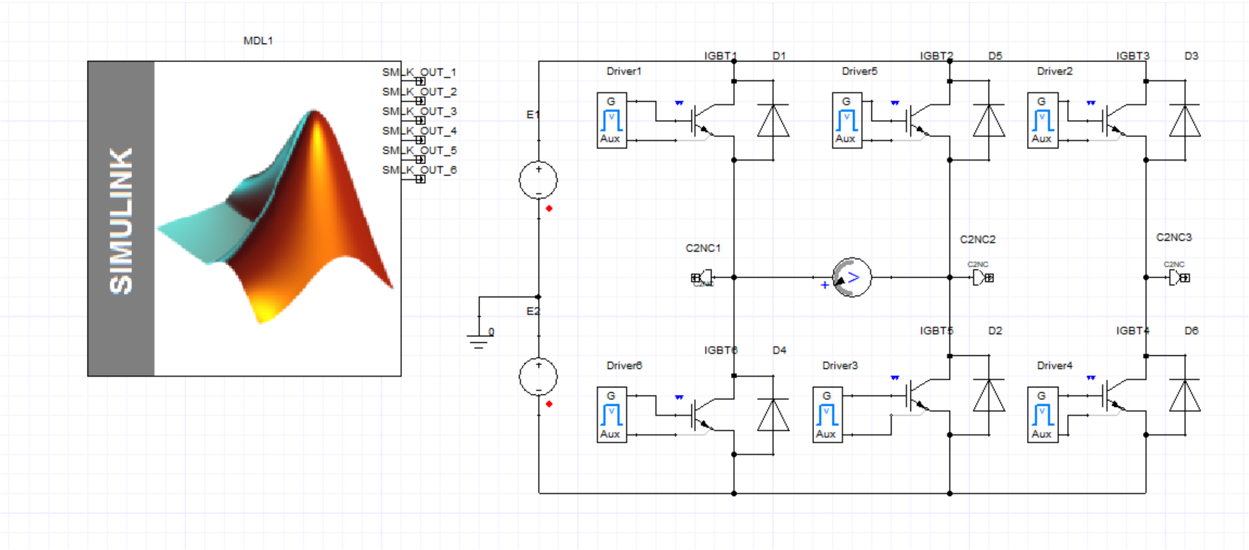

Figure (4.2) Three-phase Voltage Source Inverter model on Simplorer

The power electronic circuit shown in the figure 4.2 is the model of realistic three-phase voltage source inverter (VSI) designed and modeled on Simplorer. The gate control signal, the control signals controlling the switching of the semiconductor switches (IGBTs) on the inverter, are generated on simulink using SVPWM technique. The inverter output voltage waveforms, the phase and line voltages, also transferred back to the Simulink inorder to be supplied to the motor and for further control. The signal communication is through the SIM2SIM Link, for further understanding look section 4.2.1.

4.3.1 IGBT and Power Diode Selection on Simplorer

The selected semiconductor switching devices, IGBTs and power diodes, used for the modeling of VSI on Simplorer are ”$5SNA0800N330100 : ABB - Si - IGBTs\_Basic\_Dyn$” and ”$IDP18E120$:

$Infineon - Si - Diodes$" respectively. This devices are real and they exist on the market. The aim of realistic modeling of this VSI is in order to design and model an inverter which could be used for implementation purposes on the ground.

The selected IGBT has voltage and current rating of $1800V$ (V_{CE}) and $800A$ (I_{CE}). Among the existing semiconductor switching devices (for instance, BJT and MOSFET), the reason IGBT is selected is, it is developed by combining into it the best qualities of both BJT and MOSFET. Thus an IGBT possesses the high input impedance quality of a power MOSFET and has low on-state power loss as in a BJT. Further IGBT is free from the drawback of BJT, second breakdown problem. Besides IGBTs are widely used in medium power applications. Even if IGBTs are more expensive than BJTs, they are popular because of lower gate-drive requirements, lower switching losses and smaller snubber circuit requirements. And IGBT converters are more efficient with less size as well as cost, as compared to BJT converters. An inverter of IGBTs is capable of working with 15-20 KHz switching frequency with objectionable audio-noise. Even if MOSFETs are more advantagious in many cases than IGBTs, IGBT's ratings which is above (1200 V, 500 A) are better for medium power applications [42].

Among the existing IGBTs on the Simplorer library, the selected IGBT is better in the nominal value of voltage and current (V_{CE} and I_{CE}), i.e. $1800V$ and $800A$. And the selected diode among the existing diodes on the Simplorer library is better in the diode's reverse recovery time characteristics, which is the major parameter in the design of signal diodes as well as power diodes [42]. The selected power diode has a very small reverse recovery time (t_{rr}), i.e. $t_{rr} = 2e^{-16}s$, Which makes it under the category of the fast-recovery diodes. Any interested reader of this paper can refer the specification sheets of this devices from the manufacturers website or by searching on web using the device's name.

4.4 Motor Parameter Selection

The basis for all the simulations is an 8-pole, 50 Hz 3-phase HRreSM with the rated power of $71.6\ kW$, rated torque of $60\ Nm$ and from this two ratings the base speed of $1193\ rad/sec$ is used for performance analysis of the proposed MTPA and FW control based drive system. The simulation model is developed in MATLAB/Simulink and Simplorer environments. And the simulation parameters for the HRreSM are shown in the following table (table 4.1).

Table (4.1) Electrical and Mechanical Parameter of The Motor

Parameter	unit	Value
Stator Resistance (R_a)	Ω	0.01
d-axis self-inductance (L_d)	H	0.0015
q-axis self-inductance (L_q)	H	0.0007
No. of pole pair (p)	$-$	4
Inertia (J)	Kg/m^2	0.01
Field Winding Resistance (R_{fd})	Ω	0.005
Field winding self-inductance (L_{fd})	H	0.00085
Mutual inductance (M_{fd})	H	0.0008

4.5 Controller Design

The proposed HRreSM drive system uses field oriented control (FOC) strategy to control the speed and torque of the motor. In Figure 1.1, the block diagram representation of the whole controlled drive system is provided. There are two control loops in the general structure of the FOC. The first one is the outer loop called speed control loop with PI controller to compensate the motor speed error. The second loop is the inner loop, which is to control the d-q axes currents. The inner loop contains two PI compensators, one for the control of the d-axis current (field winding flux producing component) while the other is for the q-axis current (torque producing component). In this section the design of these PI controllers will be discussed.

4.5.1 Speed Control Loop

The rotational speed of the motor can be regulated by the speed controller block of figure 1.1. The loop consists of the proportional integral (PI) speed controller block, MTPA and FW control block, current controllers (PI), SVPWM inverter, motor plus load and transformation blocks (parks and inverse park transform) based on figure 1.1. The shaded rectangle in 4.3, consists of a current controller block, holding the inner loop, MTPA and FW control. The motor speed ω_m is the output of the inner loop. And Apply Load torque as a disturbance. Then using PI control law and pole placement method ,for the calculation of the PI controller parameters, the speed controller computes the reference torque, T_{ref}. [12].

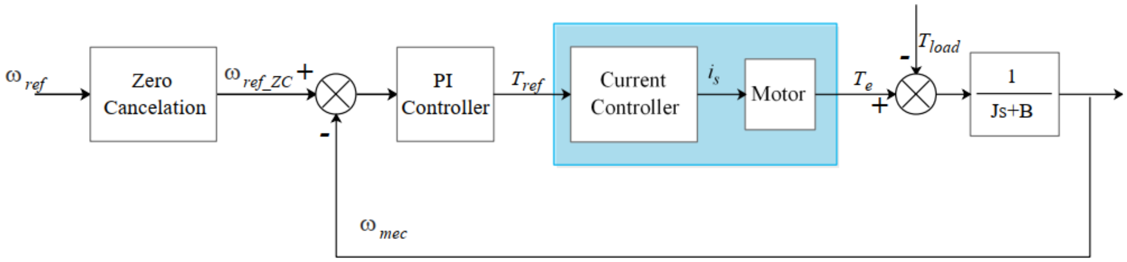

Figure (4.3) Block Diagram Representation of The Speed Control Loop, [12].

Figure 4.3 shows the closed loop system general block representation, where the mechanical load is modeled as a first order. Equation (4.1) shows the transfer function of the PI controller and the mechanical load[43].

$$\begin{aligned} G_M(S) &= \frac{1}{J_r s + B_r} \\ G_{PI}(S) &= \frac{K_P s + K_I}{s} \end{aligned} \tag{4.1}$$

where B_r and J_r are the motor's rotational friction coefficient and motor's rotational inertia respectively. Between the sampling instants of the speed control loop, the response of the current loop will reach steady state. This is due to the application of much faster sampling frequency for the current control loop than the speed control loop. Therefore, a unity gain can be considered for the transfer function from T_{ref} to T_e, from the perspective of the outer loop. ω_{ZC-ref} to ω_{ref} transfer function for the closed loop can be described as,

$$G_{OL}(s) = \frac{\left(\frac{K_P}{K_I}s + 1\right)\frac{K_I}{J_r}}{s^2 + \left(\frac{B_r + K_P}{J_r}\right)s + \frac{K_I}{J_r}} \tag{4.2}$$

$$= \frac{\omega_m(s)}{\omega_{ref}(s)} = \frac{G_{PI}(s)G_M(s)}{G_{PI}(s)G_M(s) + 1} \tag{4.3}$$

A zero is introduced in the closed loop transfer function by the PI controller, as shown in equation (4.3). An increase in system overshoot, which lowers the bandwidth of the closed loop, happens due to this derivative behavior of the loop. In order to avoid this effect, adding a zero block in the feed forward path will compensate the zero of the PI controller. The transfer function of the zero block can be written as

$$G_{ZC}(s) = \frac{1}{\frac{K_P}{K_I}s + 1} \tag{4.4}$$

The feed forward path with zero cancellation gives the following transfer function of the speed loop.

$$\begin{aligned} G_{OL}(s) &= \frac{\frac{K_I}{J_r}}{s^2 + \left(\frac{K_P+B_r}{J_r}\right)s + \frac{K_I}{J_r}} \\ &= G_{ZC}(s)\frac{G_{PI}(s)G_M(s)}{1+G_{PI}(s)G_M(s)} \end{aligned} \tag{4.5}$$

Now let's rewrite the equation (4.5) using the general 2^{nd}-order system [43].

$$G_{OL}(s) = \frac{\omega_n^2}{s^2 + 2\xi\omega_n s + \omega_n^2} \tag{4.6}$$

Where ξ and ω_n are the damping ratio and the natural frequency of the transfer function of the closed-loop system . Based on the transient performance requirement, first choose the ξ and ω_n value and then use the following equation to calculate the parametersof the PI controller.

$$K_P = -B_r + 2J_r\xi\omega_n \tag{4.7a}$$

$$K_I = J_r\omega_n^2 \tag{4.7b}$$

Let's see an example based on the following table, table 4.2, showing motor's mechanical parameters and required closed-loop performance measurements in order to calculate the controller gains parameters.

Table (4.2) Outer loop PI controller Designed Parameters

Paramter	**Value**
Damping Ratio, ξ	2
Natural Frequency, ω_n (rad/s)	60
Rotational Friction, B_r (Nms)	0.1
Rotor Inertia, J_r (kgm^2)	0.01

To provide faster cloased-loop step response a much higher ω_n has been selected and the over-damped closed loop system ($\xi > 1$ i.e., $\xi = 2$) is selected to reduce the oscillation,look at table 4.2. Using Equation (4.7) the controller gains $K_P = 2.4$ and $K_I = 36$ can be obtained by calculation.

In this thesis, a trial and error procedure has been followed to select the speed controller PI gains. And then based on equation (4.7) and motor's mechanical parameters (i.e., $J_r = 0.01$ kgm^2 and $B_r = 0.1$ Nms) the natural frequency and damping ratio constants are calculated. As such for the speed PI controller, $K_P = 10$, $K_I = 55$ has been selected. Then $\omega_n = 74.16$ rad/s and $\xi = 6.81$ values are obtained.

4.5.2 Current Control Loop

This control loop consists of the reference d-q-axes currents from MTPA and FW controls, d-axis current modulation (for this particular motor) and current controllers.

As described earlier, superimposing a triangular waveform $A_f(t)$ of amplitude I_f with the d-axis current component is crucial during the modeling and control of HReSM. After the modulation of the stator current, the field winding flux becomes proportional to amplitude, I_f, of the triangular signal. For speeds upto ω_{base}, I_f is provided from the MTPA control block, i.e. $i_{d\ ref}$. In the high speed operation region, $\omega_{mech} > \omega_{base}$, FW control techniques are used to determine the amplitude, I_f.

As discussed in the sections 3.2 and 3.3 the reference values for the current PI controllers are from MTPA and FW control algorithms, Look at equation (3.4), (3.12) and (3.17).

Current Regulator

Using the corresponding dq-axes current references, the current regulator (PI) generates voltage reference in the dq-axes reference frame. For each axis, the motor and the load with the voltage source are modeled as first order, during the design of the current controller. [12].

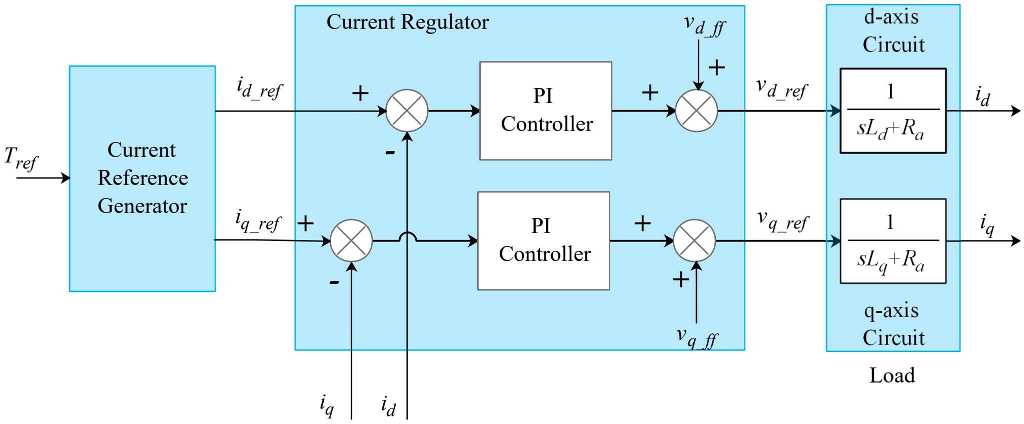

Figure (4.4) Block Diagram Represention of Current controller loop, [12].

To regulate the current to the reference dq-axes current values, two PI controllers are required. As shown in Equation (2.1), a voltage term from the speed voltaage ($\omega_e\lambda_d$ for the q-axis circuit and $-\omega_e\lambda_q$ for the d-axis circuit) with in the R-L circuit is used to model the individual circuits in each reference frame axis. The feedback current control process faces negative influence due to the existence of these voltage components in the loop. Using feed-forward long with feedback control improves the performance of the current control and elliminates the effects of the disturbance components, look at figure 4.4. The dq-axes currents cross decoupling is represented by these feed-forward terms.

$$v_{ff\_d} = -\omega_e \psi_q \tag{4.8a}$$

$$v_{ff\_q} = \omega_e \psi_d \tag{4.8b}$$

To design the PI controller, use the same pole placement method which has been used in the design of the PI controller in the speed control loop. For the R-L load and PI controller, the following expression of transfer function are being used during the design of current controller [12].

$$G_{RL\ j} = \frac{1}{R_a + sL_j} \tag{4.9a}$$

$$G_{PI\ j} = \frac{K_{I\ j} + sK_{P\ j}}{s} \tag{4.9b}$$

Where $j = d,\ q$, for the d- and q- axes circuits, respectively.
Then equation (4.10) describes the closed-loop transfer function for this inner control loop.

$$\begin{aligned} G_{IL\ j}(s) &= \frac{\frac{K_{I\ j}}{L_j}\left(\frac{K_{P\ j}}{K_{I\ j}}s + 1\right)}{s^2 + \left(\frac{K_{P\ j}+R_a}{L_j}\right)s + \frac{K_{I\ j}}{L;j}} \\ &= \frac{i_j(s)}{i_{j\ ref}(s)} = \frac{G_{PI\ j}(s)G_{RL\ j}(s)}{1 + G_{PI\ j}(s)G_{RL\ j}(s)} \end{aligned} \tag{4.10}$$

A zero-cancellation block with transfer function of equation (4.11) is introduced in the feed-forward path to compensate the zeros added by the PI controller.

$$G_{ZC\ j}(s) = \frac{1}{\frac{K_{P\ j}}{K_{I\ j}}s + 1} \tag{4.11}$$

And the complete closed-loop transfer function is given by

$$\begin{aligned} G_{IL\ j}(s) &= \frac{\frac{K_{I\ j}}{L;j}}{s^2 + \left(\frac{K_{P\ j}+R_a}{L_j}\right)s + \frac{K_{I\ j}}{L_j}} \\ &= G_{ZC\ j}(s)\frac{G_{PI\ j}(s)G_{RL\ j}(s)}{1 + G_{PI\ j}(s)G_{RL\ j}(s)} \end{aligned} \tag{4.12}$$

Using the general form of a second order system in Equation (4.6) to compare with equation (4.12), the following expressions of PI controller gains can be obtained.

$$K_{P\,j} = -R_a + 2\xi\omega_n L_j \tag{4.13a}$$

$$K_{I\,j} = \omega_n^2 L_j \tag{4.13b}$$

In this thesis, a trial and error procedure is used to select the current PI controllers' gain values. Therefore, $K_P = 50$, $K_I = 10$ for the q-axis current loop and $K_P = 10$, $K_I = 50$ for the d-axis current have been selected. Then for the q-axis $\xi = 298.86$, $\omega_n = 119.5\ rad/s$ and for the d-axis $\omega_n = 182.57\ rad/s$, $\xi = 18.28$ are obtained

Chapter 5

Simulation Results and Discussion

Simulation results of the complete model, MTPA based sensorless FOC of HRreSM, along with the discussion are presented in this chapter. First the performance of VSI model on Simplorer is provided together with the performance of SVPWM gate signal generator on MATLAB/ Simulink, then the performance of the rotor position information extraction model is realized. After that the MTPA and FW control models' performances are discussed. Finally the general speed and torque performances of the complete FOC model are illustrated. The complete sensorless drive system control model is based on the block diagram shown in the figure 5.1. The model has been simulated on MATLAB/ Simulink and Simplorer simulation softwares.

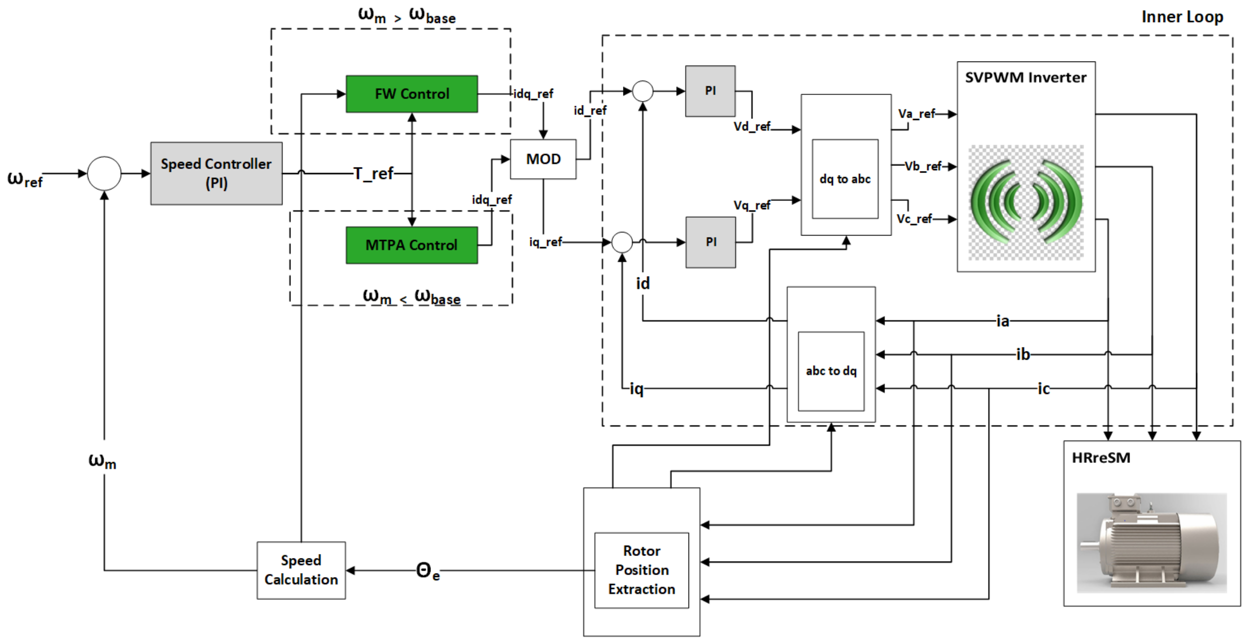

Figure (5.1) General block diagram of the MTPA based sensorless control of HRreSM

The model has been prepared for simulation as follows. Speed PI controller of figure 5.1 gets the reference speed signal from a signal builder block of MATLAB/ Simulink and the speed controller gets the feedback motor speed from the outputs of Simscape motor model (sensored) or from the speed calculation model based on the extracted rotor position (sensorless). The speed controller output, Torque Reference, is used as an input for MTPA and FW control models in order to generate optimal d-q axes reference current values. And the obtained optimal d-q axis current values are going to be used as an input for the current PI controllers. For this particular motor, HRreSM, stator current modulation using a triangular wave signal is necessary, and which is modeled before the current controllers (i.e. superimposing the reference d-axis current from MTPA or FW with a triangular waveform of frequency f_b and amplitude of I_f). The outputs of the inner loop controller (current PI controllers) are reference dq-axes voltages, which are necessary for SVPWM gate control signal production and the six gate control signals from the SVPWM model are fed to the 3-phase VSI model on Simplorer. The motor on MATLAB/ Simscape is supplied by the three phase voltages, which are the outputs of the Simplorer VSI model. The signal communication between these two softwares, MATLAB/ Simulink and Simplorer, is through the SIM2SIM link interface.

5.1 Performance of The Realistic VSI Model

In this subsection, the performance of SVPWM gate signal generation on Simulink and the VSI model performance comparison between a realistic model on Simplorer and an ideal model on Simulink will be discussed relying on their results. First the SVPWM gate signal performances will be discussed and then using the same gate signals from the SVPWM and the same lowpass filters, to filter the higher harmonics components of the VSI models, the performances of the VSI models, for the realistic and the ideal, will be discussed.

5.1.1 Performance of SVPWM Gate Signal Generator

Here first the performance of SVPWM gate control signal generator on Simulink is presented. Then the comparison between the SVPWM VSI model and the SPWM VSI model is presented. The realization of SVPWM is shown in appendix B.3. The MATLAB function block shown in the figure B.4 performs the required six sector operations. Refer [12] for the MATLAB code inside the MATLAB function.

For the reference voltage vector in the third sector, i.e. its space vector $V_a + V_b + V_c$ has an angle between $2\pi/3$ and π, the switching sequence which is shown in figure 5.2 is obtained.

All switching sequences shown in the figure 5.2 are generated from the SVPWM generator for the six sectors and this repeats all over again. This process continues endlessly and ensures the availability of the required phase voltages to the motor, HRreSM. The required voltages that are obtained from PI controllers (from the inner control loop) are represented by these switching signals. A VSI, realistic model on Simplorer, then converts this series of digital signals to a 3-phase voltage signal shown in figure 5.3a. Since the inductance

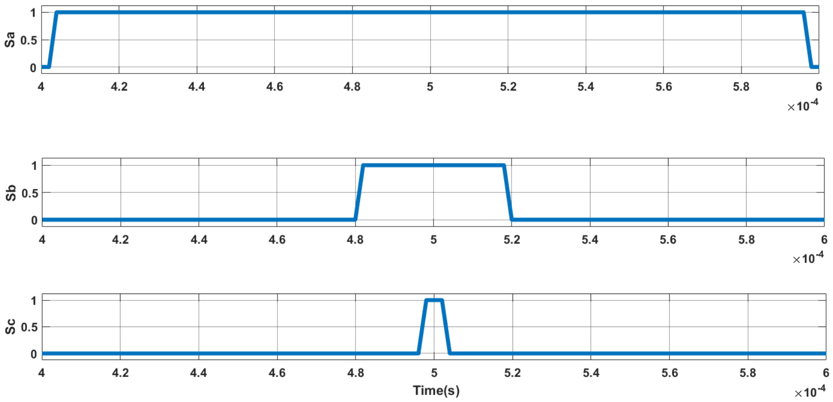

Figure (5.2) Switching Sequence Output of the SVPWM Generator in the third Sector.

of stator winding of the motor acts as a low pass filter, the filtered signal will take the form shown in figure 5.3b. Figure 5.3 summarizes the VSI phase and line voltage waveforms.

The registered peak value of the phase and line voltage of the realistic VSI model on Simplorer, as shown in figure 5.3b and 5.3d respectively, is 222 V and 390 V. The VSI outputs should pass through a lowpass filter in order to give the filtered phase and line voltage waveforms of figure 5.3b and 5.3d. Refer figure D.2 of appendix D for the employed lowpass filter. The purpose of using the lowpass filter is to get rid of the unnecessary harmonics and to get a sinusoidal signal with fundamental frequency of 50 Hz.

The α-β transformation of the phase voltage signals is shown in the figure 5.4. The 90 degree phase shift between the α and β components is clearly seen on the figure 5.4c. The complex plane (α-β) plot in figure 5.5 shows the hexagon incorporating the six sectors. The inscribed circle is the α-β plot of the filtered signal. The radius of this circle represents the amplitude of the reference three phase voltage ($|V_s^*| = \frac{V_{dc}}{\sqrt{3}}$). Whenever the reference voltage's amplitude is less than or equal to this value the SVPWM generator works in the linear modulation region. In the other modulation regions (over modulation regions) the concept of SVPWM degrades slowly as the amplitude value is increased.

Comparison of SVPWM and SPWM Techniques

In order to study the harmonics and the spectrum of SVPWM technique, a three-phase SPWM (Three triangular waveforms, with $\frac{2\pi}{3} rad$ phase shift and frequency of 5kHz, are compared to the three-phase sinusoidal reference signals) is implemented as shown in appendix E [15]. The results of the FFT analysis of the SVPWM and SPWM techniques are shown in figure 5.6 and figure 5.7 respectively. In the figures the waveform for one of the phases, Vcn, and the corresponding FFT spectrum with THD value is shown.

The results shown in the figures 5.6 and 5.7, consist of the phase voltage signal V_{cn} and the frequency

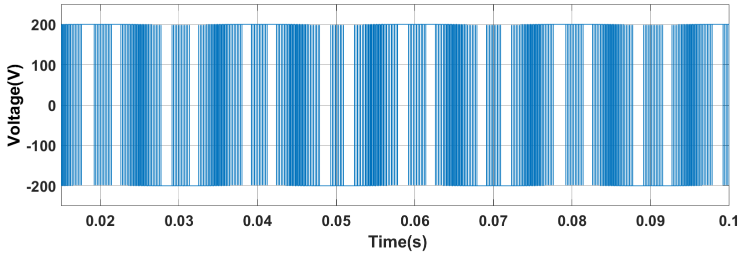

(a) VSI Phase Voltage, Unfiltered

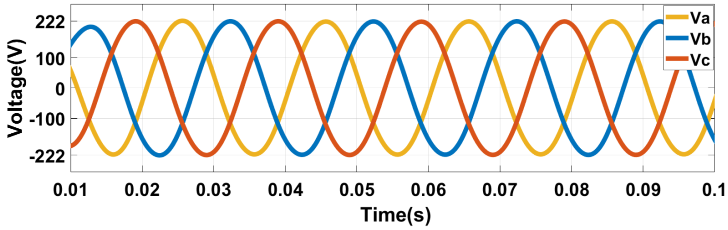

(b) VSI Phase Voltage, Filtered

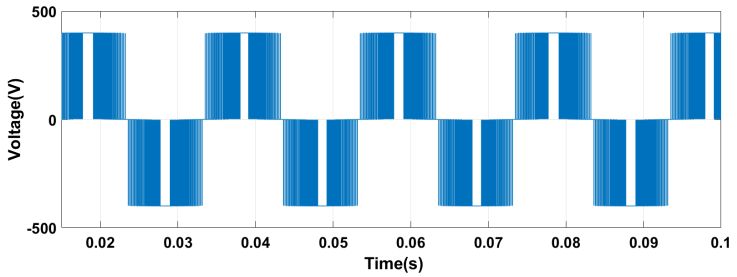

(c) VSI Line Voltage, Unfiltered

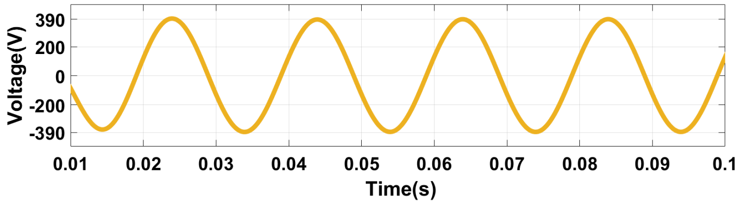

(d) VSI Line Voltage, Filtered

Figure (5.3) VSI Phase and Line Voltages, Filtered and Unfiltered

spectrum. From the frequency spectrum of both figures, it can be clearly seen that, only the spectrum of the fundamental and switching components have contribution on the signal. As a result, the THD of the SVPWM is less than that of the SPWM. There is about 33.1077% of THD difference. Even the peak value of the waveform in figure 5.6 is 226.5 and in figure 5.7 is 200, which implies that, the conversion ratio from DC to AC is larger in SVPWM than SPWM.

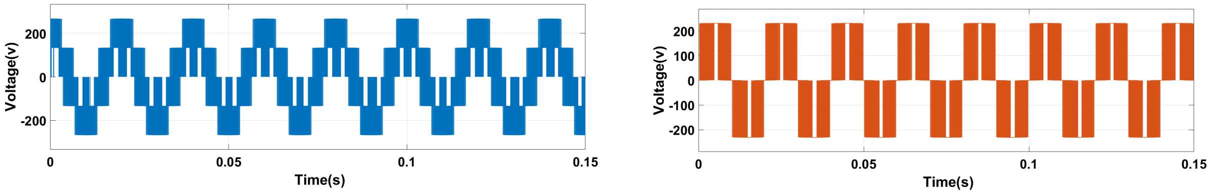

(a) Alpha component

(b) Beta component

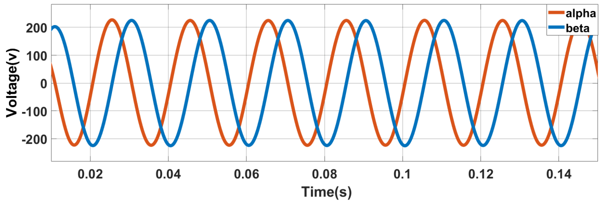

(c) Filtered alpha and beta components

Figure (5.4) Alpha-Beta components of phase voltage, Filtered and Unfiltered.

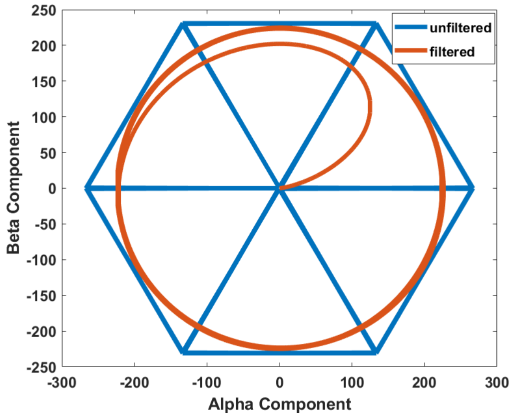

Figure (5.5) Complex plot of Filtered and Unfiltered Alpha-Beta Component.

The lower THD in SVPWM implies lower switching loses than SPWM [16]. This lower THD value secures the reliability and flexibility of SVPWM.

Apart from motor drives, this PWM technique can be used in different modern non-linear systems, where the presence of harmonics is inevitable and the THD should be in the limit standard expressed by [20]. In these FFT analyses, the maximum frequency for THD computation is ”Same as max. frequency” .

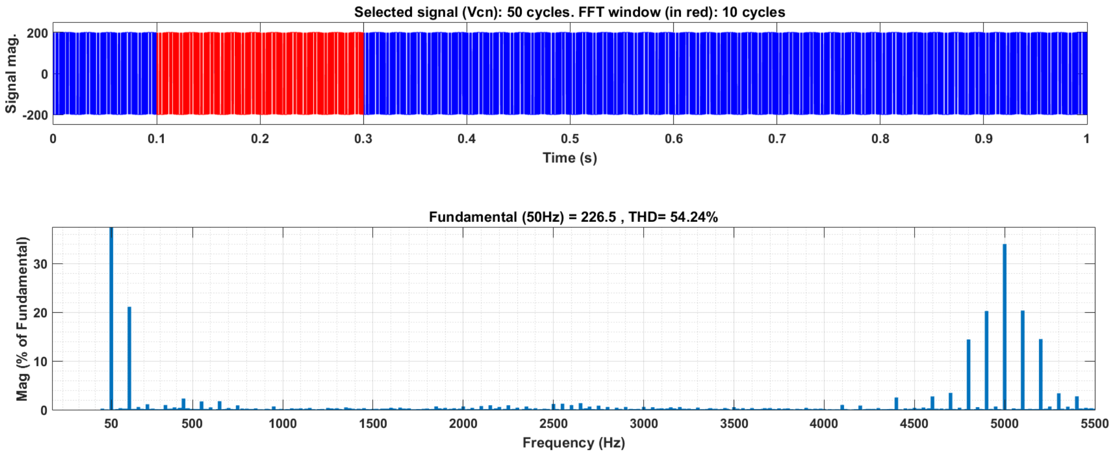

Figure (5.6) Waveform and Frequency Spectrum of Phase Voltage, V_{cn}, of SVPWM.

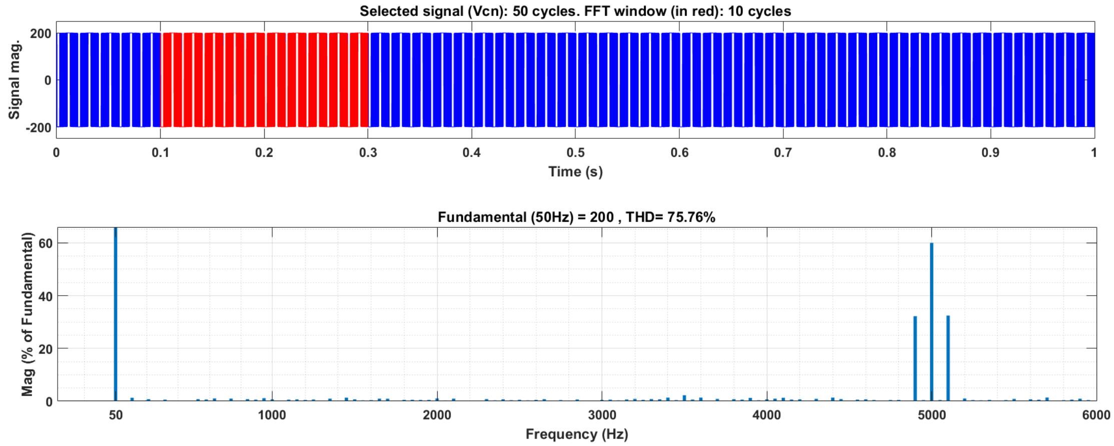

Figure (5.7) Waveform and Frequency Spectrum of Phase Voltage, V_{cn}, of SPWM.

5.1.2 Comparison of a Realistic and Ideal Model of SVPWM Voltage Source Inverter

In order to understand the performance of the realistic VSI model of Simplorer, it is mandatory to make a comparison with the simulink ideal VSI model. Using the same gate control signals and lowpass filters, let's compare the VSI outputs, phase voltages and line voltages, of these two models including the FFT analysis.

The phase and line voltages in figure 5.8 are the outputs of the ideal VSI model on Simulink. The peak value of the phase voltage is 224 V and the peak value of the line voltage is 394V. Figure 5.3 contains the phase and line voltages of the realistic VSI model.

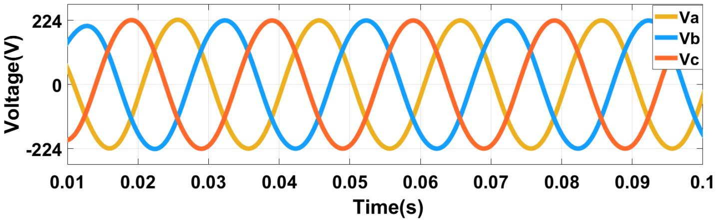

(a) VSI Phase Voltage

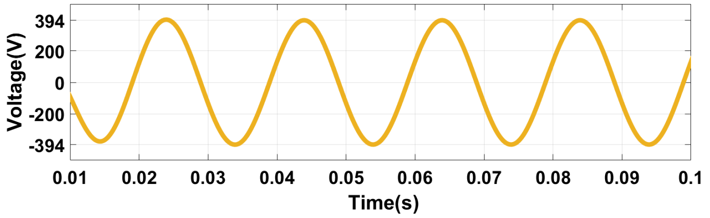

(b) VSI Line Voltage

Figure (5.8) VSI Phase and Line Voltages of An Ideal Simulink Model

The percentage difference between the peak value of the phase voltages of the realistic VSI model and the peak value of the phase voltages of the ideal VSI model is 0.897%. And The percentage difference between the peak value of the line voltages of the realistic VSI model and the peak value of the line voltages of the ideal VSI model is 1.02%. From the FFT analysis of figure 5.9, there is about 2.108% of THD difference between these models. Even the peak value of the waveform in figure 5.6 is 226.5 and in figure 5.9 is 229.9, which means there is 1.49% difference in the peak values of the phase voltages of the two models.

As described above, the peak values of the phase and line voltages of the realistic VSI model are a little less than the ideal VSI model. There are few possible reasons for that, the first reason is the effect of real time parameters used for the design of power IGBT and power diodes of the realistic model, i.e. their realistic nature. And the second and the last possible reason is the effect of the interfacing link (SIM2SIM) between the two softwares, which depends on the performance of the computer used for simulation. But, since the percentage difference of the outputs of the two models is minor, it is obvious that the designed realistic model using real-time semiconductor devices and the performance of the computer used for simulation, are excellent. So, The advantages of using those two softwares for their purpose is much better than the effects on the outputs of the model.

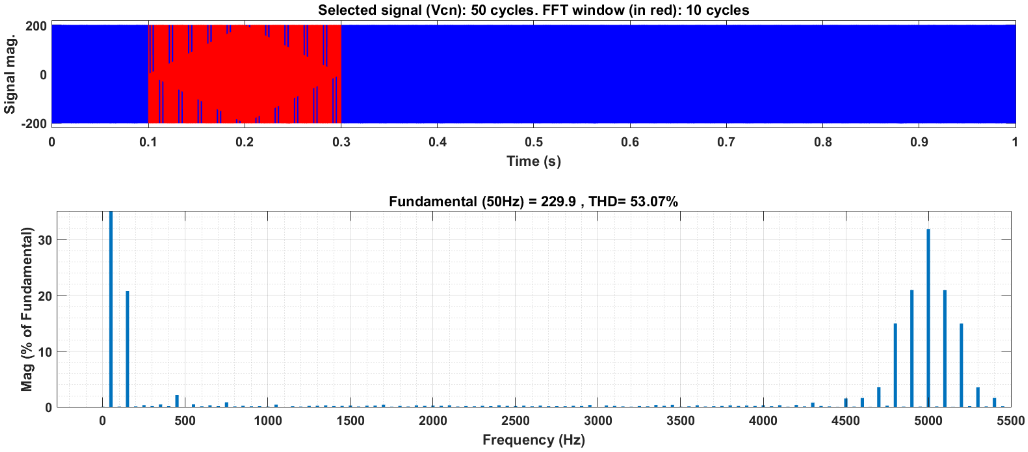

Figure (5.9) Waveform and Frequency Spectrum of Phase Voltage, V_{cn}, of the ideal SVPWM inverter.

5.2 Performance of The Rotor Position Information Extraction

Unloaded drive ($0 - 2000\,rpm$), loaded drive model with $T_L = 5Nm$ ($0 - 2000\,rpm$) and a loaded drive for a reverse speed operation ($-6000\,rpm - 6000\,rpm$) are used during the modeling of the rotor position estimation. The model supplies the HRreSM by a modulated stator current, where the frequency (bias frequency) of the modulating signal (triangular waveform) is 1.5kHz. This bias frequency component of the stator current is the source of rotor position of the drive system.

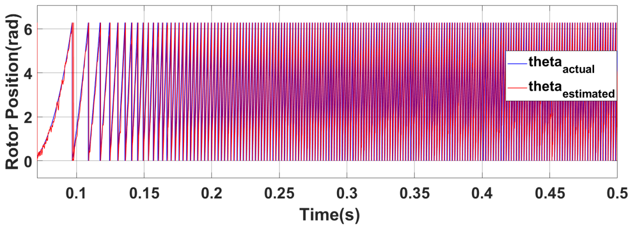

(a) Actual and Extracted Rotor Position for Motor Speed, 0 - 2000rpm.

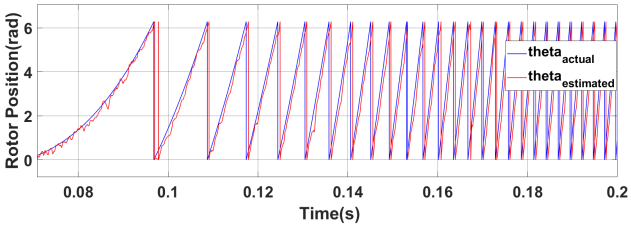

(b) Actual and Extracted Rotor Position, Magnified.

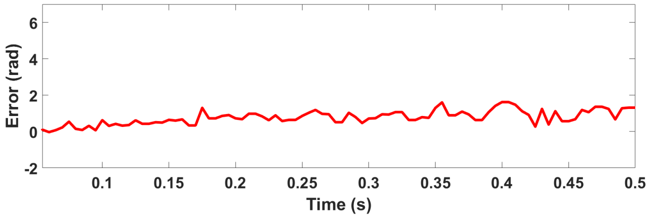

(c) Estimated rotor position error.

Figure (5.10) Performance of Rotor Position Information Extraction From The Bias Frequency Component of Stator Current, For Unloaded Drive.

Figure 5.10 shows the actual (sensed) and extracted (estimated) rotor position of the unloaded motor driven from 0 to 2000rpm. Figure 5.10b is a magnified version of figure 5.10a, for the clear inspection of the tracking performance of the extracted signal to the actual signal. From figure **??**, a pulsating rotor position at low speed and at steady state is obtained, but a much better response is obtained as the speed of the motor increases towards the set point. The ripples at steady state of the unloaded drive are due to the reduced stator current of the drive at steady state, as described before, the rotor position of the proposed motor is extracted from the high frequency component of stator current of the motor. The ripples during startup on the extracted rotor position can be reduced by selecting the right bias frequency value for the modulating triangular waveform. To support these points, rotor position extraction for a loaded drive (figure 5.11) and for a drive operating in four quadrant (figure 5.12) are shown below.

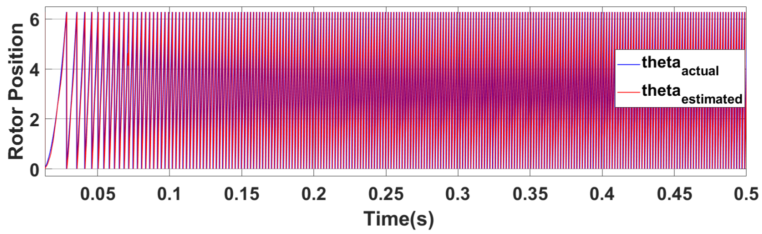

(a) Actual and Extracted Rotor Position for Loaded Motor, 0 - 2000rpm.

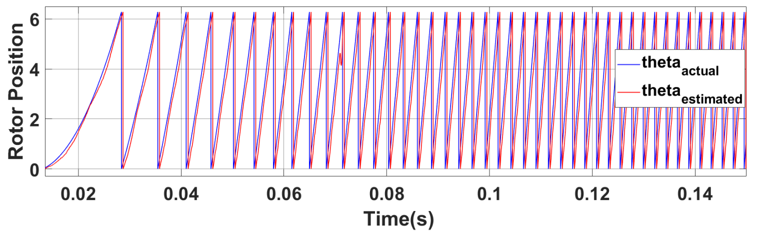

(b) Actual and Extracted Rotor Position, Magnified.

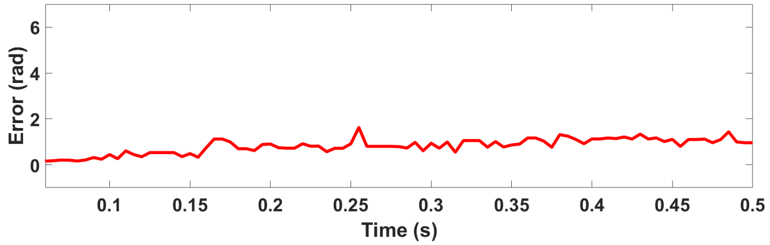

(c) Estimated rotor position error.

Figure (5.11) Performance of Rotor Position Information Extraction of A Loaded Motor Drive Based on The Bias Frequency Component of Stator Current.

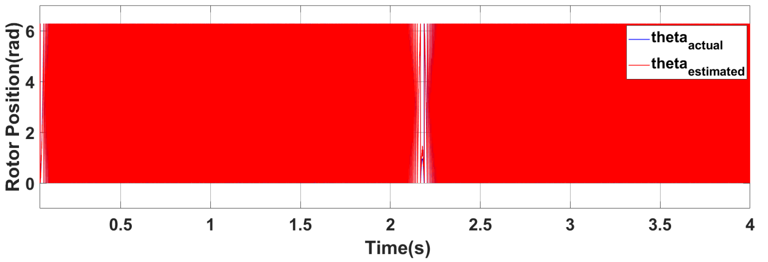

(a) Actual and Extracted Rotor Position for Loaded Motor, $(-6000rpm - 6000rpm)$.

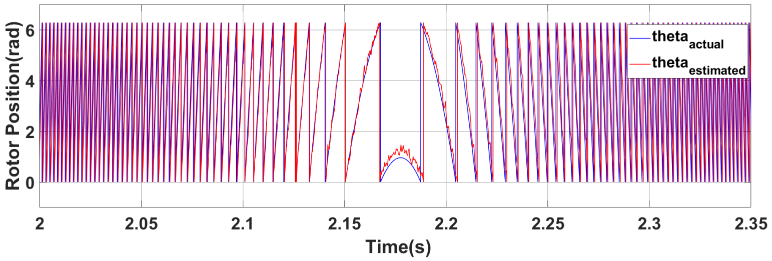

(b) Actual and Extracted Rotor Position, Magnified.

Figure (5.12) Performance of Rotor Position Information Extraction of A Loaded Motor Drive Based on The Bias Frequency Component of Stator Current.

Figure 5.10c and figure 5.11c shows the estimated error signals of the rotor position of the unloaded and loaded drive systems respectively. Figure 5.13 shows the comparison between the two error signals for the investigation of the effect of the load on rotor position estimation. The phase shift between the actual and estimated rotor position is the main cause of these error signals. The maximum error in both drive models is 1.62 rad.

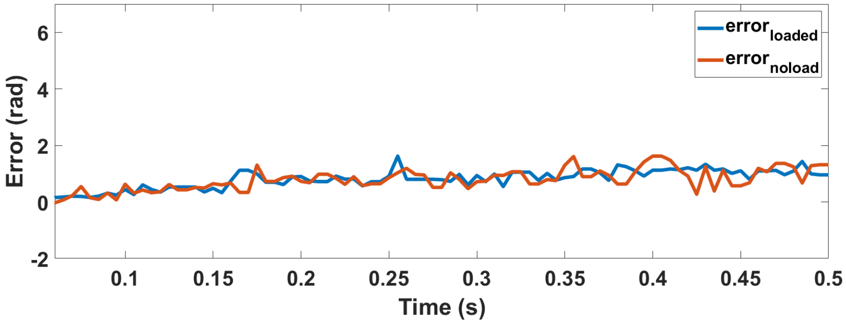

Figure (5.13) Estimated Rotor Position Errors for Unloaded and Loaded drive for Comparison.

5.3 Performances of MTPA and Flux Weakening Control Techniques

5.3.1 Performance of The MTPA Control Strategy

In order to examine the performance of the MTPA control strategy, it is necessary to compare it with the other control strategies. The $i_d = 0$ control method is one method of control, but it is not applicable for the control of HRreSM and using a constant reference i_d current value is another method of control for a drive system with HRreSM [12]. Next comparison between the MTPA based control model and the constant i_d based control model will be discussed based on the generated maximum torque and peak stator current value of the drive systems.

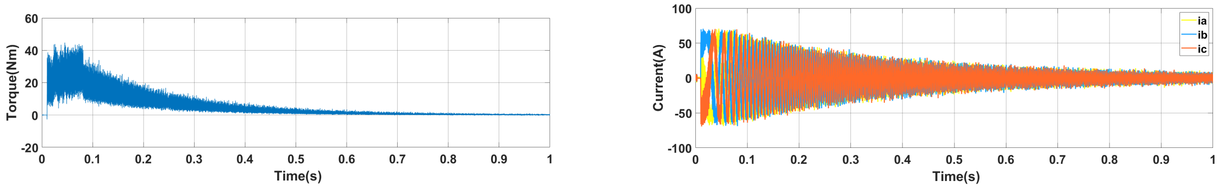

(a) Motor Torque under MTPA Control

(b) 3-Phase Stator Current under MTPA

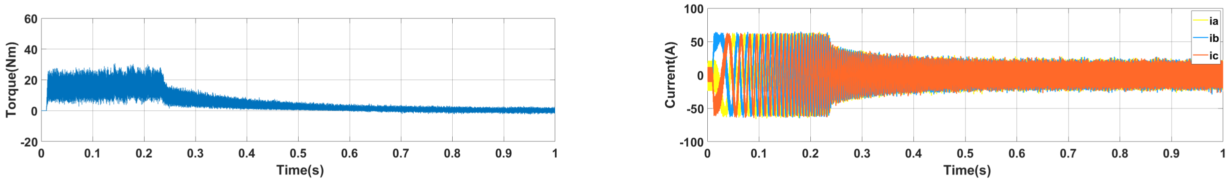

(c) Motor Torque under constant i_d Control

(d) 3-Phase Stator Current under constant i_d control

Figure (5.14) Comparison Between MTPA and Constant i_d Control Strategies, Analysing the Torque and Stator Currents.

Figure 5.14 show the comparison between MTPA control and constant i_d control. Both the developed MTPA and constant id control models are no-load and with step reference speed input (0 - 3000rpm). The i_{dref} value in the case of MTPA based control model is determined from the MTPA algorithm, while in the case of constant id based control model constant $i_{dref} = 30\,A$ value is used, which is equivalent to the output id current component (rms) of the MTPA model. Under the MTPA based control system the maximum registered average torque and stator currents are $25.82\,Nm$ and $64A$ respectively. Under the constant id control model the generated average motor torque is below $16.9Nm$ and the peak stator current is $62A$.

Based on the results, implementing MTPA control strategy to the proposed FOC model generates 52.78% more torque than the constant i_d based control model. Even if the maximum current output of the constant

i_d control is lower than the MTPA control, there is still high current generation at steady state of the constant i_d control model, which increases the losses of the drive significantly.

5.3.2 Performance of The Flux Weakening Control Technique

Figure 5.15 shows the performance comparison between two models. The first model is a control model with MTPA control strategy only. The second model added FW control technique to the first MTPA based control model. These models have been examined by setting a random step reference input of 13,600rpm speed. The purpose of this investigation is to know how much the MTPA control model drives the system and the benefit of having FW technique for speed range extension of the motor.

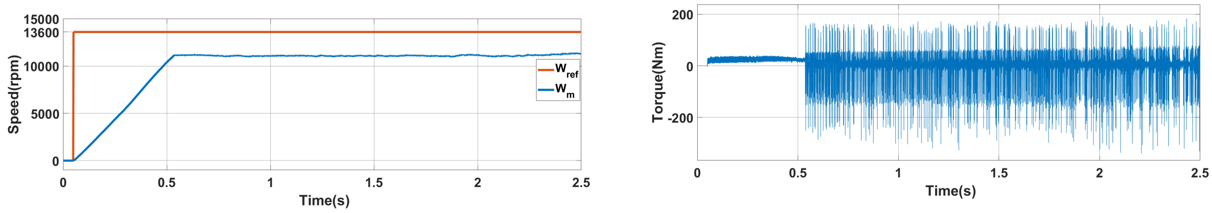

(a) Motor Speed under MTPA Control

(b) Motor Torque under MTPA Control

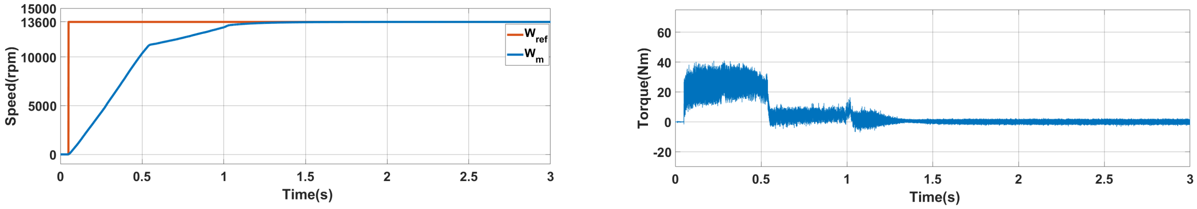

(c) Motor Speed under MTPA and FW Control

(d) Motor Torque under MTPA and FW Control

Figure (5.15) Comparison of MTPA based Model With MTPA and FW Based Control Model.

In the figure 5.15a and 5.15b, the limiting speed value for MTPA based control is clearly shown. Once the motor speed reaches the base speed $(11,400\ rpm)$, the control model saturates, it couldn't produce any reasonable torque to drive the motor above that speed. FW control technique is added to the prior MTPA based model and the results shown in the figures 5.15c and 5.15d are obtained.

When FW technique is added to support the MTPA based control model, it is done by applying the FW control strategy after the base speed of the motor. After this speed the FW control model takes part and performs well upto the command speed, 13600rpm. But the model's speed response to the step reference input shown in figure 5.15c may not look perfect. The response can be improved by re-tuning the controller parameters.

So the MTPA and FW based FOC of HRreSM model can employ MTPA control strategy upto the base speed and FW control strategy after the base speed of the motor. By doing that 21.97% speed extension beyond the speed limit of the MTPA based model (base speed) is obtained by implementing MTPA and FW control strategies consecutively.

5.4 Speed and Torque Performances of The Complete FOC

In this section, the performances of the speed and torque of the drive model are analyzed under different reference speed signals and load conditions.. For the purpose of clear inspection of the FW control strategy, the models studied in this section applied FW control strategy after motor speed of $2700\,rpm$.

5.4.1 Speed Performances

It is always crucial to know the performance of the MTPA based control model of the drive system to converge to the reference command signal. This criterion has been well accepted as a primary indicator when benchmarking the performance of a control model. The performance of the speed controller, tracking performance, of the drive system under no-load condition can be examined by changing the speed reference of the system, i.e. under the step response, increasing stair case, decreasing stair case and reverse speed conditions.

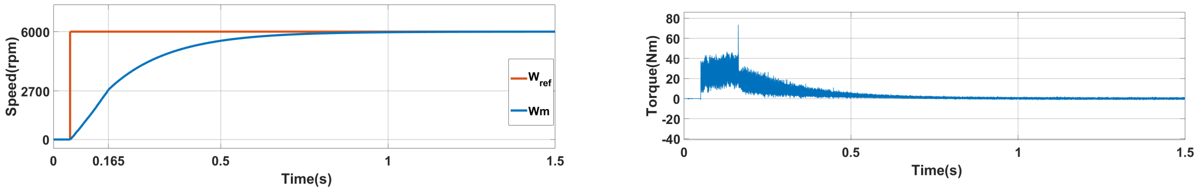

(a) No-Load Command and Motor Speed

(b) Motor Torque

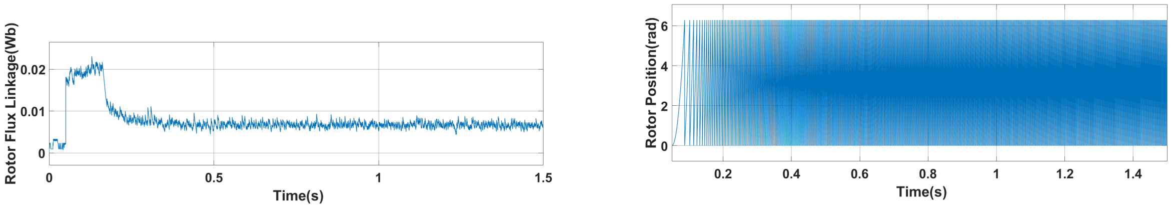

(c) Field Winding Flux Linkage

(d) Rotor Position

Figure (5.16) No-Load Transients, and Steady State Responses For Reference Step Input.

Figure 5.16 shows the performance of the drive system to a step command signal. The proposed MTPA based drive system control model tracks the step signal reference input. This shows the tracking performance of the control model to the reference speed. The drive system with step reference input has approximately 0% steady state error and transient performance with rise time of $0.3421sec$.

To reach the required steady-state speed, the motor must generate the adequate torque. This is made possible by increasing and maintaining constant at the peak value of the q-axis current (i_q) as well as d-axis current (i_d), look at figures 5.17a and 5.17b. This is happened by the employed MTPA control strategy, i.e. the optimal d-q axis current components are calculated based on the reference torque generated from the speed PI controller. With MTPA control generating maximum torque while minimizing the stator current during the starting and operating condition, upto the base speed, of the motor under no-load condition made possible. As the motor approaches steady state condition, and since the load torque is zero, the amounts of dq-axes currents required to keep the motor running will drop. In this control approach the actual d-axis current never follows the reference d-axis current, since the employed d-axis reference current is time-varying and it is difficult to design an infinite gain current regulator [12]. Figure 5.17a verifies this point.

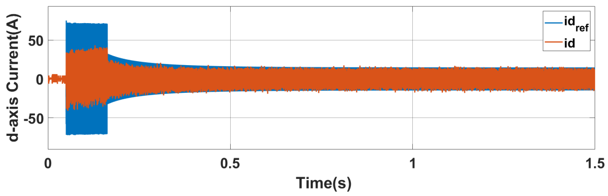

(a) d-axis Stator Current Component

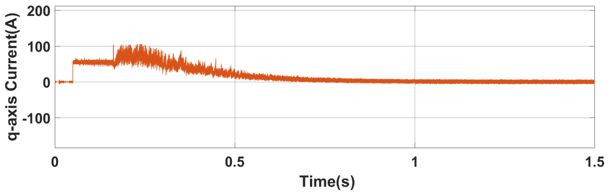

(b) q-axis Stator Current Component

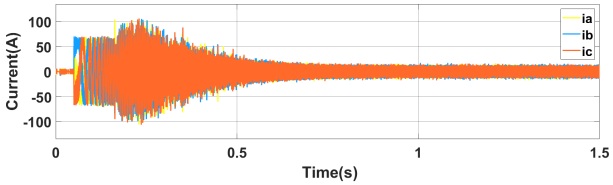

(c) Three Phase Stator Current

Figure (5.17) Stator Current and its d-q axes Components at no-load for a reference step input.

The drive efficiency under no-load condition is tried to be described using the speed-torque and speed-power characteristic curves. Figure 5.18 shows the drives operation in the constant torque region up to the speed of $2700\,rpm$ and in the flux weakening region after the this speed, figure 5.18b shows the non-constant power in the flux weakening region, [12] described this character of the motor as a drawback.

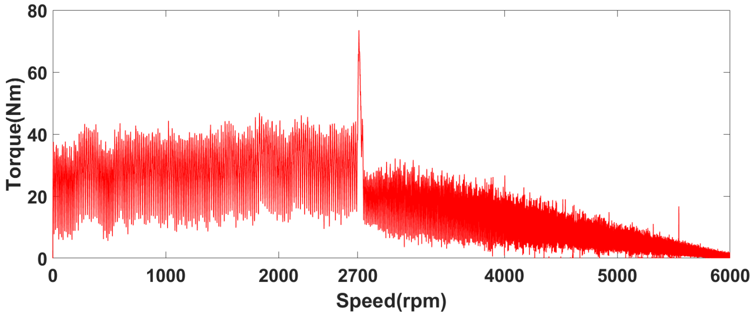

(a) Speed-Torque Characteristics Curve

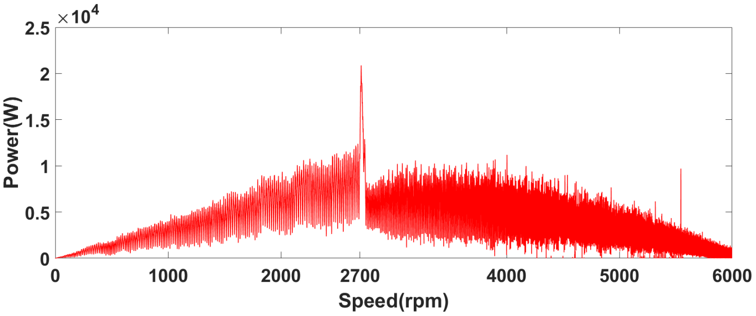

(b) Speed-Power Characteristics Curve

Figure (5.18) Speed-Torque and Speed-Power Characteristics of HRreSM.

Figure 5.19 shows the response of the drive system to the direction reversal speed command. As the motor drive obtains speed decreasing command at $t = 1.5sec$, it tries to slow down the motor by creating a negative q-axis current which in turn creates torque in opposite direction. From figure 5.19, the negative i_q can be seen and it is the result of the reversed current sequence (see figure 5.19c). The position of the motor is shown in figure 5.19d, where at zero speed the slop of the position plot is zero. After this zero slop value, the negative slop inverse-tangent plot follows and continues this way as long as the required speed is in the reverse direction.

Figure 5.20 shows the increasing staircase operation of the drive system by applying step reference signals at $t = 0.05sec$, $t = 1.5sec$, $t = 2.5sec$ and $t = 3.5sec$. After the motor reaches steady state in the first step response ranges (from $t = 0.05sec$ to $t = 1.5sec$), the operating stator current is very small as show in the figure 5.20b. When step speed increase command is obtained, the motor increases torque by increasing stator current. And the process continues for the remaining increasing stairs.

For case of the decreasing staircase operation, the motor operates in a similar way as in the case of the increasing staircase operation except that negative torque is used to decrease the speed of the motor, Figure 5.21 shows this operation. In this case, negative torque (where the q-axis current is also negative) is generated during the decreasing of the driving electrical speed, which is through the frequency control of the inverter. So, figure 5.21b shows stator phase currents with lower frequency as the speed decreases. Also as the speed decreases the frequency of the rotor position signal also decreases as shown in the figure 5.21c

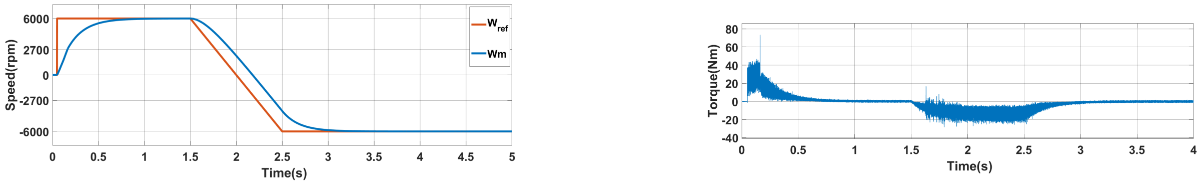

(a) No-Load Command Speed and Motor Speed

(b) Motor Torque

(c) q-axis Stator Current Component

(d) d-axis Current Component

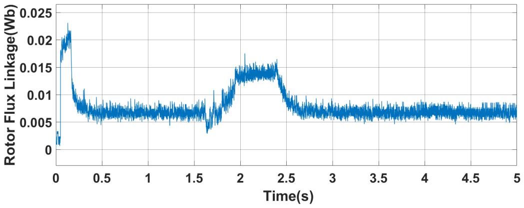

(e) Field Winding Flux Linkage

Figure (5.19) No-Load Speed Reversal Operation.

(a) No-Load Motor Speed

(b) Three Phase Stator Current

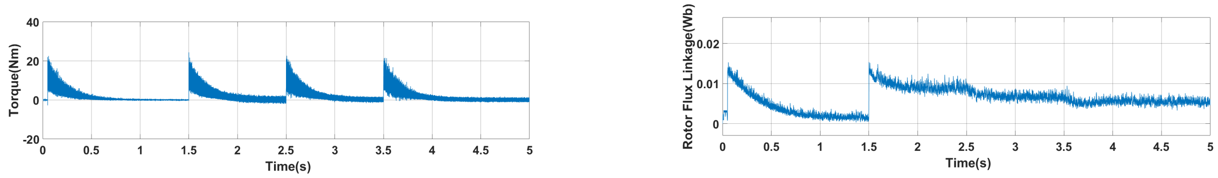

(c) Motor Torque

(d) Rotor Flux Linkage

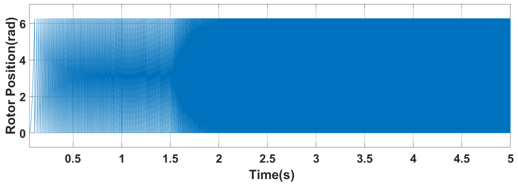

(e) Rotor Position

Figure (5.20) No-Load Transients, and Steady State Responses for Increasing Stair Case Operation.

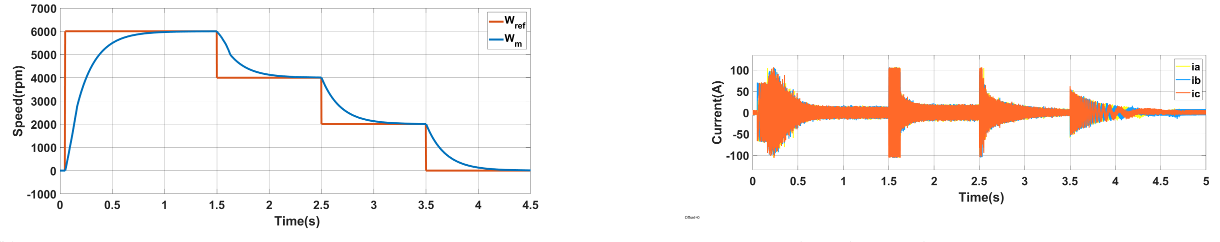

(a) No-Load Motor Speed

(b) Three Phase Stator Current

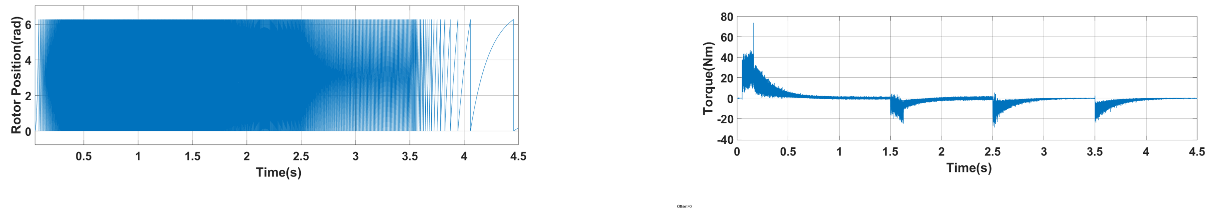

(c) Rotor Position

(d) Motor Torque

Figure (5.21) No-Load Transients, and Steady State Operations For Decreasing Stair Case Operation.

5.4.2 Torque performances

Under this section, the drive performance after introducing load to the motor from the starting and applying a load after the starting are investigated and presented. Consider Figure 5.22. The motor operates as the same way as shown in Figure 5.16 until a load (5Nm) is applied at t = 1.25sec. At this time, the motor's stator current increases from the very small value it has been to some higher value and is maintained at this value in order to keep the motor running at the required speed by driving the load specified. In Figure 5.22c, the increase in these currents' values is illustrated. When the load torque is applied the speed drop from $5991.8rpm$ to $5990.4rpm$ is registered and the drive immediately tracks the reference.

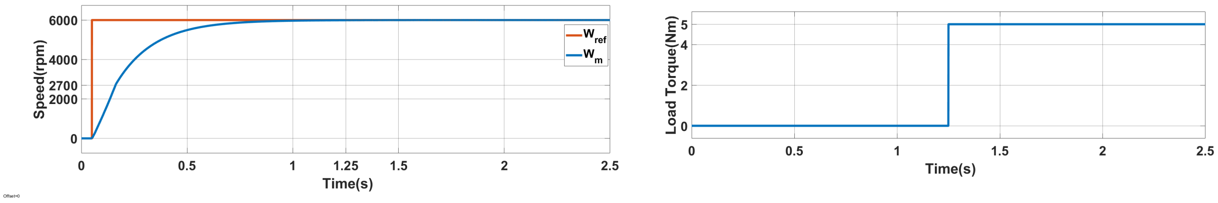

(a) Motor Speed

(b) Load Torque

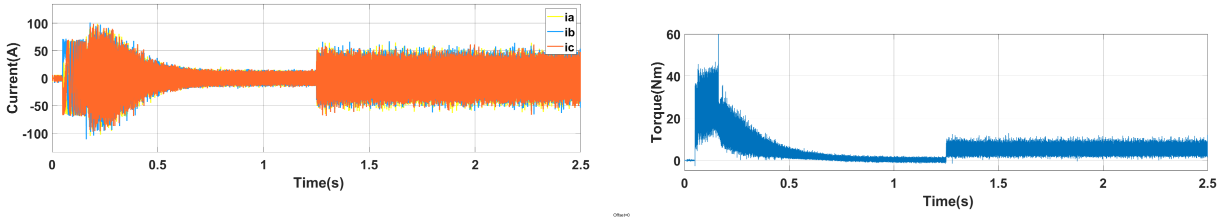

(c) Three Phase Stator Current

(d) Motor Torque

Figure (5.22) Transients, and Steady State Operations of a Drive Commanded to Reach a Constant Speed While Load Applied After The Motor Started.

If the the motor started loaded ($T_L = 2.5Nm$) beginning from the starting time, the drive performance shown in the figure 5.23 is obtained. The drive system with step reference, shown in the figure 5.23a, has approximately 0% steady state error and transient performance with rise time of $0.38025sec$. From the figure 5.23 the stator current don't decrease to a very small value once the drive is in steady state condition as it does in the no-load condition, Instead it maintains a value that allows the motor to produce enough torque in order to drive the load torque at the required speed. Besides the starting current of the motor is very large.

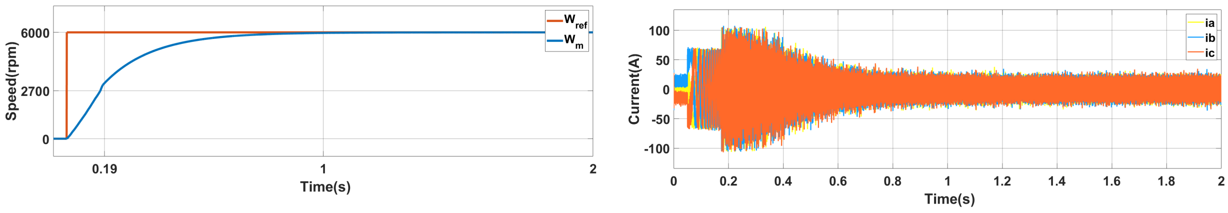

(a) Loaded Motor Speed

(b) Three Phase Stator Current

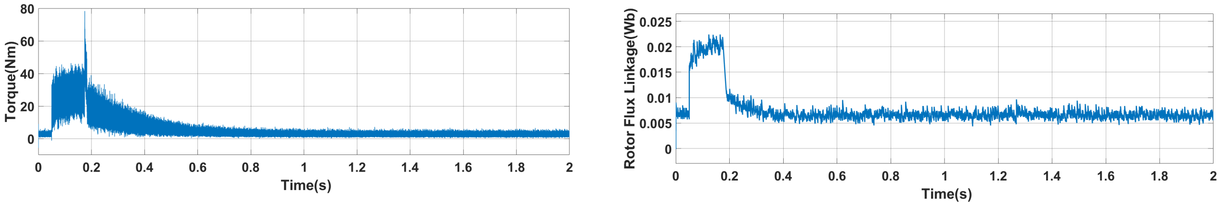

(c) Motor Torque

(d) Rotor Flux Linkage

Figure (5.23) Transients, and Steady State Operations of a Loaded Drive System Commanded to Reach a Constant Speed.

The increasing stair case operation of the motor under loaded condition, given in the Figure 5.24 is the same as that of no-load increasing stair case operation except that the q-axis currents have higher value to support the loaded drive. As shown in the figure 5.24c, the i_q value reaches the rated current value, $100\,A$, when the speed increases above $4000\,rpm$. The rotor flux linkage signal, figure 5.24b, shows the exact operation of the drive in the flux weakening region. Generally the drive generates the maximum possible motor torque even if the drive operating range is in the flux weakening region.

(a) Loaded Motor Speed

(b) Rotor Flux Linkage

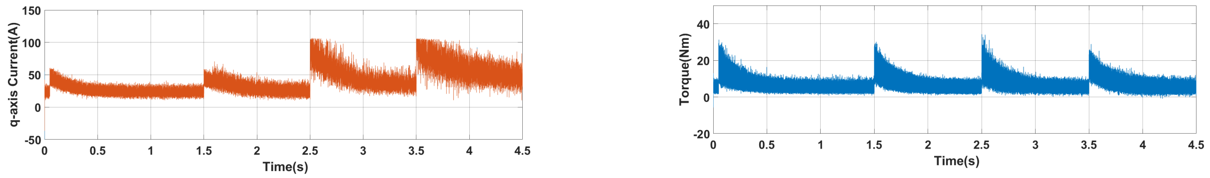

(c) q-axis Stator Current Component

(d) Motor Torque

Figure (5.24) Motor under Load Transients, and Steady State Operations For Increasing Stair Case Operation.

The decreasing operation of the motor under loaded condition, given in the Figure 5.25 is the same as that of no-load decreasing stair case operation except that the q-axis currents have higher value to support the loaded drive. As shown in the figure 5.25b, first the rotor flux linkage value increase when the drive enters to the constant power region, then when the speed gradually decreases the drive get back to the MTPA control region and the flux starts to rise and maintains constant value.

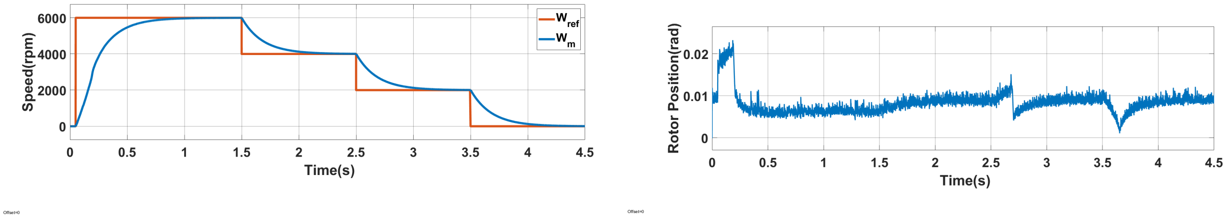

(a) Loaded Motor Speed

(b) Rotor Flux Linkage

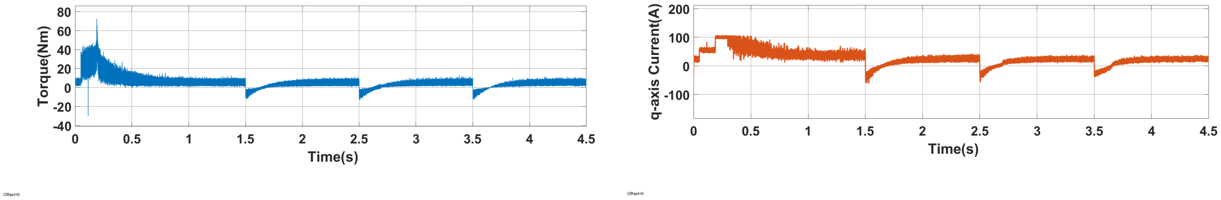

(c) Motor Torque

(d) q-axis Stator Current Component

Figure (5.25) Motor under Load Transients, and Steady State Operations For Decreasing Stair Case Operation.

The speed reversal operation under loaded condition is studied as shown in the figure 5.26, the four quadrant operation is studied by engaging the drive system for an electric vehicle purpose. In the figure 5.26b, just like the flux linkage signal from figure 5.19e of the unloaded drive response for a speed reversal reference input, the flux linkage value increases and maintains some value, in the range $t = 2.5\,sec$ to $t = 3\,sec$. This is due to the optimal d-axis current value, from the MTPA control, increases in this range in order to generate a higher torque, as shown in the figure 5.26d. Deacreasing the load torque value can make the rotor flux linkage of fig. 5.26b to converge to the rotor flux linkage of fig. 5.19e.

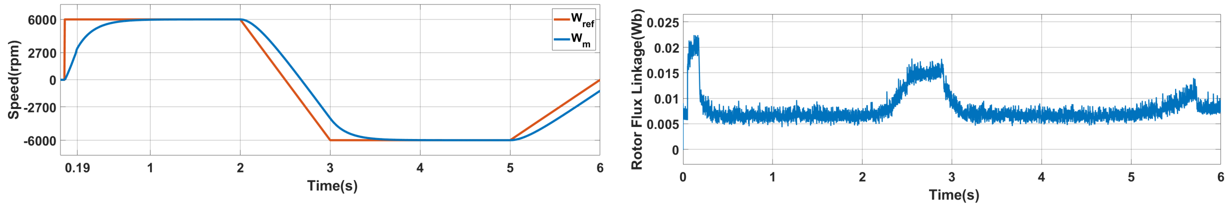

(a) Loaded Motor Speed

(b) Field Winding Flux Linkage

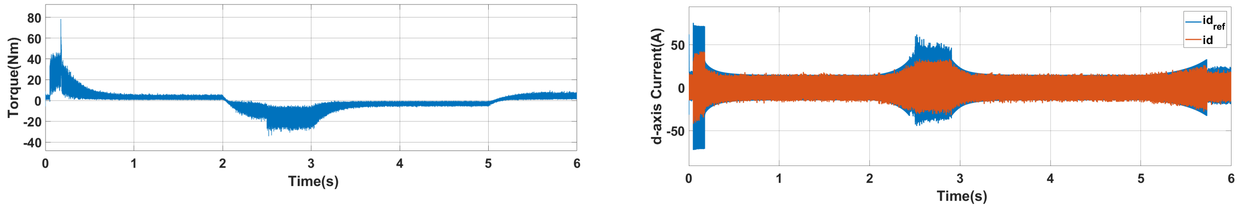

(c) Motor Torque

(d) d-axis Stator Current Component

Figure (5.26) Speed Reversal Operation For an EV, Four Quadrant Operation.

Chapter 6

Conclusion and Future Works

6.1 Conclusion

In this thesis study, the MTPA based sensorless control of HRreSM is demonstrated by using MATLAB/ Simulink, Simscape and Ansys Electronics/ Simplorer integrated simulation environment. During the modeling of the proposed sensorless drive control model, MATLAB/ Simulink is used for controller modeling, SVPWM inverter gate control signal generation and sensorless rotor position extraction. MATLAB/ Simscape is for motor, HRreSM, modeling. And Simplorer is for realistic VSI modeling. After properly modeling each individual models on each softwares, the performance of the whole model on the integrated simulation environment is examined. The MTPA based control of the proposed drive system is demonstrated to be effective upto the base speed, for maximum torque generation while minimizing stator current. And the FW control of the drive makes the motor operation to be extended beyond the base speed. This FOC model also includes the sensorless rotor position information extraction from the bias frequency component of the stator current, where it's effectiveness is demonstrated by comparison with the actual (sensed) rotor position of the motor. This MTPA based sensorless control model is directly applicable for the proposed application area, Electric Vehicle (EV), since it produces enough torque at starting, during acceleration and when external load is applied and motor operation beyond the base speed is demonstrated to be possible.

The 3-phase synchronous motor, HRreSM, studied in this thesis is neither brushed connection nor PM based for the field winding excitation. It has a stator winding identical to the conventional SM or IM and the rotor/ field winding short circuited through a diode. In the field winding a time-varying voltage is induced by the application of a modulated time-varying d-axis current. The induced time-varying voltage induces a time-varying flowing current with in the field winding. A DC current for the field winding excitation is produced by rectifying the time-varying current using field winding short circuiting diode. Important performance characteristics, such as the d-axis stator current controlled variable field flux, wide range of operation beyond the base speed, expected efficiency characteristics and possible controllability of torque, are displayed by the developed controlled HRreSM based drive system.

The performance study of the realistic VSI model (on Simplorer) is performed by making a comparison with the Simulink ideal VSI model. The same SVPWM gate control signals and the same lowpass filters are employed to these 3-phase realistic and ideal VSI models. The outputs, phase voltage signals, of the two models are used for inspection. After performing FFT analysis to these VSI output signals, a 2.108% THD and 1.49% peak value differences are registered. From the results, the realistic model has higher THD and lower peak value of the phase voltage as compared to the ideal VSI model. Since there is no much significant difference between the outputs of these two models, there is high convergence of the realistic model into the ideal model. So, using Simplorer for power electronic circuit modeling, like VSI model of this study, can make the drive system modeling more realistic and practically possible.

The rotor position information of HRreSM is extracted from the bias frequency component of the stator current without any required high frequency signal injection. After selecting the right bias frequency, 1.5kHz, of the triangular waveform during the modulation of the stator d-axis reference current, a better rotor position estimation is obtained. The performance of this sensorless rotor position estimation technique is demonstrated by comparing the estimated rotor position with the actual rotor position of the motor. From the simulation results the bias frequency based rotor position extraction technique is found effective for both low and high motor operating speeds, where high speed means beyond the base speed. This extracted rotor position information can be used as a source of rotor flux position for the decoupling of the stator current in the field oriented control of the HRreSM.

From the investigation of the MTPA and FW control model performances, the effectiveness of the two control models is demonstrated. The performance study of the MTPA control strategy is made by comparing the MTPA based FOC of HRreSM with constant i_d based FOC. The result shows a 52.78% more torque and almost the same peak stator current production by employing MTPA control strategy in our control model. Besides the constant i_d control model generates higher stator current at steady state than the MTPA control, which increases the stator current losses at steady state. The performance analysis of the FW control strategy is implemented by applying the FW control after the speed limit of the MTPA based control model. Based on the results, the FW based control model (MTPA and FW applied consecutively) drives the system above the limit speed of the MTPA based control model(where MTPA is applied for the whole speed range of the drive), i.e. 21.97% motor speed extension beyond the limit of the MTPA control (base speed). Therefore, MTPA and FW based FOC of HRreSM model should employ MTPA control strategy upto the base speed and FW control strategy after the selected base speed.

In this model, transition of control mode, MTPA to FW, is simply implemented by using the ”if condition”, i.e. MTPA for $\omega_m \leq \omega_{base}$ and FW for $\omega_m > \omega_{base}$. Both the MTPA and FW techniques generate the optimal dq-axes current components in different ways. This has an impact on the smooth operation of the drive, even if it is minor. This kind of effects got magnified during the modeling of loaded drive, the effects could be ignored or avoided by tuning the controller parameters or by changing the reference speed input signal, use ramp reference speed input signal. The ramp reference speed input is valid for the proposed EV application.

6.2 Future Works

In the motor modeling of this paper, MATLAB/ Simscape has been used. If realistic motor modeling on COMSOL Multiphysics is used, a more realistic responses of the drive system could have been obtained. So, it is recommended for the future work.

Transition of control mode modeling should be done in the way, to interact the two functions (i_{dq}), on MTPA and FW. So the smoother operation of the drive system is obtained without the need to change controller parameters or reference speed input signal.

On this thesis, after calculating the required motor ratings based on the vehicle dynamics of an electric vehicle (Tesla model S), the discussed model results for one motor are obtained. The calculated power rating of the motor was 220kW, which must be fulfilled by employing more than one HRreSMs. Here model and demonstration for one motor with 71.6kW is provided. Torque, 190Nm (required motor torque to drive the electric vehicle) division modeling by employing more than one HRreSMs is recommended for the future work.

References

[1] C. Chan, K. Chau *et al.*, *Modern electric vehicle technology*. Oxford University Press on Demand, 2001, no. 47.

[2] M. Preindl and S. Bolognani, "Model predictive direct torque control with finite control set for pmsm drive systems, part 1: Maximum torque per ampere operation," *IEEE Transactions on Industrial Informatics*, vol. 9, no. 4, pp. 1912–1921, 2013.

[3] T. A. Huynh and M.-F. Hsieh, "Performance analysis of permanent magnet motors for electric vehicles (ev) traction considering driving cycles," *Energies*, vol. 11, no. 6, p. 1385, 2018.

[4] A. H. Isfahani and S. Sadeghi, "Design of a permanent magnet synchronous machine for the hybrid electric vehicle," *World academy of science, engineering and technology*, vol. 45, pp. 566–570, 2008.

[5] S. Nonaka and K. Fujii, "Brushless self-excited three-phase synchronous motor driven by voltage source inverter," *Electrical engineering in Japan*, vol. 103, no. 4, pp. 81–89, 1983.

[6] Y. Hirakawa, T. Higuchi, Y. Yokoi, and T. Abe, "Characteristics of a half-wave rectified brushless synchronous generator," in *2014 International Power Electronics Conference (IPEC-Hiroshima 2014-ECCE ASIA)*. IEEE, 2014, pp. 3024–3028.

[7] J. Oyama, T. Abe, T. Higuchi, E. Yamada, and K. Shibahara, "Sensor-less control of a half-wave rectified brushless synchronous motor," in *IAS'95. Conference Record of the 1995 IEEE Industry Applications Conference Thirtieth IAS Annual Meeting*, vol. 1. IEEE, 1995, pp. 69–74.

[8] J. Oyama, T. Higuchi, T. Abe, and E. Yamada, "Analysis of half-wave rectified brushless synchronous motor with permanent magnets," in *Conference Record of the 1990 IEEE Industry Applications Society Annual Meeting*. IEEE, 1990, pp. 146–151.

[9] A. Iqbal and O. Singh, "Maximum torque per ampere control of six-phase synchronous motor," in *2016 International Conference on Control, Computing, Communication and Materials (ICCCCM)*. IEEE, 2016, pp. 1–5.

[10] S. H. Hosseini and M. Tabatabaei, "Ipmsm velocity and current control using mtpa based adaptive fractional order sliding mode controller," *Engineering science and technology, an international journal*, vol. 20, no. 3, pp. 896–908, 2017.

[11] H. Hida, Y. Tomigashi, and K. Kishimoto, "Novel sensorless control for pm synchronous motors based on maximum torque control frame," in *2007 European Conference on Power Electronics and Applications*. IEEE, 2007, pp. 1–10.

[12] M. Mamo and G. Fikadie, "Modeling and control of half-wave rectified rotor brushless synchronous motor," Ph.D. dissertation, Addis Ababa University, 2020.

[13] J. Yamaguch, S. Toba, T. Higuchi, and E. Yamada, "Principle and fundamental characteristics of half-wave rectified brushless synchronous motor," *Electrical engineering in Japan*, vol. 107, no. 6, pp. 98–106, 1987.

[14] S.-H. Kim, *Electric motor control: DC, AC, and BLDC motors*. Elsevier, 2017.

[15] M. Mamo, K. Ide, M. Sawamura, and J. Oyama, "Novel rotor position extraction based on carrier frequency component method (cfcm) using two reference frames for ipm drives," *IEEE Transactions on industrial electronics*, vol. 52, no. 2, pp. 508–514, 2005.

[16] N. T. Woldegebriel, "Rotor position extraction by carrier frequency component method (cfcm) in space vector modulation (svm) for ipm drives," Ph.D. dissertation, Addis Ababa University, 2015.

[17] H. Abu-Rub, A. Iqbal, and J. Guzinski, *High performance control of AC drives with MATLAB/Simulink models*. John Wiley & Sons, 2012.

[18] J. Holtz, W. Lotzkat, and A. M. Khambadkone, "On continuous control of pwm inverters in the overmodulation range including the six-step mode," *IEEE transactions on power electronics*, vol. 8, no. 4, pp. 546–553, 1993.

[19] D.-C. Lee and G.-M. Lee, "A novel overmodulation technique for space-vector pwm inverters," *IEEE transactions on Power Electronics*, vol. 13, no. 6, pp. 1144–1151, 1998.

[20] I. F II, "Ieee recommended practices and requirements for harmonic control in electrical power systems," *New York, NY, USA*, pp. 1–1, 1993.

[21] A. Kronberg, "Design and simulation of field oriented control and direct torque control for a permanent magnet synchronous motor with positive saliency," 2012.

[22] S. Halder, P. Agarwal, and S. Srivastava, "Mtpa based sensorless control of pmsm using position and speed estimation by back-emf method," in *2016 IEEE 6th International Conference on Power Systems (ICPS)*. IEEE, 2016, pp. 1–4.

[23] T. M. Jahns, G. B. Kliman, and T. W. Neumann, "Interior permanent-magnet synchronous motors for adjustable-speed drives," *IEEE Transactions on Industry Applications*, no. 4, pp. 738–747, 1986.

[24] R. W. De Doncker, D. W. Pulle, and A. Veltman, *Advanced electrical drives: analysis, modeling, control*. Springer Nature, 2020.

[25] M. Zeraoulia, M. E. H. Benbouzid, and D. Diallo, "Electric motor drive selection issues for hev propulsion systems: A comparative study," *IEEE Transactions on Vehicular technology*, vol. 55, no. 6, pp. 1756–1764, 2006.

[26] N. Hashemnia and B. Asaei, "Comparative study of using different electric motors in the electric vehicles," in *2008 18th International Conference on Electrical Machines*. IEEE, 2008, pp. 1–5.

[27] K. M. Rahman, B. Fahimi, G. Suresh, A. V. Rajarathnam, and M. Ehsani, "Advantages of switched reluctance motor applications to ev and hev: Design and control issues," *IEEE transactions on industry applications*, vol. 36, no. 1, pp. 111–121, 2000.

[28] M. Yildirim, M. Polat, and H. Kürüm, "A survey on comparison of electric motor types and drives used for electric vehicles," in *2014 16th International Power Electronics and Motion Control Conference and Exposition*. IEEE, 2014, pp. 218–223.

[29] H. Won, Y.-K. Hong, W. Lee, and M. Choi, "Roles of coercivity and remanent flux density of permanent magnet in interior permanent magnet synchronous motor (ipmsm) performance for electric vehicle applications," *AIP Advances*, vol. 8, no. 5, p. 056811, 2018.

[30] N. P. Quang, J.-A. Dittrich *et al.*, *Vector control of three-phase AC machines*. Springer, 2008, vol. 2.

[31] N. Matsui, "Sensorless operation of brushless dc motor drives," in *Proceedings of IECON'93-19th Annual Conference of IEEE Industrial Electronics*. IEEE, 1993, pp. 739–744.

[32] N. Kasa and H. Watanabe, "For practical use position and speed sensorless salient-pole brushless dc motor drives," in *Proceedings of Power Conversion Conference-PCC'97*, vol. 1. IEEE, 1997, pp. 127–132.

[33] M. J. Corley and R. D. Lorenz, "Rotor position and velocity estimation for a permanent magnet synchronous machine at standstill and high speeds," in *IAS'96. Conference Record of the 1996 IEEE Industry Applications Conference Thirty-First IAS Annual Meeting*, vol. 1. IEEE, 1996, pp. 36–41.

[34] M. Mengesha, J. Oyama, T. Abe, T. Higuchi, and E. Yamada, "Carrier frequency component method for position sensorless control of ipm motor in lower speed range," *IEEJ Transactions on Industry Applications*, vol. 120, no. 2, pp. 275–280, 2000.

[35] T. Aihara, A. Toba, T. Yanase, A. Mashimo, and K. Endo, "Sensorless torque control of salient-pole synchronous motor at zero-speed operation," *IEEE Transactions on Power Electronics*, vol. 14, no. 1, pp. 202–208, 1999.

[36] J.-I. Ha, S.-J. Kang, and S.-K. Sul, "Position-controlled synchronous reluctance motor without rotational transducer," *IEEE transactions on Industry Applications*, vol. 35, no. 6, pp. 1393–1398, 1999.

[37] S. Ogasawara and H. Akagi, "An approach to real-time position estimation at zero and low speed for a pm motor based on saliency," *IEEE Transactions on Industry Applications*, vol. 34, no. 1, pp. 163–168, 1998.

[38] O. Haedrich and U. Knorr, "Electric circuit and control system simulation by linking simplorer (r) and matlab/simulink (r) analysis of interactions of subsystems of modern electric drives," in *COMPEL 2000. 7th Workshop on Computers in Power Electronics. Proceedings (Cat. No. 00TH8535).* IEEE, 2000, pp. 192–196.

[39] A. K. Singh, P. Kumar, C. U. Reddy, and K. Prabhakar, "Simulation of direct torque control of induction motor using simulink, simplorer and maxwell software," in *2015 IEEE International Transportation Electrification Conference (ITEC).* IEEE, 2015, pp. 1–6.

[40] W. Emar, "Analysis, modeling and simulation of step up converter using matlab–simulink and simplorer," *International Journal of Modeling, Simulation, and Scientific Computing*, vol. 7, no. 02, p. 1650004, 2016.

[41] S. Morimoto, K. Hatanaka, Y. Tong, Y. Takeda, and T. Hirasa, "Servo drive system and control characteristics of salient pole permanent magnet synchronous motor," *IEEE Transactions on Industry Applications*, vol. 29, no. 2, pp. 338–343, 1993.

[42] P. Bimbhra and S. Kaur, *Power electronics*. Khanna publishers, 2012, vol. 2.

[43] N. S. Nise, *Control systems engineering*. John Wiley & Sons, 2020.

[44] J. C. Robinson, *An Introduction to Ordinary Differential Equations*. Cambridge University Press, 2004.

Appendices

Appendix A

Field Current Derivation, Voltage and Current Limits

A.1 Field Current

The field winding current (i_{fd}) is the current obtained by rectifying the induced current in the field winding by using a diode. It is the result of mutualism between the rotor winding and the stator d-axis circuit. This mutual interaction between the stator and rotor winding is described by an equivalent circuit in the figure A.1 taken from figure 2.2. The magnitude of this field current depends on many factors, some of them are the amplitude of the field excitation current (I_f), the motor parameters (resistance and inductance) and the bias frequency (f_b). For proper description of the motor, it is necessary to express the field winding current (I_{fd}) explicitly.

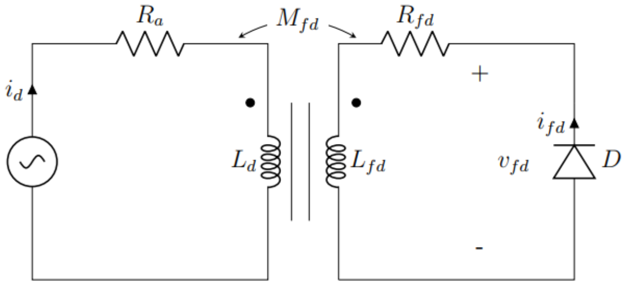

Figure (A.1) Simplified d-axis Equivalent Circuit.

The field circuit has two distinct operating states: Diode ON state and Diode OFF state. In figure A.2, the d-axis equivalent circuit of figure A.1 is used to describe these two states of the field winding circuit by assuming the diode employed is ideal.

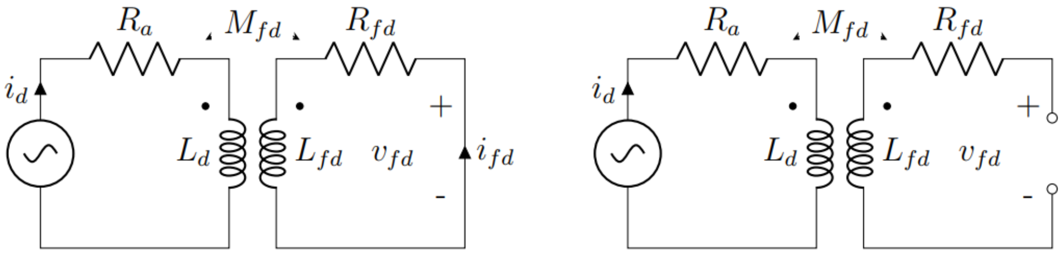

(a) Diode ON (b) Diode OFF

Figure (A.2) The Equivalent Circuit in Two Operation Modes.

The transformed component of the stator current i_d with the desired frequency and amplitude is going to be supplied to the inverter of the drive. In our case, based on the previous study by [13], triangular waveform is used for the modulation. The triangular waveform ($A_f(t)$) has a period of T_b and an amplitude of I_f. Mathematically, using piece-wise function i_d can be described as,

$$i_d(t) = \begin{cases} I_f - \dfrac{4I_f}{T_b}t & ;\ 0 \leq t \leq \dfrac{T_b}{2} \\ \\ -3I_f + \dfrac{4I_f}{T_b}t & ;\ \dfrac{T_b}{2} < t \leq T_b \end{cases} \tag{A.1}$$

Apply KVL for the equivalent circuit, where the field circuit is in the ON-operating state, to find the expression for the field current i_{fd}.

$$E_{fd} = 0 \tag{A.2}$$

Substituting

$$E_{fd} = R_{fd}i_{fd} + \frac{d}{dt}\psi_{fd} \tag{A.3}$$

Where

$$\psi_{fd} = L_{fd}i_{fd} + \frac{3}{2}M_{fd}i_d \tag{A.4}$$

A linear ODE is obtained by rearranging the above equation, which is given by

$$-\frac{3}{2}\frac{M_{fd}}{L_{fd}}\frac{d}{dt}\,i_d(t) = fracR_{fd}L_{fd}\,i_{fd}(t) + \frac{d}{dt}\,i_{fd}(t) \tag{A.5}$$

Solve for i_{fd} from equation (A.5). To find a solution for this kind of ODEs, use integrating factors method [44]. The solution becomes

$$R(t)e^{S(t)} = \frac{d}{dt}\left(i_{fd}(t)e^{S(t)}\right) \tag{A.6}$$

Where

$$R(t) = -\frac{3}{2}\frac{M_{fd}}{L_{fd}}\frac{d}{dt}i_d(t) \tag{A.7}$$

$$S(t) = \int \frac{R_{fd}}{L_{fd}}dt = \frac{t}{T_0} \tag{A.8}$$

Where T_o is the time constant of the field winding described as an RL circuit. And it can be expressed as $T_0 = \frac{L_{fd}}{R_{fd}}$.

After completing the derivation of the above equation of the ON state field winding circuit, the following expression of i_{fd}, for both the ON and OFF states of the circuit, will be obtained.

$$i_{fd} = \begin{cases} 4I_f\left(\frac{3}{2}\frac{M_{fd}}{L_{fd}}\right)r\left(1-e^{-t/T_0}\right) & , 0 \le t \le \frac{T_b}{2} \\ 4I_f\left(\frac{3}{2}\frac{M_{fd}}{L_{fd}}\right)r\left(2e^{1/2r-t/T_0} - e^{-t/T_0} - 1\right) & , \frac{T_b}{2} < t \le t_1 \\ 0 & , t_1 < t \le T_b \end{cases} \tag{A.9}$$

Where, r is the ratio of time constant of the R-L circuit to the bias period, (i.e. $r = \frac{T_0}{T_b}$).

During the second half of the excitation waveform full period, i_{fd} decays to zero. The time length of this decay of i_{fd} is determined by the parameter r. r also determines the OFF time of the circuit. For further understanding of the effects of r on the motor performance and detail derivation of the above equations refer [12].

A.2 Voltage and Current Limits

Above the rated or base speed (ω_{base}) of the motor, flux weakening control techniques is required under the voltage and current limit, since the stator current increases above its maximum value in order to generate the required torque, however the the stator voltage could not have the efficiency to generate that much current due to the increase of the back emf as the speed increases above the base speed. Thus, the voltage and current limit conditions must be clearly defined before analyzing the high speed operation of the motor. The voltage and current limits in terms of the d-q axes variables are defined as follows,

$$I_{s\_max}^2 \geq i_d^2 + i_q^2 \tag{A.10a}$$

$$E_{s\_max}^2 \geq E_d^2 + E_q^2 \tag{A.10b}$$

From the inverter ratings E_{s_max} and I_{s_max} are the maximum voltage and stator current values.

Based on the thermal and other constraints, the allowable range of d-q axes currents is specified by the current limit condition. A circle, in the d-q axes coordinates, centered at (0,0) and with radius of I_{s_max} is described in equation (A.10a). As shown in the figure A.3, the d-axis stator current is limited between the vertical broken black lines, i.e. $i_d = -I_f$ and $i_d = I_f$, which tells the existence of additional limiting condition in the d-axis current during the modeling and control of HRreSM. The intersection of the area between the two vertical lines and the area inside the circle determines the current limit area for this particular motor drive system [12].

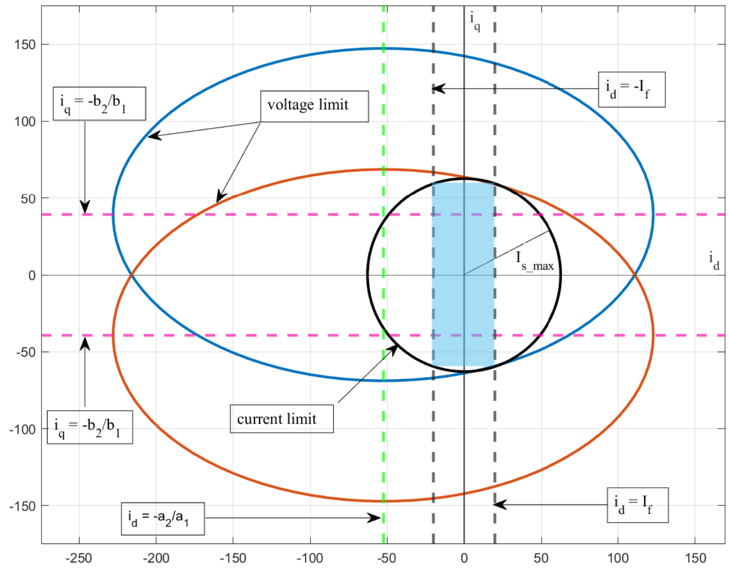

Figure (A.3) Curves Describing The Voltage and Current Limits, Considering The d-axis Current Limit Range, [12].

The maximum possible inverter output voltage driving the motor is represented by E_{s_max} of equation (A.10b). Neglecting the resistance voltage drop of the stator winding, let's rewrite equation (2.1) as follows.

$$E_d = R_a i_d - \omega\psi_q + \frac{d}{dt}\psi_d \approx -\omega\psi_q + \frac{d}{dt}\psi_d \tag{A.11a}$$

$$E_q = R_a i_q + \omega\psi_d + \frac{d}{dt}\psi_q \approx \omega\psi_d + \frac{d}{dt}\psi_q \tag{A.11b}$$

Set $\frac{d}{dt}\psi_f = 0$ by considering a steady state condition, use the i_{fd} expression in terms of a simplified d-axis current, shown in equation (A.12) and then substitute the variables into the voltage limit equation. The simplified form is described in equation (A.13).

$$i_{fd}(t) \approx \left(-\frac{3}{2}\frac{M_{fd}}{L_{fd}}\right) i_d(t) + I_f \left(\frac{3}{2}\frac{M_{fd}}{L_{fd}}\right) \tag{A.12}$$

$$\left(\frac{{}^{\alpha_2}/_{\alpha_1} + i_d}{{}^{E_{s\_max}}/_{\alpha_1}}\right)^2 + \left(\frac{{}^{\beta_2}/_{\beta_1} + i_q}{{}^{E_{s\_max}}/_{\beta_1}}\right)^2 \leq 1 \tag{A.13}$$

where

$$\alpha_1 = \left(-\frac{3}{2}\frac{M_{fd}^2}{L_{fd}} + L_d\right)\omega \tag{A.14a}$$

$$\alpha_2 = \left(\frac{3}{2}\frac{M_{fd}^2}{L_{fd}} I_f\right)\omega \tag{A.14b}$$

$$\beta_1 = -L_q\omega \tag{A.14c}$$

$$\beta_2 = \frac{d}{dt} i_d \left(-\frac{3}{2}\frac{M_{fd}^2}{L_{fd}} + L_d\right) \tag{A.14d}$$

Since an ellipse is formed from equation (A.13), let's now discuss the ellipse's geometrical parameters.

- length of minor axis

$$2\beta = 2\frac{E_{s\_max}}{\beta_1} = 2\frac{E_{s\_max}}{\omega L_q} \tag{A.15}$$

- length of major axis

$$2\alpha = 2\frac{E_{s\_max}}{\alpha_1} = 2\frac{E_{s\_max}}{\omega\left(L_d - \frac{3}{2}\frac{M_{fd}^2}{L_{fd}}\right)} \tag{A.16}$$

- center at

$$\left(-\frac{\alpha_2}{\alpha_1}, -\frac{\beta_2}{\beta_1}\right) = \left(\frac{\frac{M_{fd}^2}{L_{fd}}}{L_d - \frac{3}{2}\frac{M_{fd}^2}{L_{fd}}} * \frac{3}{2} I_f, -\frac{1}{\omega L_q} * \frac{d}{dt} i_d \left(L_d - \frac{3}{2}\frac{M_{fd}^2}{L_{fd}}\right)\right) \tag{A.17}$$

Two ellipses will be created since the sign of the $\frac{d}{dt}i_d$ term of equation (A.17) can be both negative and positive, see figure A.3. The voltage limit condition which is satisfied by any set of controllable dq-axes current will be determined by the intersection of these two ellipses. Therefore, in an inverter of rated voltage, working without exceeding the stator current's maximum allowable range, all the controllable dq-axes current values will be found inside the area created by the intersection of the voltage and current limit curves[12].

The ellipse's geometrical parameters are much dependent on the electrical angular speed ω, as it can be seen from the equations (A.15) to (A.17). As the speed extends beyond the rated speed, for a given constant voltage E_{s_max}, the length of the minor axes as well as the major axis decreases. This scenario causes a new center position, while shrinking the area covered by the ellipses of the voltage limit (look at figure A.4). Under the rated voltage of E_{s_max}, the combination of dq-axes currents from zero to I_{s_max} (rated stator current) is covered by the current and voltage limit curves upto the base speed ω_b of the motor. This case can be illustrated by the following figure A.4, where ω is equal to ω_1.

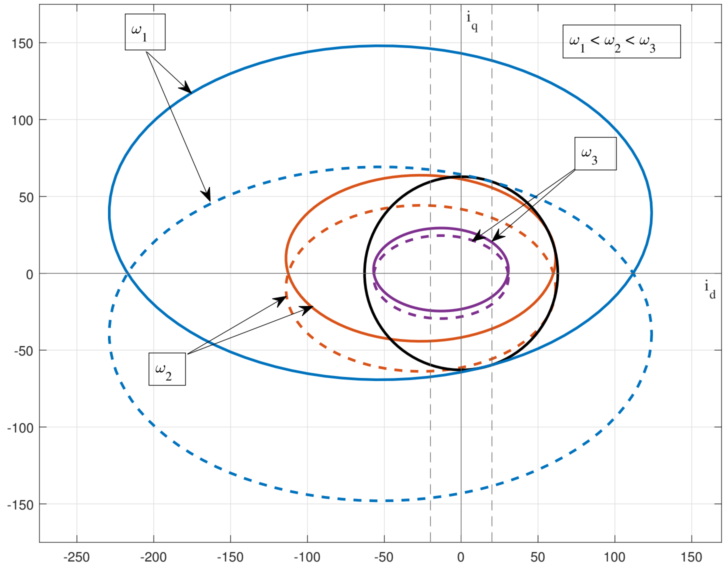

Figure (A.4) Voltage Limit Curves Under Different Electrical Angular Speed Values of The Motor (ω), [12].

At the base speed of the motor, when rated stator current is supplied, the stator voltage reaches its peak value, i.e. E_{s_max}. By taking the intersection of the two ellipses into consideration, equation (A.13) can be used to calculate the base speed value of the motor for a given E_{s_max}.

$$|\omega_b| = \frac{-8RSI_fI_tf_b + \sqrt{(8RSI_fI_tf_b)^2 - 4\left[((R+T)I_f)^2 + S^2I_t^2\right]\left[-V_{s\_max}^2 + (4RI_ff_b)^2\right]}}{2\left[((R+T)I_f)^2 + S^2I_t^2\right]} \tag{A.18}$$

Where

$$R = -\frac{3}{2}\frac{M_{fd}^2}{L_{fd}} + L_d \tag{A.19a}$$

$$S = -L_q \tag{A.19b}$$

$$T = \frac{3}{2}\frac{M_{fd}^2}{L_{fd}} \tag{A.19c}$$

In order to limit the stator voltage to the rated value for the high speed operation of the motor, the flux weakening contol technique starting from the base speed must be applied. For the stator current to be limited to the available inverter voltage, the back-emf of the motor must be limited to the desired level by employing any applicable flux weakening control technique. This back-emf of the motor is directly proportional to the field winding flux linkage and rotor angular speed of the motor [12]. In this study, the classic flux weakening control technique has been discussed. It is a strategy of reducing the field flux by changing or reducing the I_f values. Where I_f is the peak value of a triangular waveform which is used to modulate the normal stator excitation current. Then the maximum allowable current (I_t) satisfying both the voltage and current limit curves, for a given speed, can be calculated from the value of I_f.

$$I_t = \frac{4Rf_bI_f - \sqrt{V_{s\_max}^2 - \omega^2 I_f^2 (R+T)^2}}{\omega S} \tag{A.20}$$

The value of R, S, and T can be calculated from equation (A.19). The intersection of the ellipses of the voltage limit has been taken into consideration for the derivation of Equation (A.20).

Appendix B

Simulink® Complete Model

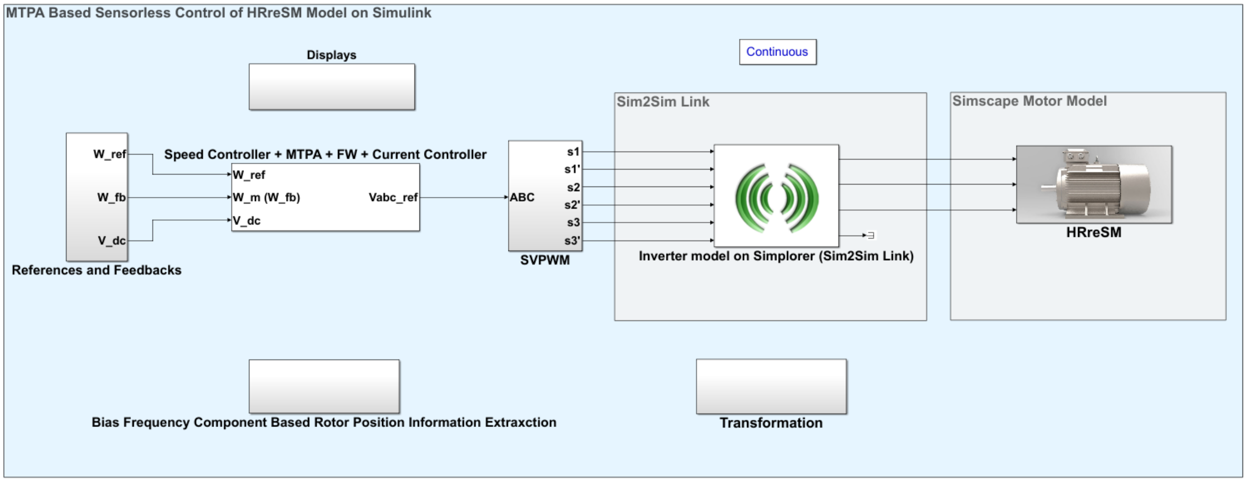

Figure (B.1) SIMULINK® Model of the Complete MTPA based Sensorless Drive System.

B.1 HRreSM

For the MATLAB code of the Simscape motor model refer [12].

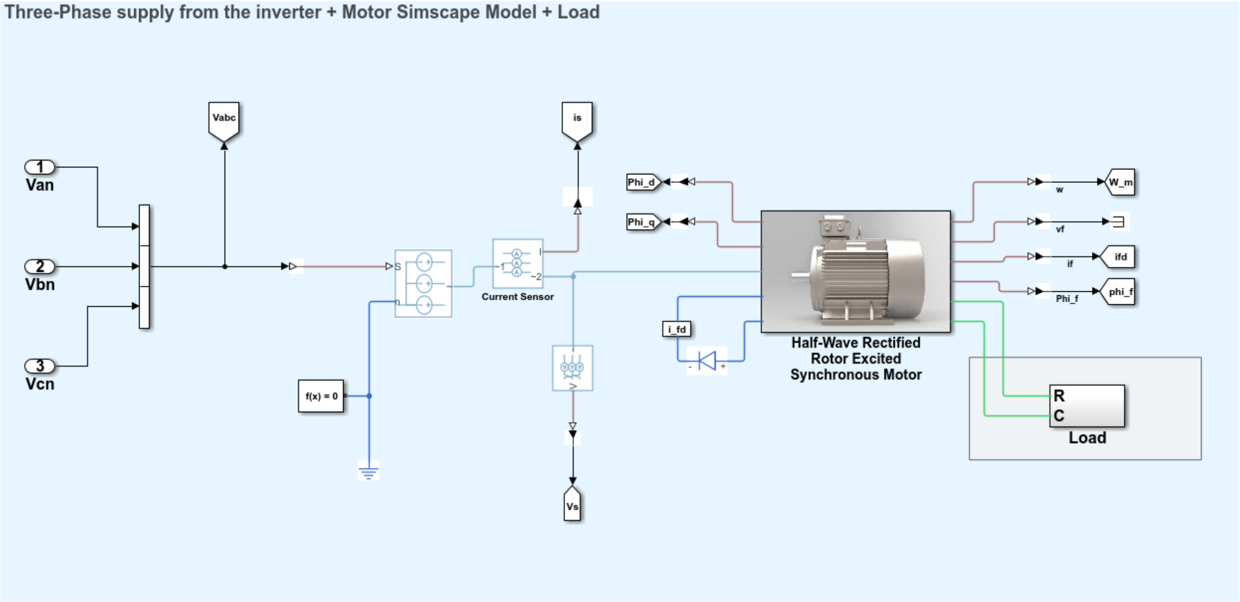

Figure (B.2) Extracting The HRreSM Block of Figure B.1

B.2 Simplorer Link Assignment Dialog Box (Block Named ”Inverter model from Simplorer (SIM2SIM Link))

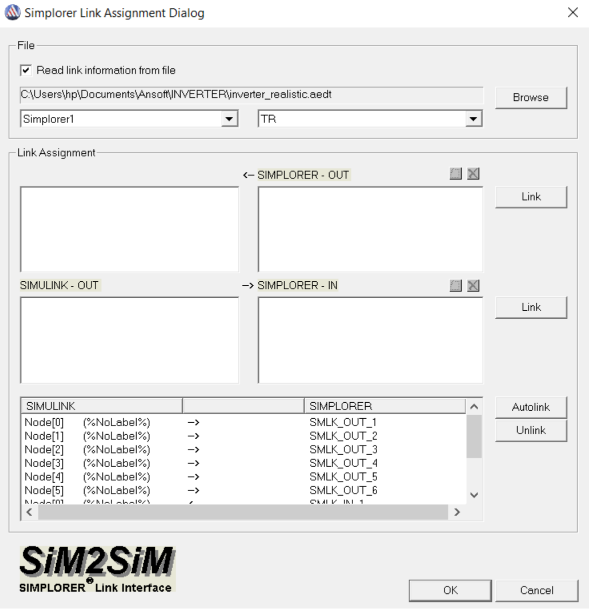

Simplorer Link Assignment Dialog

File

☑ Read link information from file

C:\Users\hp\Documents\Ansoft\INVERTER\inverter_realistic.aedt

Simplorer1

TR

Link Assignment

SIMULINK			SIMPLORER
Node[0]	(%NoLabel%)	–>	SMLK_OUT_1
Node[1]	(%NoLabel%)	–>	SMLK_OUT_2
Node[2]	(%NoLabel%)	–>	SMLK_OUT_3
Node[3]	(%NoLabel%)	–>	SMLK_OUT_4
Node[4]	(%NoLabel%)	–>	SMLK_OUT_5
Node[5]	(%NoLabel%)	–>	SMLK_OUT_6

Figure (B.3) Realization of Block Named ”Inverter Model on Simplorer (SIM2SIM Link) in The Figure B.1

B.3 SVPWM

Refer [16] for MATLAB code to be implemented inside the ”Three phase SVPWM” MATLAB Function block of figure B.4.

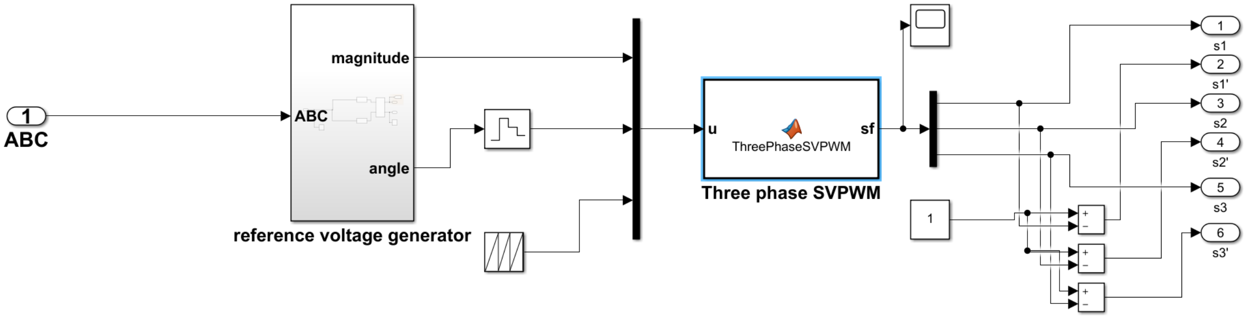

Figure (B.4) SVPWM Gate Signal Generation on SIMULINK, from SVPWM block of the Complete model

B.3.1 Reference Voltage Generator of the SVPWM

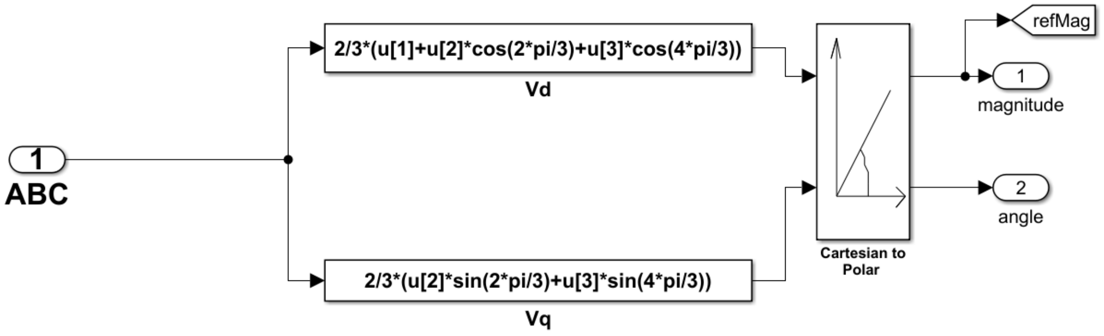

Figure (B.5) Extracting the Reference Voltage Generator Block of the Figure B.4

B.4 Transformation

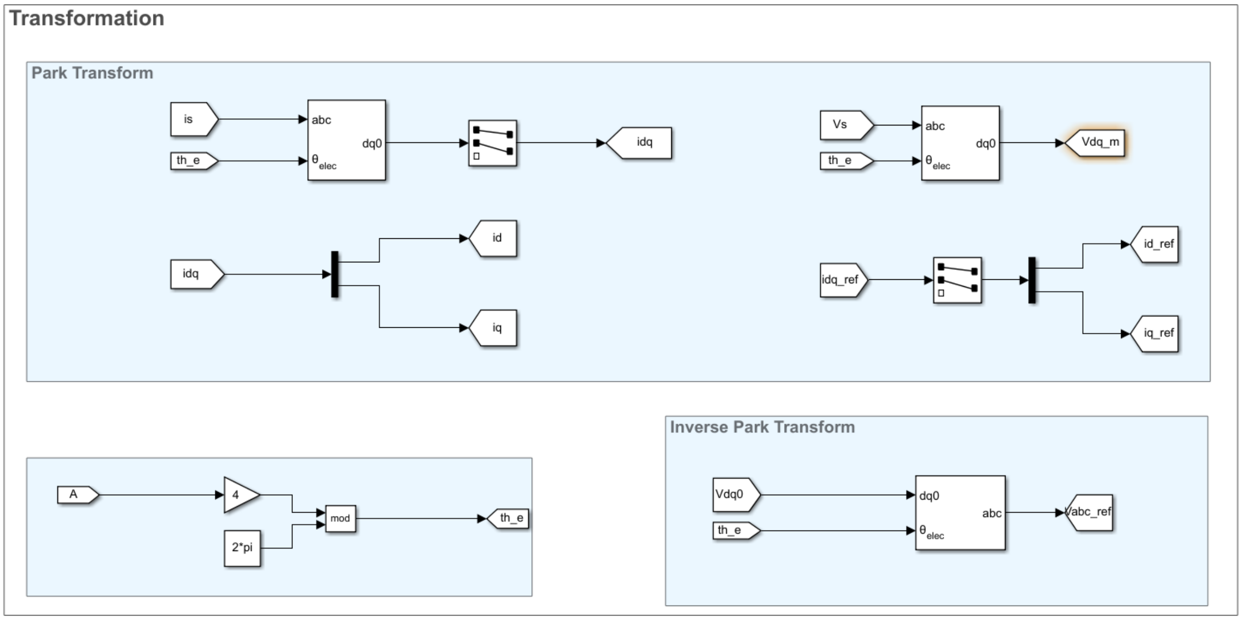

Figure (B.6) The ”Transformation” Block of Figure B.1

B.5 Bias Frequency Component Based Rotor Position Information Extraction

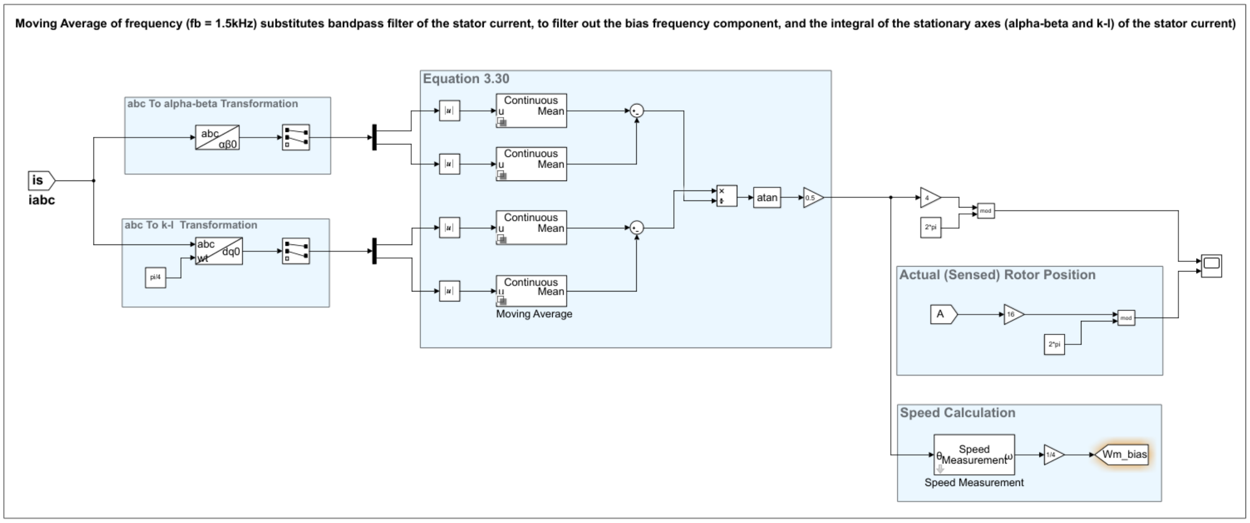

Figure (B.7) The ”Bias Frequency Component Based Rotor Position Information Extraction” Block of Figure B.1

B.6 Outer Loop, MTPA, Flux Weakening and Inner Loop

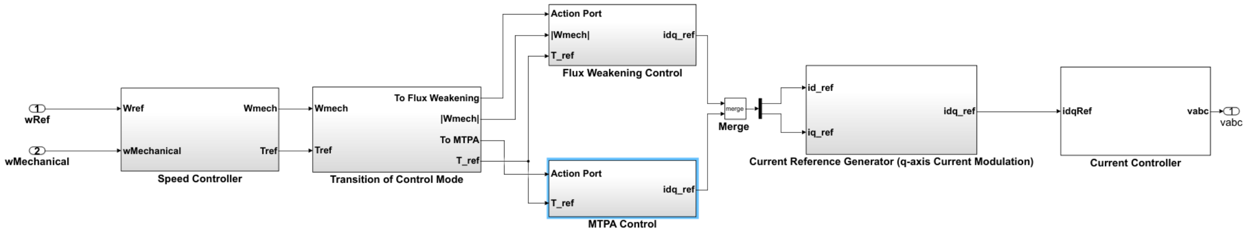

Figure (B.8) The Speed Controller, MTPA Control, Flux Weakening Control and Current Controller Block of Figure B.1

B.6.1 Speed Controller

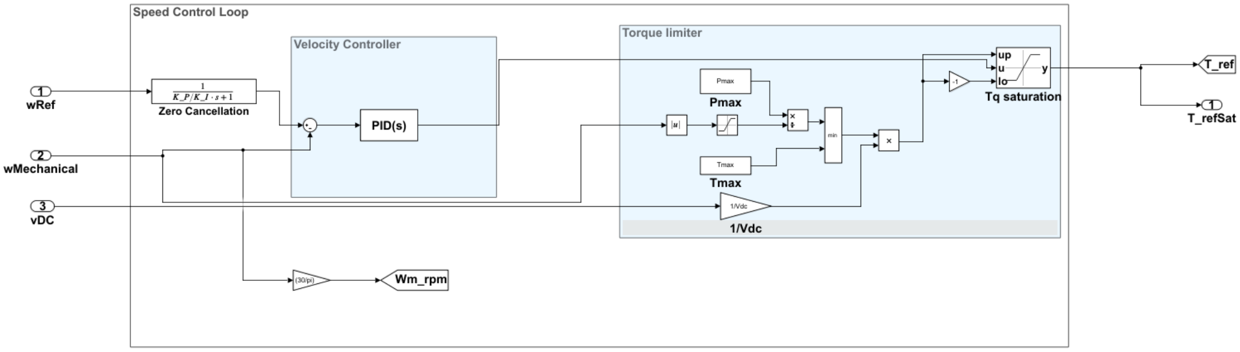

Figure (B.9) ”Speed Controller” Block of Figure B.8

B.6.2 Transition of control from MTPA to FW

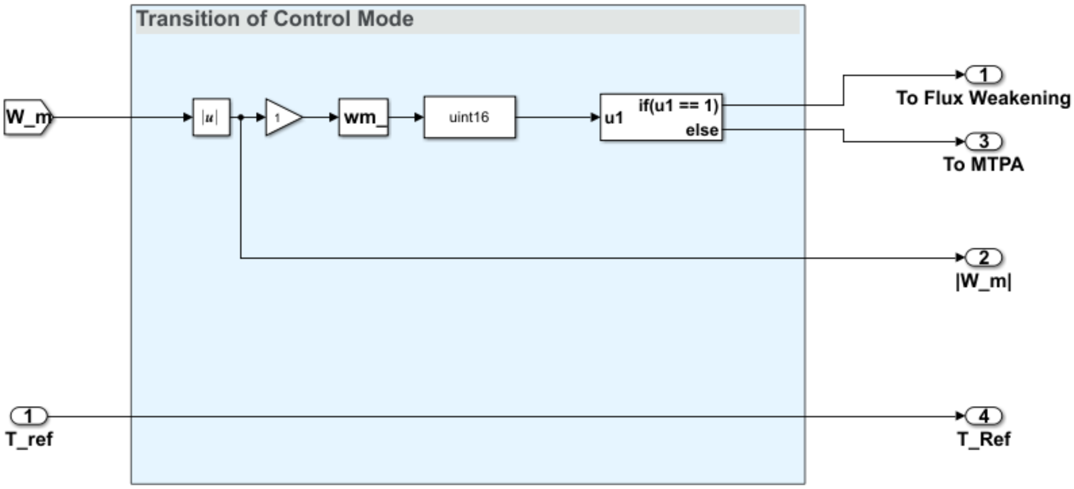

Figure (B.10) The ”Transition of Control Mode” Block of Figure B.8

B.6.3 MTPA Control Model

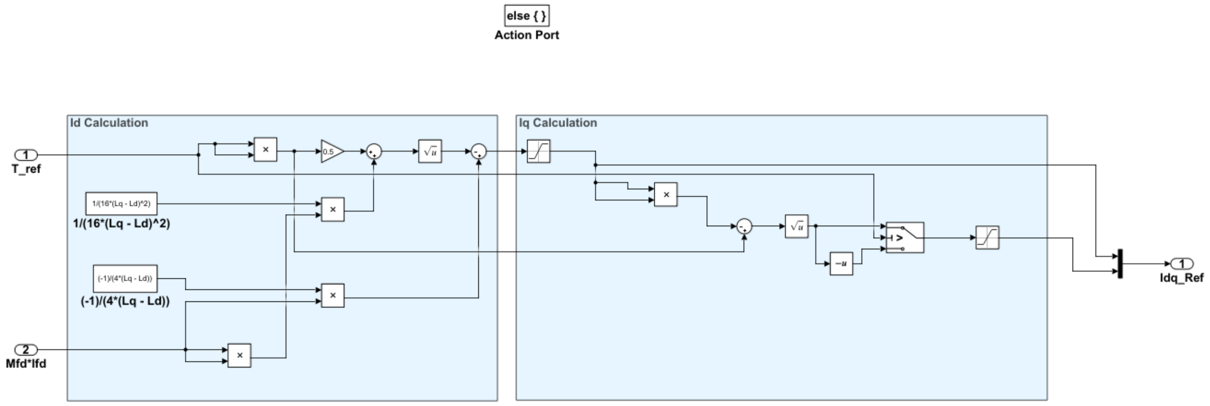

Figure (B.11) The ”MTPA Control” Block of Figure B.8

B.6.4 FW Control Model

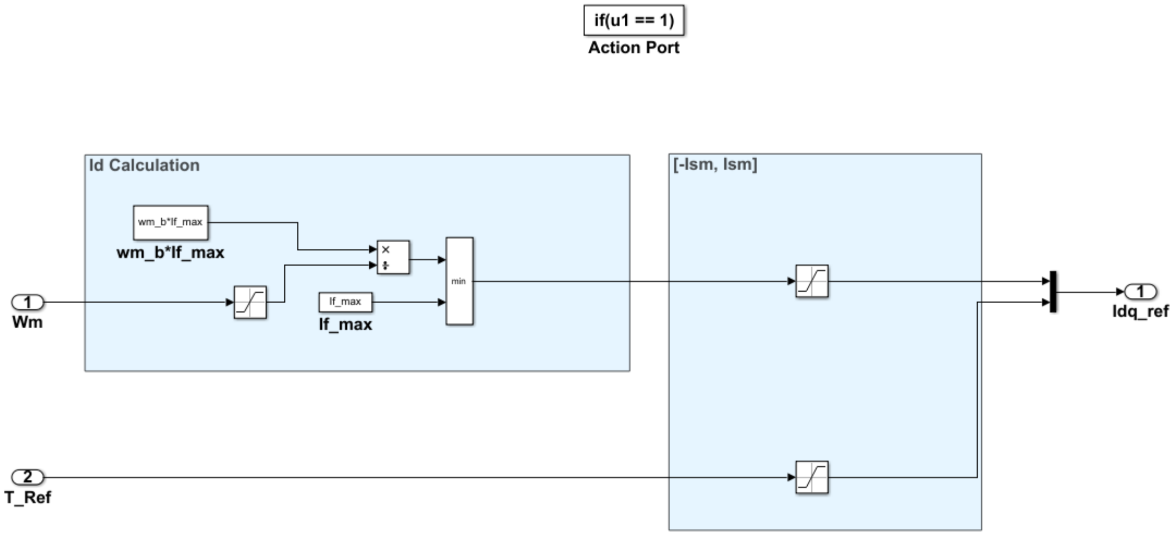

Figure (B.12) The ”Flux Weakening Control” Block of Figure B.8

B.6.5 Current Reference Generator

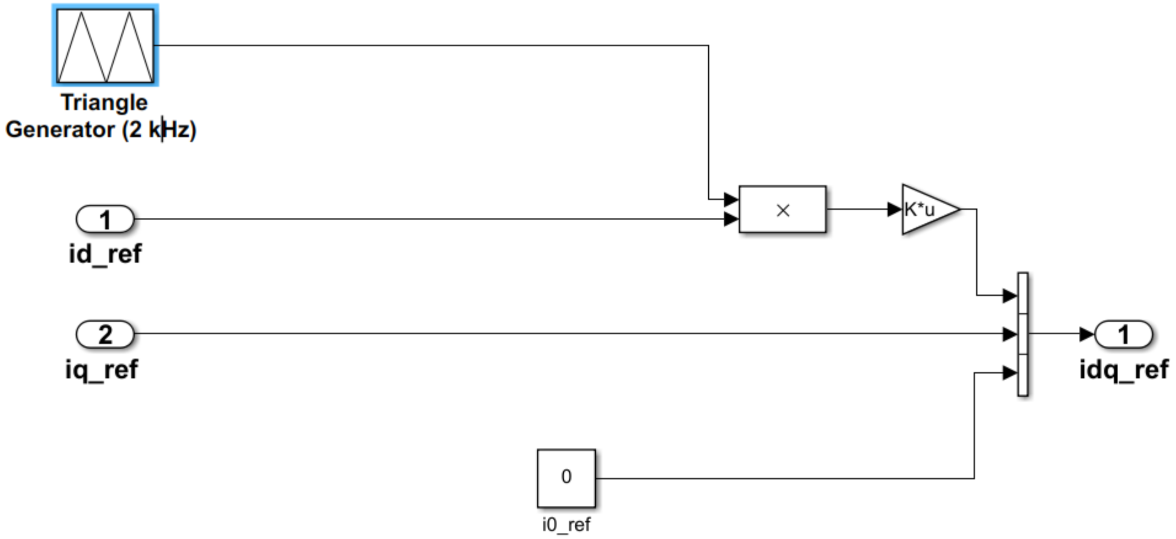

Figure (B.13) Modulation of the reference currents using triangular signal

B.6.6 Current Controller and Decoupling Control

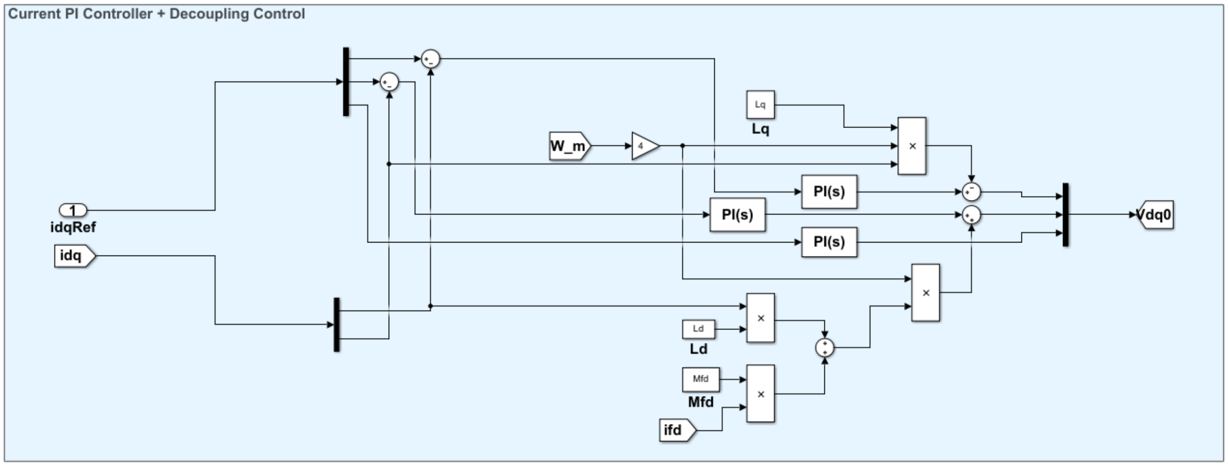

Figure (B.14) ”Current Controller” Block of Figure B.8.

Appendix C

VSI Model on Simplorer

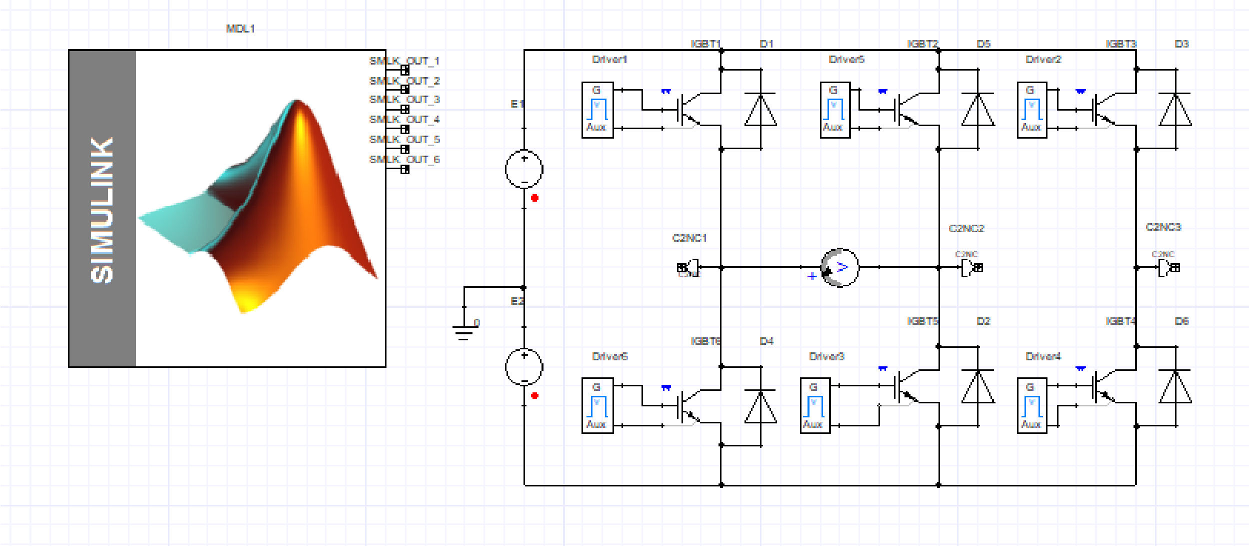

Figure (C.1) VSI model on Simplorer.

Appendix D

SVPWM VSI Modeling

D.1 Realistic SVPWM VSI Model on an Integrated MATLAB/ Simulink and Simplorer Simulation Environment

Refer the figures B.4, B.3, D.2 and D.3 for the realization of ”SVPWM” and ”Inverter model from Simplorer (Sim2Sim link)”, ”FILTER” and ”alpha_beta transformation” blocks of the figure D.1 respectively.

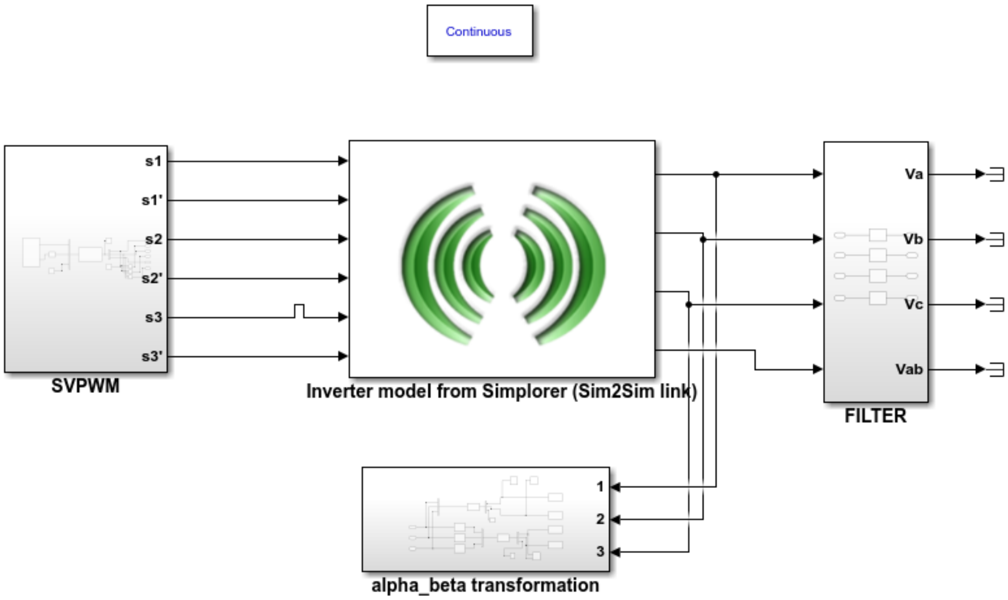

Figure (D.1) Realistic VSI Model Using Integrated Simulink and Simplorer Simulation Environment

D.1.1 Filter

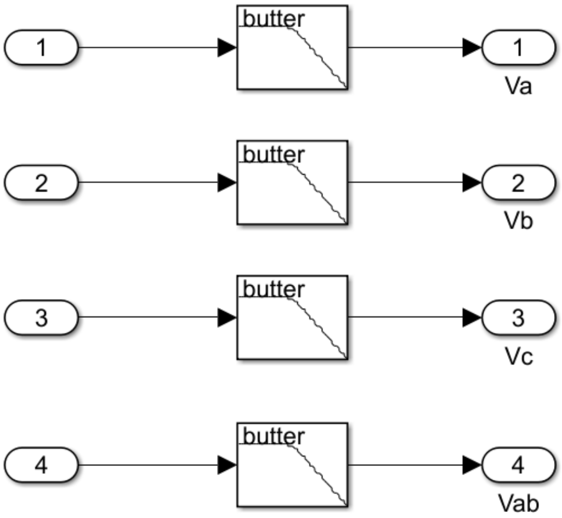

Figure (D.2) Analog Lowpass Filter with Butterworth Design Method, Filter Order of 4 and Passband Edge Frequency of 80Hz

D.1.2 α-β transformation

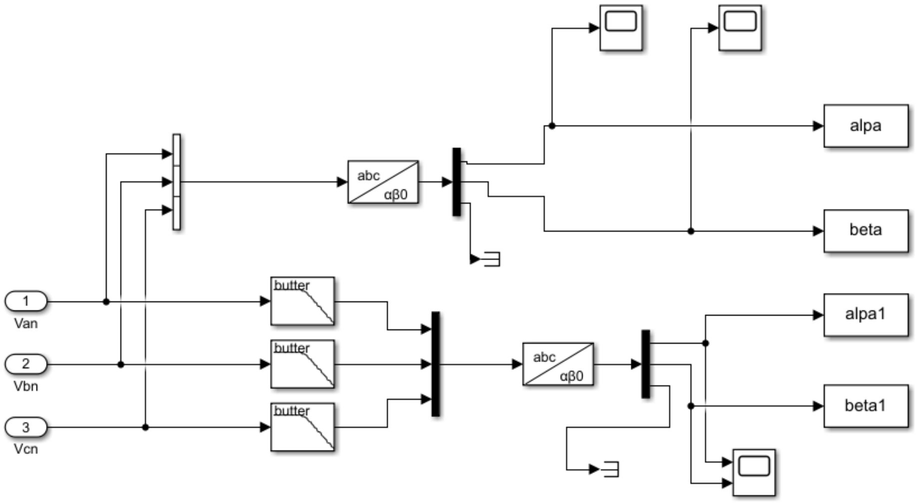

Figure (D.3) Alpha-Beta Transformation

D.2 Ideal VSI Model on MATLAB/ Simulink

Refer the figures B.4, D.5, D.2 and D.3 for the realization of ”SVPWM”, ”Ideal VSI”, ”FILTER” and ”alpha_beta transformation” blocks of figure D.4 respectively.

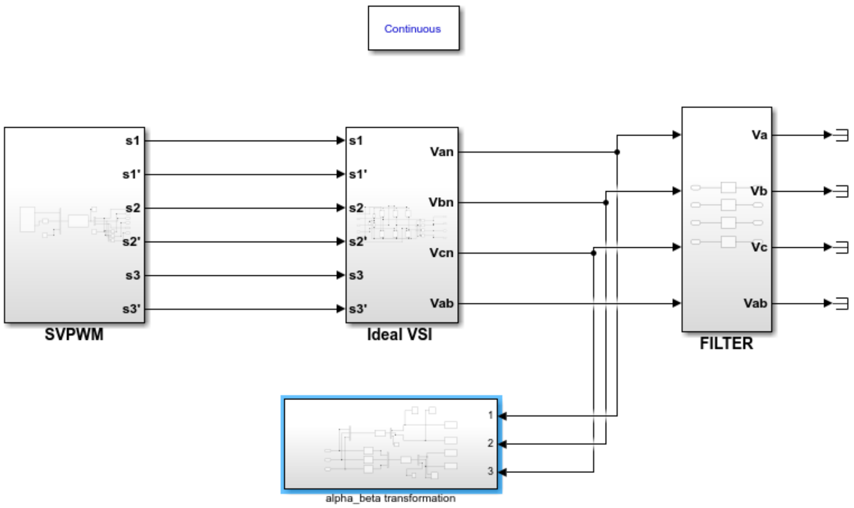

Figure (D.4) Ideal VSI Model on MATLAB/ Simulink Simulation Environment

D.2.1 Ideal VSI Circuit Model on MATLAB/ Simulink

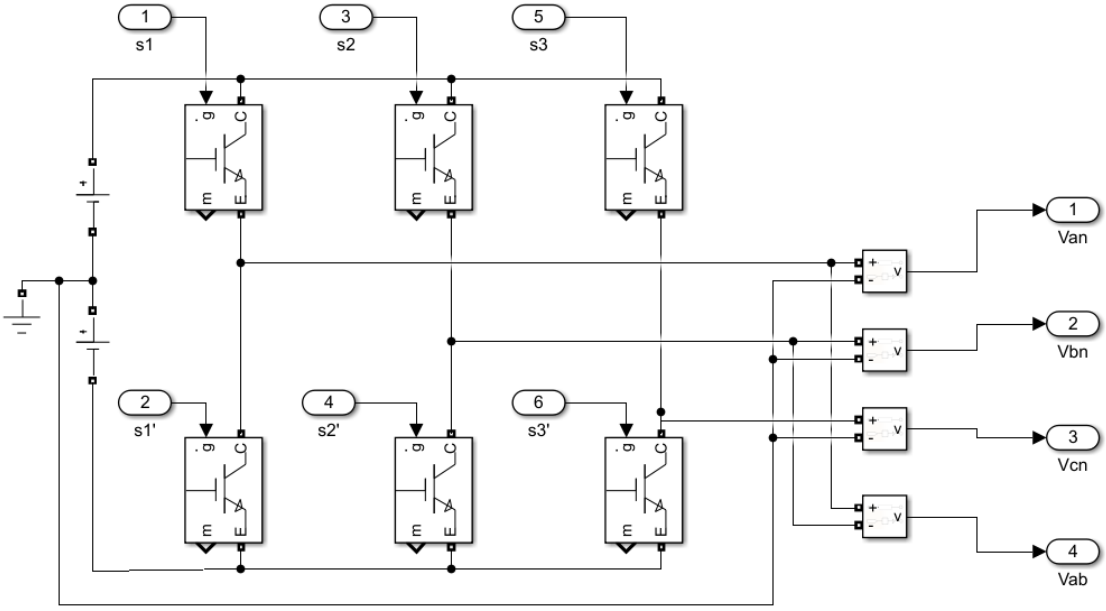

Figure (D.5) Ideal VSI Circuit Model

Appendix E

Implementation of SPWM to the realistic VSI Model on Simplorer

Refer the figures E.2, B.3 and D.2 for the realization ”SPWM”, ”Inverter model from Simplorer (Sim2Sim Link)” and ”FILTER” blocks of the figure E.1 respectively.

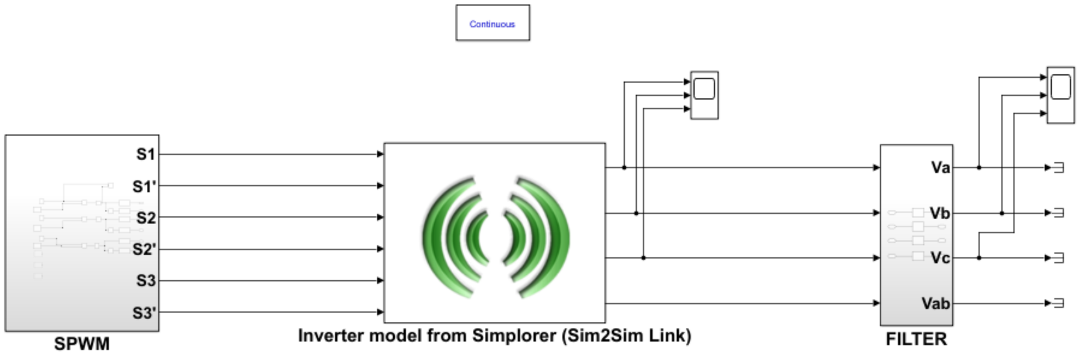

Figure (E.1) SPWM Inverter (VSI) Model on an Integrated Simulation Environment (Simulink To Simplorer)

E.1 Sinusoidal Pulse Width Modulation (SPWM) Gate Control Signal Generation

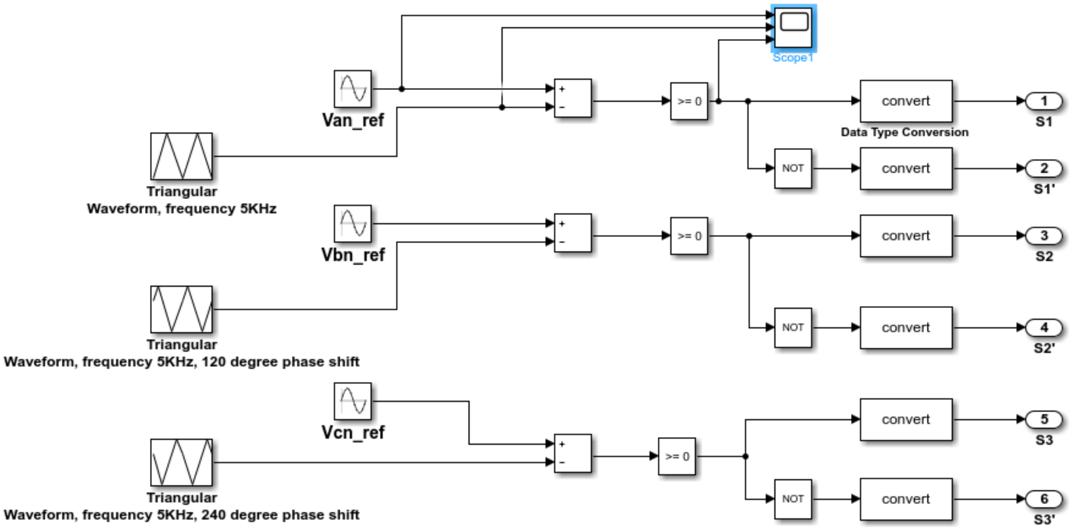

Figure (E.2) SPWM Gate Control Signal Generation on MATLAB/ Simulink To The Realistic VSI Model on Simplorer.